ISSN 2221-6413 (Print), ISSN 2223-2559 (Online)
Coden: PJSIB5 64(1) 01-96 (2021)

Pakistan Journal of Scientific and Industrial Research

Series A: Physical Sciences

Vol. 64, No.1, January-April, 2021

(for on-line access please visit web-site http://www.pjsir.org)

Published by
Scientific Information Centre
Pakistan Council of Scientific and Industrial Research
Karachi, Pakistan

Pakistan Journal of Scientific and Industrial Research

Series A: Physical Sciences (Vol.64, Issue 1, 2021)

Pakistan Journal of Scientific and Industrial Research is published triannually i.e:

Series A: Physical Sciences [**ISSN 2221-6413 (Print); ISSN 2223-2559 (Online)]** (appearing as issues of January-April, May-August and September-December).

This Journal is indexed/abstracted in BIOSIS Preview, NCBI, Pub Med, Scimago, Research Gate, Clarivate Analytics, CABI, Elsevier's Scopus and Zoological Record.

Subscription rates (including handling and Air Mail postage): ***Local:*** Rs. 1500 per volume, single issue Rs. 500/=
Foreign: US$ 450 per volume, single issue US$ 75/=

Electronic format of this journal is available with: ProQuest Information and Learning, 789 E. Eisenhower Parkway, P.O. Box 1346, Ann Arbor, MI 48106-1346, U.S.A.; Fax.No.+1.734.997.4268; http://www.proquest.com

Photocopies of back issues can be obtained through submission of complete reference to the Executive Editor against the payment of Rs. 25 per page per copy (by Registered Mail) and Rs. 115 per copy (by Courier Service), within Pakistan; US$ 10 per page per copy (by Registered Mail) and US$25 per page per copy (by Courier Service), for all other countries.

Composed by: Syed Asif Ali, Imdadullah Khan and Kamran Ahmed; Graphics by: Mansoor Ghani; Webmaster: Mobeen Ali

Printed and Published by: PCSIR Scientific Information Centre, PCSIR Laboratories Campus, Shahrah-e-Dr. Salimuzzaman Siddiqui, Karachi-75280, Pakistan.

Editorial Address

Executive Editor
Pakistan Journal of Scientific and Industrial Research, PCSIR Scientific Information Centre
PCSIR Laboratories Campus, Shahrah-e-Dr. Salimuzzaman Siddiqui, Karachi-75280, Pakistan
Tel: 92-21-99261914-99261916, 99261949, 99261917; Web: http://www.pjsir.org, E-mail: info@pjsir.org

AIMS & SCOPE

Pakistan Journal of Scientific and Industrial Research (PJSIR) was started in 1958 to disseminate research results based on utilization of locally available raw materials leading to production of goods to cater to the national requirements and to promote S & T in the country. Over the past **64** years, the journal convey high quality original research results in both basic and applied research in Pakistan. A great number of major achievements in Pakistan were first disseminated to the outside world through PJSIR.

It is a peer reviewed journal and published in both print and electronic form. Original research articles, review articles and short communications from varied key scientific disciplines are accepted however, papers of Pure Mathematics, Computer Sciences and Medical Sciences are not entertained.

From 54th Volume in 2011 the PJSIR has been bifurcated into two series i.e. Series A: Physical Sciences and Series B: Biological Sciences, the published triannualy i.e. January-April, May-August and September-December issue. It includes research related to Natural Sciences, Organic Chemistry, Inorganic Chemistry, Industrial Chemistry, Physical Chemistry, Pharmaceutical Sciences, Environmental Sciences, Geology, Geography, Physics, Polymer Sciences, Applied Sciences and Nano-Technology related to Physical Sciences.

Due to many global issues, we are encouraging contributions from scientists and researchers from all across the globe with the sole purpose of serving scientific community worldwide on the whole and particularly for our region and third world countries.

Pakistan Journal of Scientific and Industrial Research
Series A: Physical Sciences
Vol. 64, No. 1, January-April, 2021

Contents

Reviews

Pak. j. sci. ind. res. Ser. A: phys. sci. 2021 **64A**(1) 1-5

The Anti-depressant Activity of Fixed Oil of *Phaseolus vulgaris* Linn. in Mice

Salma Sabir[a], Sadia Ghousia Baig[a]*, Muhammad Mohtasheem ul Hasan[b], Afshan Siddiq[a], Salman Ahmed[b] and Syeda Anum Fatima[a]

[a]Department of Pharmacology, Faculty of Pharmacy and Pharmaceutical Sciences, University of Karachi, Karachi, Pakistan

[b]Department of Pharmacognosy, Faculty of Pharmacy and Pharmaceutical Sciences, University of Karachi, Karachi, Pakistan

(received April 26, 2019; revised November 26, 2019; accepted December 12, 2019)

Abstract. *Phaseolus vulgaris* Linn commonly known as red kidney bean, it is enriched in protein, carbohydrates and dietary fibres. Beans have nutritional and health benefits and also possess antimicrobial, antihyperglycemic, antioxidant and anticancer activity due to presence of bio-active chemical constituents. The following study was carried out to evaluate the anti-depressant activity of *Phaseolus vulgaris* fixed oil (PVFO) using forced swim test and tail suspension test in mice. In this study animals assigned into four groups (n=7). Group I: Control normal saline (2 mL/Kg), Group II: PVFO I (2 mL/Kg), Group III: PVFO II (4 mL/Kg) and Group IV: standard amitriptyline (10 mg/Kg). The results were significant and indicated the possible anti-depressant role of *Phaseolus vulgaris* fixed oil.

Keywords: *Phaseolus vulgaris*, fixed oil, anti-depressant, forced swim test, tail suspension test, beans

Introduction

The remedies based on plants or herbs used from ancient times because the plants are economical. In each era the use of herbal medicine is admired because they meet the criteria for immediate personal need. Herbal and plant based drugs are gaining attention in developing countries for health related products. For the last few decades the demand of herbal medicine in global market is growing vigorously (Rana *et al*., 2016).

Phaseolus vulgaris Linn also known as red kidney beans are substantial edible seeds, farmed and utilized globally. They have rich source of proteins, starch and dietary fibres. Dry beans also a great source of nutrients and has lots of importance as functional food, contain high content of protein that is why placed in group with fish, meat, eggs and nuts. 100 g of cooked beans could fulfil 8-10% of the daily protein requirement. A variety of prebiotics (resistant starch and the fructo-oligosaccharides, stachyose and raffinose) are also present in beans. These compounds have an influence on microbial flora of gastrointestinal tract and gut metabolism, take part in bacterial fermentation process in intestine. In addition to this some minerals and vitamins have been found in dry beans, specifically vitamin B is present in great amounts. All these vitamins are of great importance as involved in DNA synthesis, repair, methylation and serve as co-factor in different reactions. Beans also contain phenolic compounds, tocopherols, unsaturated fatty acids, peptides as well as other constituents. Some valuable biological activities related to chemical constituents of beans have also been reported in literature, which include antimicrobial, anti-hyperglycemic, antioxidant and anticancer activity (Los *et al*., 2018).

Depression is a mood disorder which involves low mood, loss of interest in routine activities, and self esteem with a miserable state, could lead one to suicidal attempt. Worldwide a large number of population is affected by depression. Nowadays, depression is a common disorder which badly affect on daily life of individuals which also causing disability and mortality. Exact etiology of disease is still unknown but according to preclinical studies one of the major factor is alteration in CNS serotonin activity which can lead to affective disorders. Other neuro transmitter such as Dopamine (DA), nor epinephrine (NE), glutamate (GA), brain derived neurotrophic factor (BDNF) are also involved in depression (Dunlop and Nemeroff, 2007). Depression is managed by various medications. Several anti-depressants are available in market but these synthetic drugs are not ideally effective for every patient.

Herbal therapy is highly recommended for depression and most of the patients use herbal drugs for treatment.

*Author for correspondence;
E-mail: sadiaghousiabaig@yahoo.com

Conventional anti-depressants possess various adverse effects. An experimental study concluded that *Phaseolus vulgaris* seed extracts have significant anti-depressant activity, which may be linked with presence of tryptophan and omega-3 fatty acids (Devi and Sharma, 2014). The present study is aimed to evaluate the possible anti-depressant effect of fixed oil of *Phaseolus vulgaris* L.

Materials and Methods

Plant material and oil extraction. Dry seeds of *Phaseolus vulgaris* L were purchased from local market. Sticks, dirt and stones were separated and seeds were crushed and extracted with hexane. Clear light yellow colour oil was obtained.

Chemicals. Amitriptyline (Merck, Germany) and hexane analytical grade (Merck, Germany).

Animals. Adult mice of both sexes weighing around 20-25 g were taken for current study and housed in a controlled environment of 12 h light and dark cycle at 22-25 °C temperature, and humidity was kept between 50-60%. Propylene plastic cages were used for housing mice and maximum 5 mice were housed per each cage. Mice were given standard food and given free access to tap water. The experimental protocol was approved by institutional Bioethics committee, Faculty of Pharmacy and Pharmaceutical Sciences on 17th April 2017 (IBCPH 17) and Board of Advanced Studies (BASR), University of Karachi in November 2015. All experiments were performed in accordance with relevant guidelines and regulations.

Anti-depressant activity. *Forced swim test.* Mice were divided in four groups (n=7). The animals received different treatments as follows:

Group-I: normal saline (2 mL/Kg); Group-II: fixed oil of *Phaseolus vulgaris* (2 mL/Kg); Group-III: fixed oil of *Phaseolus vulgaris* (4 mL/Kg); Group-IV: standard (amitriptyline 10 mg/Kg), All test animals were brought from animal house to the laboratory to acclimatize, 1-2 h before starting experiment. All groups were administered respective doses orally. One hour after dose administration mice were put into cylinder filled with water and allowed to swim. The test comprised of total 6 min, in which initial 2 min considered habituation period and later 4 min observed the immobility showed by mice. Immobility time was recorded manually with the help of stop watch. After 6 min mice were removed from water and dried with soft towel. Each mouse was used once for swimming (Porsolt *et al*., 1977).

Tail suspension test. Mice were divided in four groups (n=7). The animals received different treatments as follows:

Group-I: normal saline (2 mL/Kg); Group-II: fixed oil of *Phaseolus vulgaris* (2 mL/Kg); Group-III: fixed oil of *Phaseolus vulgaris* (4 mL/Kg); Group-IV: standard (amitriptyline 10 mg/Kg), All test animals were brought from animal house 1-2 h before starting experiment to the laboratory to acclimatize with the conditions. All groups were administered respective doses orally. After 1 h of dose administration mice were individually suspended about 1 cm from the tip of tail with the help of adhesive tape to the rim of table at a height of 50 cm above the floor. Mouse was observed carefully for total 6 min. Immobility time during 6 min was recorded manually using stop watch. Each mouse was used once in the experiment (Steru *et al*., 1985).

Statistical analysis. Data is expressed as mean ±SEM and statistically analysed by SPSS version 20. One way ANOVA was used and followed by tukey hsd. $P<0.05$ was considered significant.

Results and Discussion

Force swim test. Data of forced swim revealed that PVFO markedly decreased the immobility time. With both doses i.e. 2 mL/Kg and 4 mL/Kg there is reduction observed in immobility time as compared to control. Amitriptyline used as standard reference, with 10 mg/Kg dose also reduced the immobility time. The results were found significant at $P<0.05$ in all cases (Table 1).

Tail suspension test. PVFO very significantly ($P<0.001$) reduced the immobility time with 2 mL/Kg dose as

Table 1. Force swim test

Groups	Dose	Immobility time (sec)
Control	2 mL/Kg	135±5.13
PVFO I	2 mL/Kg	74±9.06***
PVFO II	4 mL/Kg	105±1.85*
Amitriptyline	10 mg/Kg	106±5.13*

Data is expressed as mean±standard error of mean (SEM); N=7; Control=Normal saline; PVFO=*Phaseolus vulgaris* fixed oil; ***=Very highly significant at $P<0.001$ as related to control; **=Highly significant at $P<0.01$ as related to control; *=Significant at $P<0.05$ as related to control.

compared to control. Similarly, amitriptyline also showed highly significant (P<0.001) reduction in immobility time with 10 mg/Kg dose level. Results showed that fixed oil also reduced immobility time with 4 mL/Kg and reduction in immobility is significant at P<0.05 (Table 2).

Table 2. Tail suspension test

Groups	Dose	Immobility time (sec)
Control	2 mL/Kg	269±13.50
PVFO I	2 mL/Kg	141±0.86***
PVFO II	4 mL/Kg	217±1.08**
Amitriptyline	10 mg/Kg	174±2.97***

Data is expressed as mean± standard error of mean (SEM); N=7; Control=Normal saline; PVFO=*Phaseolus vulgaris* fixed oil; ***=very highly significant at P<0.001 as related to control; **=Highly significant at P<0.01 as related to control; *=Significant at P<0.05 as related to control.

Depression is low mood behaviour characterised by helplessness, misery, apathy, loss of self confidence, lack of interest, along with biological symptoms including psychomotor impairment, sleep disorders, loss of libido and appetite. Depression is considered major after symptoms intensify (Ashok *et al*., 2014). For treatment of depression different synthetic drugs such as tricyclic anti-depressants (TCAs), selective serotonin re-uptake inhibitors (SSRIs), selective reversible inhibitors of monoamine oxidase A (RIMAs), and specific serotonin–noradrenaline reuptake inhibitors (SNRIs) are available and used clinically (Fava, 2003) but these drugs are associated with serious side effects such as hypotension, sexual dysfunction, cardiac toxicity, increase in body weight, sleep disorders (Park *et al*., 2005).

Amitriptyline is a tri cyclic anti-depressant that enhances the activity of nor-epinephrine or serotonin or both (Feighner, 1999). In FST the parameter of observing depression is immobility, that is lowered mood behaviour adopted by mice in forced swim test. The overall exposure time comprises of 6 min, in which first 2 min considered as habituation period and later 4 min was taken as test observation which gives the time duration of immobility (Abelaira *et al*., 2013). A mouse is considered immobile when it stops swimming and other body movements excluding some necessary movement to keep the head above the level of water. A drug is believed to be anti-depressant that decreases the depressed behaviour by decreasing immobility time. PVFO showed decrease in immobility time as compared to control. PVFO with 4 mL/Kg showed similar effect as standard reference amitriptyline exhibited. The anti-depressant effect showed by fixed oil may be due to re-uptake inhibition of nor epinephrine along with serotonin. Lipid content is very low in common beans, which comprised of some important unsaturated fatty acids (Mabaleha and Yeboah, 2004). These unsaturated fatty acids mainly consist of palmitic acid, oleic and linoleic acid (Grela and Gunter, 1995). Omega-3 fatty acid are derived from α-Linolenic acid (ALA). Anti-depressant effect of omega-3 fatty acid has been reported previously (Lakhwani *et al*., 2007). Anti-depressant activity of flax seed fixed oil also has been proved by experimental study. ALA is major fatty acid found in flax seed (Rath and Pardhan, 2012).

Massive quantity of research has done on this topic suggests that increased production of pro-inflammatory cytokines is involved in depression. These cytokines including interleukin-1 beta (IL-1β), interleukin-2 (IL-2), interleukin-6 (IL-6), interferon-gamma (IF) and tumor necrosis factor-alpha (TNF-α) can effect central nervous system directly or indirectly. They decrease the availability of neuro transmitter precursors, activate the hypothalamic-pituitaryaxis and alter the metabolism of neuro transmitters and neuro transmitter transporters. Excessive production of IL-1β and TNF-α are related to severe depression (Suarez, 2003). Increase production of cytokines results from psychological stress, trauma, toxins, infection and some other factors. Omega-3 fatty acids have been reported as pro-inflammatory cytokines inhibitors specifically TNF-α and IL-1, but exact mechanism of inhibition is unknown (James *et al*., 2000). The exact chemical composition of PVFO is still unidentified, may be presence of omega-3 fatty acid in PVFO is responsible for antidepressant activity.

PVFO was also evaluated for anti-depressant activity using tail suspension model of depression. Same as in force swim test immobility time is the criteria for evaluating depression. In TST immobility is described as a static behaviour in which mice do not make any body movement to escapes from hanging and appear totally motionless. Peaceful and calm environment is basic criteria for TST (Uddin *et al*., 2018). Mice were considered immobile when they hung inactively and completely motionless. A decrease in immobility time is indicating the anti-depressant effect of an agent. PVFO with the dose 2 mL/Kg and amitriptyline

produced very highly significant (P<0.001) reduction in immobility time as compared to control group. The effect observed with 2 mL/Kg dose was better than amitriptyline. PVFO with 4 mL/Kg dose also showed a small decrease in immobility time. We can say that antidepressant effect of PVFO is due to presence of omega-3 fatty acid in it. PUFAs are involved in regulating certain processes in central nervous system such as adjusting blood glucose and food consumption as well as these fatty acids take part in process of apoptosis, regulating emotional behaviour, neuro transmission and neuro inflammation. Furthermore, dietary PUFAs (n-3) control various neuro transmitter operations, as well as signal transmission, responsiveness and phospholipid alteration. PUFAs (n-3) are also connected with psychiatric syndromes and required for mental development, avoidance of neuronal death, and the inhibition of neuro inflammation.

Locomotor activity is a sign of mental alertness and decrease locomotion could be interpreted as reduced CNS excitability which is indicative of calmness and sedation (Islam *et al*., 2015). The decrease in overall locomotion is an indication of sedative activity (Hossain *et al*., 2016). A drug with sedative effect reduces locomotor activity in open field test which can also be interpreted as lack of curiosity to the novel environment (Moniruzzaman *et al*., 2015). In the open field study conducted on PVFO (2 mL/Kg and 4 mL/Kg), it produced calming effect shown by significant decrease in number of boxes crossed (Salma *et al*., 2018). According to another research anti-depressants Fluoxetine, Imipramine and Venlafaxine reduce the locomotor activity in unfamiliar environment (Kawai *et al*., 2019). Which support the finding of current study of PVFO and shows anti-depressant activity and decreases locomotor activity.

Conflict of Interest. The authors declare no conflict of interest.

References

Abelaira, H.M., Reus, G.Z., Quevedo, J. 2013. Animal models as tools to study the pathophysiology of depression. *Brazilian Journal of Psychiatry*, **35:** S112-S120.

Ashok, K.B.S., Lakshman, K., Velmurugan, C., Sridhar, S.M., Gopisetty, S. 2014. Anti-depressant activity of methanolic extract of amaranthusspinosus. *Basic and Clinical Neuroscience*, **5:**11-17.

Devi, M., Sharma, R. 2014. Anti-depressant activity of aqueous extract of *Phaseolus vulgaris* (black bean) in rodent models of depression. *International Journal of Nutrition, Pharmacology, Neurological Diseases*, **4:** 118.

Dunlop, B.W., Nemeroff, C.B. 2007. The role of dopamine in the pathophysiology of depression. *Archives of General Psychiatry*, **64:** 327-337.

Fava, M. 2003. Diagnosis and definition of treatment-resistant depression. *Biological Psychiatry*, **53:** 649-659.

Feighner, J.P. 1999. Mechanism of action of anti-depressant medications. In: *Assessing Anti-depressant Efficacy*: *A Re-examination* in Jan, 1998, Phoenix, AZ, US. Physicians Postgraduate Press.

Grela, E.R., Günter, K.D. 1995. Fatty acid composition and tocopherol content of some legume seeds. *Animal Feed Science and Technology*, **52:** 325-331.

Hossain, M.F., Talukder, B., Rana, M.N., Tasnim, R., Nipun, T.S., Uddin, S.N., Hossen, S.M. 2016. *In vivo* sedative activity of methanolic extract of *Stericulia villosa* Roxb. leaves. *BMC Complementary and Alternative Medicine*, **16:** 398.

Islam, N.U., Khan, I., Rauf, A., Muhammad, N., Shahid, M., Shah, M.R. 2015. Antinociceptive, muscle relaxant and sedative activities of gold nanoparticles generated by methanolic extract of *Euphorbia milii*. *BMC Complementary and Alternative Medicine*, **15:** 160.

James, M.J., Gibson, R.A., Cleland, L.G. 2000. Dietary polyunsaturated fatty acids and inflammatory mediator production. *The American Journal of Clinical Nutrition*, **71:** 343S-348S.

Kawai, H., Iwadate, R., Ishibashi, T., Kudo, N., Kawashima, Y., Mitsumoto, A. 2019. Anti-depressants with different mechanisms of action show different chrono-pharmacological profiles in the tail suspension test in mice. *Chronobiology International*, 1-14.

Lakhwani, L.A.L.I.T., Tongia, S.K., Pal, V.S., Agrawal, R.P., Nyati, P.R.M., Phadnis, P.R.A.D.E.E.P. 2007. Omega-3 fatty acids have anti-depressant activity in forced swimming test in Wistar rats. *Acta Poloniae Pharmaceutical*, **64:** 271-6.

Los, F.G.B., Zielinski, A.A.F., Wojeicchowski, J.P., Nogueira, A., Demiate, I.M. 2018. Beans (*Phaseolus vulgaris* L.): whole seeds with complex chemical composition. *Current Opinion in Food Science*, **19:** 63-71.

Mabaleha, M.B., Yeboah, S.O. 2004. Characterization

and compositional studies of the oils from some legume cultivars, *Phaseolus vulgaris*, grown in southern Africa. *Journal of the American Oil Chemist's Society*, **81:** 361-364.

Moniruzzaman, M., Rahman, A., Ferdous, A. 2015. Evaluation of sedative and hypnotic activity of ethanolic extract of *Scoparia dulcis* Linn. *Evidence-Based Complementary and Alternative Medicine*, 2015.

Park, I.Y., Kim, E.J., Park, H., Fields, K., Dunker, A.K., Kang, C. 2005. Interaction between cardiac calsequestrin and drugs with known cardiotoxicity. *Molecular Pharmacology*, **67:** 97-104.

Porsolt, R.D., Le Pichon, M., Jalfre, M.L. 1977. Depression: a new animal model sensitive to anti-depressant treatments. *Nature*, **266:** 730.

Rana, J.H., Patel, U.R., Sonia, J.P., Vijay, L., Dhiran, P.S. 2016. Pharmacological Activities of *Phaseolus vulgaris*: A Review. *Pharma Science Monitor*, **7:** 107-115.

Rath, B.P., Pradhan, D. 2012. Anti-depressant activity of *Linum usitatissimum* extract. *International Journal of Pharmacognostic and Phytochemical Research*, **1:** 29-32.

Salma, B.S.G., Hasan, M., Ahmed, S., Fatima, S.A. 2018. The effect of *Phaseolus vulgaris* L. Fixed oil on the behavioural activity of swiss albino mice. *RADS Journal of Pharmacy and Pharmaceutical Sciences*, **6:** 76-82.

Steru, L., Chermat, R., Thierry, B., Simon, P. 1985. The tail suspension test: a new method for screening anti-depressants in mice. *Psychopharmacology*, **85:** 367-370.

Suarez, E.C., Krishnan, R.R., Lewis, J.G. 2003. The relation of severity of depressive symptoms to monocyte-associated pro-inflammatory cytokines and chemokines in apparently healthy men. *Psychosomatic Medicine*, **65:** 362-368.

Uddin, M.M.N., Kabir, M.S.H., Hasan, M., Al Mahmud, Z., Bhuiya, N.M.A., Ahmed, F., Hasan, M.R., Hosen, M.T., Alam, M.S. 2018. Assessment of the antioxidant, thrombolytic, analgesic, anti-inflammatory, anti-depressant and anxiolytic activities of leaf extracts and fractions of *Tetracera sarmentosa* (L.) Vahl. *Journal of Basic and Clinical Physiology and Pharmacology*, **29:** 81-93.

Pak. j. sci. ind. res. Ser. A: phys. sci. 2021 **64A**(1) 6-9

Efficacy Studies of Two Iron Supplements Irovit-1 and Irovit-2

Rehana Jafri, Amir Ahmed, Kamran Abro*, Irshad Ahmed Khan and Atiq ur Rehman
Pharmaceutical Research Centre, Pakistan Council of Scientific and
Industrial Research Laboratories Complex, Karachi - 75280, Pakistan

(received October 31, 2018; revised December 21, 2018; accepted December 27, 2018)

Abstract. Two preparations of iron supplements have been developed with vitamins, Irovit-1 and Irovit-2 containing 1 mg/mL and 2 mg/mL elemental iron respectively in complex form. Clinical trials of Irovit-1 and Irovit-2 have been conducted randomly on selected anemic males and females from urban population of Karachi, an improvement in hemoglobin levels were estimated for the treatments with Irovit-1 (10 mg Fe/day) and Irovit-2 (20 mg Fe/day). Both preparations have been found to be effective in increasing hemoglobin, Hematocrit and red blood cell count. The mean hemoglobin levels were observed increased 0.73 ± 0.25 g/dL and 1.10 ± 0.30 g/dL, after 5 weeks by oral intake of Irovit-1 and Irovit-2, respectively.

Keywords: iron saccharate, oral supplements, efficacy hemoglobin level

Introduction

Iron deficiency anemia (IDA) is a major worldwide nutritional problem (Organization, 2011). Causes of anemia may be insufficient dietary iron intake; iron loses e.g. bleeding, parasite infestation and malabsorption of iron (Wiley Encyclopedia of Food Science and Technology, 1992). But all types of anemia have the same effect i.e. the lack of hemoglobin in red blood cells, which prevent proper oxygen transport through the body. Iron deficiency causes insufficient hemoglobin production, resulting in anemia symptoms (Campbell *et al*., 2018; Percy *et al*., 2017; Wong, 2017; Frewin *et al*., 1997). The average adult body contains 3g of iron. About 65% is found in the hemoglobin which carries oxygen from lungs to the various parts of the body (Krik-Oltmer Encyclopedia of Chemical Technology, 2005). A recent modification of WHO definition states that anemia in pregnancy when hemoglobin concentration falls below 11.0 g/dL (Organization, 2011).

The groups at greatest risk for developing IDA are menstruating females, pregnant or nursing females and young children (Minar *et al*., 2015; Wiley Encyclopedia of Food Science and Technology, 1992). Most athletes especially female have low-mid range hemoglobin values referred to as sports anemia thus affects their sports performance (Brownlie *et al*., 2002). Low concentration of Hb < 7 g/dL causes anemia with a few remarkable symptoms increasing lethargy, headaches, tinnitus and taste disturbances (Wiley Encyclopedia of Food Science and Technology, 1992). During pregnancy, womens have low mild range hemoglobin levels which is an extra demand for the fetus (Chandra *et al*., 2012). Food and nutrition board of the institute of medicine recommended routine use of 30 mg/day iron supplement during pregnancy. During pregnancy when the depletion of Hb level is fast, immediate administration of iron is essential to overcome this deficiency. This could only be accomplished by parenteral administration which is also the preferred route in patient which suffering from gastrointestinal disturbance caused by oral intake of iron, it is more pronounced during pregnancy. But the parenteral administration practices have their own drawbacks. Allergic side reactions, often fatal, also occur, such as hygienic safety problems described by (Feightner, 1994).

According to USP and BP the oral preparations usually used in iron deficiency anemia are mostly salts as shown in Table 1 (Birtish Pharmacopeia, 2008; United State Pharmacopeia /National Formulay, 2008). All these preparations are associated with high risk incidence of side effects including nausea, constipation and diarrhea. These side effects may be reduced by taking the drugs after meals or by the use of sustain released preparation of iron (complex form) (Frewin *et al*., 1997). Thus the following study described a preparation in the same context.

The efficacy of two preparations Irovit-1 and Irovit-2 were assessed containing iron and multi-vitamins showed in (Table 2). Both preparations contain non-

*Author for correspondence;
E-mail: abrokamran@gmail.com

Table 1. Most common commercially available iron salts

Preparations	Amount in mg/day	Fe content in mg/day
Ferrous fumarate	200 mg	65 mg
Ferrous gluconate	300 mg	35 mg
Ferrous succinate	100 mg	35 mg
Ferrous sulfate	300 mg	60 mg

Table 2. Composition of Irovit-1 and Irovit-2

Name of products	Ingredients	Amount per 10 mL syrup
Irovit-1	Fe elemental (saccharated oxide of iron)	10 mg
	Vitamins:	
	Thiamine HCl	0.35 mg
	Riboflavin	0.40 mg
	Nicotinamide	4.50 mg
	Pyridoxine HCl	0.35 mg
	Ascorbic acid	20 mg
	Folid acid	0.1 mg
Irovit-2	Fe elemental (saccharated oxide of iron)	20 mg
	Vitamins:	
	Thiamine HCl	1.5 mg
	Riboflavin	2.0 mg
	Nicotinamide	20 mg
	Pyridoxine HCl	2.0 mg
	Ascorbic acid	40 mg
	Folid acid	0.3 mg

ionic colloidal form of saccharated oxide of iron, which ensures slow release of iron and maintain constant level of iron in the body (Martindale: extra pharmacopoeia, 1977). These preparations containing low levels, 1 mg/mL and 2 mg/mL of elemental iron are designed with a view to avoid well known gastrointestinal side effect of oral iron preparation containing high levels of elemental iron. Vitamins, especially vitamin C was added in the syrup to enhance absorption of iron (Hallberg *et al*., 1986).

Material and Methods

Preparation of Irovit-1 and Irovit-2. Preparation of Irovit-1 and Irovit-2 comprised of two process (i) preparation of saccharated iron oxide and (ii) preparation of stabilized sugar base and addition of saccharated iron oxide and vitamins to this base.

Preparation of saccharated iron oxide. Saccharated iron oxide was prepared by following the method developed earlier in our laboratory (Zaidi and Mahdihassan, 1962).

Preparation of stabilized sugar base. The addition of saccharated iron oxide and vitamins to the base sugar (75 Kg), methyl-p-hydroxy benzoate (100 g), propyl p-hydroxy benzoate (50 g) and distilled water 15-20 L was placed in a 200 L stainless steel steam jacketed vessel, heated to 90ºC with vigorous stirring till the sugar dissolved completely. In another vessel carboxymethyl cellulose (180 g) was dissolved in hot water (50-60 ºC) and added to sugar solution, while hot. The mixture was left to cool at room temperature. Saccharated iron oxide containing 100 g of elemental iron was added to above mixture. Food colour (20 g) dissolved in water (20 mL) was added to the above mixture. pH of the mixture was adjusted to 7 by adding 28.5 g citric acid and finally orange flavor (125 mL) was added. Mixture of vitamins was also added to above solution and stirring continued till homogenous mixture obtained.

Evaluation of efficacy and tolerability of Irovit-1 and Irovit-2. 10 anemic patients (group-1) were selected for testing Irovit-1 and 15 anemic patients (group-2) were selected for testing Irovit-2 from urban area of Karachi. After taking their data, age, weight, height, blood pressure and initial blood sampling, they were provided with supplement 10 mL of Irovit-1 and Irovit-2 for 30-45 days. Subsequent blood sampling was done after 5 weeks. The parameters included in the study were, serum hemoglobin, hematocrit and RBC count.

Hemoglobin was estimated by cynamet hemoglobin method on Sysmax K1000 hematology auto-analyzer. Hematocrit and RBC count were also evaluated by the same machine.

Results and Discussion

The efficacy of saccharated iron oxide as oral preparation has never been evaluated before. Two trials were conducted to assess the effectiveness of Irovit-1 and Irovit-2. For these studies patients with low hemoglobin level were selected and divided in two groups. After supplementation an improvement in hemoglobin level was observed in both groups more significantly in patients belonging to group-2 treated with Irovit-2. Patients treated with Irovit-1 showed Hb increased from 0.3 g/dL to 1.0 g/dL, whereas patient treated with

Irovit-2 showed Hb increased from 0.8 g/dL to 1.7 g/dL with a mean value of 0.7 ± 0.25 g/dL in group-1 and 1.10 ± 0.3 g/dL in group-2 (Table 4). The concentration of hemoglobin increase was more rapid in group-2 receiving 20 mg elemental iron daily. Our findings were also supported by longitudinal studies in which 30-200 mg iron were given daily to bring about significant increase of 1.0 to 1.7 g/dL in hemoglobin content (Feightner, 1994). In another study low dose (20 mg/day) of iron has been given to pregnant women. This strategy was found to be effective in preventing IDA and ID in the treated subject (Makrides *et al*., 2003). Food and Nutrition Board of the Institute of Medicine recommended daily oral intake of iron supplement containing 30 mg/day during pregnancy.

Other blood parameters in these patients like hematocrit, red blood cell (RBC) counts and platelets were also studied which are shown in (Table 3). The significant increase in hematocrit (%) was observed from 27.97 ± 3.76 to 31.54 ± 3.5. The mean difference in increase was 3.56 ± 2.20 within 5 weeks of supplementation. RBC count increases from 4.05 x 10^6/uL ± 0.69 to 4.36 x 10^6/uL ± 0.53. The mean significant increase in RBC was noted 0.30 x 10^6/uL ± 0.89 after 5 weeks of supplementation. The platelets increases from 267.73 x 10^3/uL ± 104.98 to 274.8 x 10^3/uL ± 97.02. The mean significant increase in platelets was 7.07 x 10^3/uL after 5 weeks of supplementation.

Table 3. Status of RBC & HGB, PLT & Hematocrit in patients before and after taking Irovit-2

Parameters	Units	Mean ± SD at 0 week	Mean ± SD at 5 weeks	Mean difference ± SD
Hemoglobin	g/dL	8.16 ± 1.34	9.26 ± 1.24	1.10 ± 0.30
Hematocrit	%	27.97 ± 3.76	31.54 ± 3.50	3.57 ± 2.20
RBC count	x10^6/µL	4.05 ± 0.69	4.36 ± 0.53	0.31 ± 0.89
Platelets	x10^3/µL	267.73 ± 104.98	274.8 ± 97.02	7.07 ± 3.23

Table 4. Comparison of the mean hemoglobin value at 0 and after 5 weeks in Group-1 (Irovit-1) and Group-2 (Irovit-2)

	Units	Mean ± SD at 0 week	Mean ± SD at 5 weeks	Mean increase ± SD
Group-1	g/dL	9.53 ± 1.57	10.26 ± 1.50	0.73 ± 0.25
Group-2	g/dL	8.16 ± 1.34	9.26 ± 1.24	1.10 ± 0.30

Conclusion

Both the preparation indigenously produced Irovit-1 and Irovit-2 have low iron concentrations and are readily absorbed. The normal side effects associated with other oral iron preparations were missing. Our investigation has shown that low iron doses (20 mg/day) is sufficient to manage iron deficiency anemia effectively. Moreover, very low doses of iron (10 mg/day) are also beneficial for anemia treatment, but not as effective as 20 mg/day, resulting in a substantial increase in the level of hemoglobin.

The significance increase in hematocrit % 3.56 ± 2.20 and RBC counts x 10^6/uL 0.30 ± 0.89 shows significant rise from base line suggested the better absorption and cure of anemia by using the Irovit-2 (20 mg Fe/10 mL) within 5 weeks.

Conflict of Interest. The authors declare no conflict of interest.

References

Birtish Pharmacopeia. 2008. *Birtish Pharmacopeia*, vol. **III,** 901 pp.

Brownlie, T.T., Utermohlen, V., Hinton, P.S., Giordano, C., Haas, J.D. 2002. Marginal iron deficiency without anemia impairs aerobic adaptation among previously untrained women. *The American Journal of Clinical Nature,* **75:** 734-742.

Campbell, H., Maguire, C., Kimble, R. 2018. Iron deficiency anaemia to laparotomy - a hair - raising tale. *Journal of Pediatric Surgery Case Reports*, **39:** 29-30.

Chandra, S., Tripathi, A.K., Mishra, S., Amzarul, M., Vaish, A.K. 2012. Physiological changes in hematological parameters during pregnancy. *Indian Journal of Hematology & Blood Transfusion: An Official Journal of Indian Society of Hematology and Blood Transfusion*, **28:** 144-146.

Feightner, J.W. 1994. Routine iron supplementation during pregnancy in Canadian task force on the periodic health examination. *Canadian Guide to Clinical Preventive Health Care Ottawa: Health Canada*, **64**.

Frewin, R., Henson, A., Provan, D. 1997. ABC of clinical haematology. Iron deficiency anaemia. *BMJ Journal*, **314:** 360-363.

Hallberg, L., Brune, M., Rossander, L. 1986. Effect of ascorbic acid on iron absorption from different types of meals. Studies with ascorbic-acid-rich

foods and synthetic ascorbic acid given in different amounts with different meals. *Human Nutrition. Applied Nutrition*, **40:** 97-113.

Krik-Oltmer Encyclopedia of Chemical Technology. 2005. vol. **14,** 5th edition, 490 pp.

Makrides, M., Crowther, C.A., Gibson, R.A., Gibson, R.S., Skeaff, C.M. 2003. Efficacy and tolerability of low-dose iron supplements during pregnancy: a randomized controlled trial. *The American Journal of Clinical Nutrition*, **78:** 145-153.

Martindale: The extra pharmacopoeia. 1977. 27th edition. https://doi.org/10.1111/j.2042-7158.1977.tb11428.x

Minár, M., Košutzká, Z., Habánová, H., Rusnák, I., Planck, K., Valkovic, P. 2015. Restless legs syndrome in pregnancy is connected with iron deficiency. *Sleep Medicine*, **16:** 589-592.

Percy, L., Mansour, D., Fraser, I. 2017. Iron deficiency and iron deficiency anaemia in women. *Best Practice and Research Clinical Obstetrics and Gynaecology*, **40:** 55-67.

United State Pharmacopeia /National Formulay. 2008. Asian edition, vol. **2,** 2154 pp.

WHO, World Health Organization. 2011. Haemoglobin concentrations for the diagnosis of anaemia and assessment of severity. https://apps.who.int/iris/handle/10665/85839.

Wiley Encyclopedia of Food Science and Technology. 1992. vol. **3,** 1817 pp., John Wiley & Sons, Inc. Canada.

Wong, C. 2017. Iron deficiency anaemia. *Paediatrics and Child Health*, **27:** 527-529.

Zaidi, S.A.H, Mahdihassan, S. 1962. Martindale extra pharmacopoeia. *Arzneim Forsch*, **12**.

Pak. j. sci. ind. res. Ser. A: phys. sci. 2021 **64A**(1) 10-18

Effect of Reinforced Glass Fibre on the Mechanical Properties of Polyamide

Raza Muhammad Khan and Asim Mushtaq*
Polymer and Petrochemical Engineering Department, NED University of Engineering & Technology, Karachi, Sindh, Pakistan

(received August 5, 2019; revised December 9, 2019; accepted January 7, 2020)

Abstract. The aim of this study is to enhance the tensile and flexural strength of polyamide (nylon 6, 6) by incorporation of glass fibre. Nylon has high elasticity, strength, toughness and maintain mechanical properties at elevated temperatures. The method employed for enhancement of properties is by the reinforcement of glass fibre. Glass fibre is the most extensively used reinforcement material. It is a lightweight, extremely solid, durable, low cost material that moderafly stiff. The composition of glass fibre was kept at 0 wt.%, 30 wt.% and 50 wt.% in nylon 6,6 blend. Initially, samples were manufactured by injection molding of nylon 6,6 and glass fibre. The pressure and velocity profiles at 0 wt.%, 30 wt.% and 50 wt.% reinforced nylon 6,6 are also compared. The samples thus formed were checked for shrinkage. The samples were tested for their tensile and flexural properties. The mechanical properties of polyamide (nylon 6,6) significantly improves by increasing glass fibre reinforcement.

Keywords: flexural strength, glass fibre, nylon 6,6, polyamide, tensile

Introduction

The term nylon is a conventional term used to describe a categery of synthetic polyamides that are synthetic. The amide group (– CONH–) in nylons forms some portion of the polymer fundamental chain. The chemical structure of nylons are divided into two categories, one based on dibasic acids or diamines and other based on lactams or amino acids. Nylons are referred by a numbering system that reveals the number of carbon atoms in their structure, like nylon 6 represents polycaprolactam (poly. ω-amino caproic acid). In the nylons family, nylon 6 and nylon 6.6 are of the utmost commercial importance as they offer good set of properties with economical cost. Other commercially useful materials like, e.g are nylon 6,9; nylon 6,10; nylon 6,12; nylon 11; and nylon 12, have relatively higher prices (Pickering *et al*., 2016).

Nylon 6 and nylon 6,6 have semi-crystalline structure with good durability and strength for challenging applications with their own distinct and separate benefits they do share some core properties such as good fatigue resistance, electrical insulating properties, sliding properties, resistance to high energy radiation, machinability and excellent wear resistance. It also has high mechanical damping ability, mechanical strength, stiffness, hardness and toughness (Pickering *et al*., 2016; Teixeira *et al*., 2015).

Althow nylon 6 and nylon 6.6 are very alike materials they also possess some different characteristics, these differences are due to different chemical structure. The nylon 6 consist of one monomer with 6 carbon atoms, while nylon 6,6 has 2 monomers with each one having 6 carbon atoms, therefore named as nylon 6,6 (Saba *et al*., 2014). Table 1 shows the comparison of different properties of nylon 6 and nylon 6,6. Also, nylon 6 endures high impact stress and stands up to hydrocarbons well while nylon 6,6 has improved stiffness, tensile and flexural modulus. Nylon 6,6 is a very common engineering thermo plastic used in plastic processing. Nylon 6,6 can be used with a different composition according to the requirement of the product. It shows very high flow in thin sections and has good weld

Table 1. Comparison of different properties of nylon 6 and nylon 6,6

Properties	Nylon 6	Nylon 6,6
Crystallinity	Less	More
Mold shrinkage	Lower	Higher
Melting point	Lower	Higher
Heat deflection temperature	Lower	Higher
Water absorption rate	High	Lower
Chemical resistance	Poor	Better

*Author for correspondence;
E-mail: engrasimmushtaq@yahoo.com.

strength. It is a hygroscopic compound and pre-drying is important. The crystalline melting point of nylon is 265 °C. It shows very high resistance towards wear because of its very high molecular weight. The major application of nylon includes nylon fibre, clothing, footwear, panty house, tooth brush bristles, finishing lines, air bag fibre, parachutes machine parts such as gears and bearing (Frihi *et al*., 2016).

The aim of this study is to use reinforced nylon 6,6 with 0 wt.%, 30 wt.% and 50 wt.% glass fibre and injection molding and to identify the difference in pressure and velocity profile, when used with three different glass fibre reinforcements by a graphical representation. In addition, the shrinkage factors, tensile strength, elongation modulus, elongation at break, flexural stress, flexural strain and flexural modulus for all the three reinforcements of glass fibre, will be discussed.

Materials and Methods

Polyamide and Nylon 6, 6 glass fiber reinforcments (toughness, low coefficient of friction, and good abrasion resistance) were purchased from Merck, Germany.

Injection molding. Injection molding is very common and popular in plastic processing techniques, in which molten material is injected into the cavity, allowing the material to cool down and solidify and eject the material. There are many ejection systems used to eject the material like pin ejection, sleeve ejection, air ejection, which depending upon the nature of the product and mold. Normally the injection molding machine is divided into two parts provided with the mold between injection and clamping unit (Nagakura *et al*., 2017). The injection unit consists of a screw motor, a barrel, a hopper, a heater band, a stationary plate and aninjection nozzle. The Barrel plays a vital role in the method of injection moulding process. It is also called the heating cylinder. Normally, it is made of an inexpensive grade of steel. The barrel is supported by an electrically activated heater band. Normally, the barrel is divided into three zones, unusual centre and front. The temperature is comparatively low in the rare zone and increasing consistently in the centre and front zone. The injection screw is placed inside the barrel. Screw design is very important in polymer processing and it may vary from material to material. The hopper is the component, where the plastic material is initially stored before it is injet to the barrel, its size depends on the machine size. Sometimes hopper is supported by dryer for drying of the material which is hygroscopic. The nozzle is the final component of the injection unit. The molten plastic is injected into the mold cavity with the help of a nozzle. A heater band is provided at the nozzle tip known as nozzle heater (Nagakura *et al*., 2017). The basic purpose of the clamping unit is to grip the mold throughout the injection process. The pressure in the clamping unit should be equal to the injection unit. The clamping unit normally has three types of systems, toggle or mechanical, hydraulic and third is the combination of mechanical and hydraulic clamping (Pickering *et al*., 2016).

Parameters of the injection molding process. In injection molding different parameters affect the product quality. Main processing parameters of the injection molding, process are temperature, pressure, time and distance. The variation in the temperature affects the injection molding process and the quality of the final product. It may include the melt temperature, mold temperature and even the ambient temperature. The melt temperature is normally maintained throughout the flow path, which starts from the hopper to machine barrel, then from machine barrel to nozzle. From the nozzle, it is injected into the mold cavity. The heating barrel has three zones, rear zone, centre zone and front zone. The temperature is gradually increases from the rear zone to front zone. The control of melt temperature is very important. The melting temperature of nylon 6 is 215 °C to 220 °C and nylon 6, 6 is 274 °C to 280 °C. After melting in the barrel, the material is now ready to flow into the mold, where the material will cool down. The cooling rate depends upon the material and the design of the product. The mold temperature of nylon 6 is 93 °C and nylon 6,6 is 79 °C (Essabir *et al*., 2018; Saba *et al*., 2014). Injection molding machines comprise of two units, injection and clamping unit. Both the two units require pressure and pressure control. The pressure in the clamp unit is required to overcome the pressure of the injection unit. There are three basic types of pressures in the injection unit, which are the initial injection, holding and backup pressures. The initial pressure is used to push the molten plastic. It is normally operated by hydraulic pressure. As a result of this pressure, the initial filling of the mold takes place. The holding pressure is also called secondary pressure, it is used with molten plastic for the final filling of the mold and holds it till the molten plastic solidifies. Shrinkage factor has been reduced by holding pressure.

Holding pressure is used to finish the filling of the mold. After the holding pressure, the back pressure is applied to the machine. Usually, the back pressure is small as compared to injection pressure. The back pressure is used to control the part weight, density and product appearance. During the injection process in the clamping unit, pressure is used to close the mold. The amount of injection and clamp force must be equal (Palazzetti, 2015).

Injection molding of nylon 6, 6. In the lab, the nylon 6,6 is used for experimental work and for the processing in injection moulding machine to make the test specimen for the tensile and flexural test. Nylon 6, 6 is taken with three different reinforcements of glass fibre that is nylon 6,6 with o wt.% glass fibres. Nylon 6,6 with 30 wt.% glass fibre and nylon 6,6 with 50 wt.% glass fibre. Table 2 shows the injection molding process parameters.

Shrinkage calculations. Shrinkage is calculated for tensile and flexural bar produced specimens by taking the difference of mold dimensions and specimen dimensions. The dimension of the mold cavity is measured by micro meter screw gauge when the width is 10.05 mm and thickness 2.39 mm for tensile bar and width is 10.06 mm and thickness is 4.03 mm, for flexural bar.

Tensile testing. The tensile test is a mechanical test of the material in which the behaviour of a material is determined under uni axial stretch loading. The elongation, elastic modulus, tensile strength and yield strength and other properties can be measured by using the data of the test. It is a quiet simple test to get a good tensile profile. The point of failure is normally referred to as ultimate strength. The stress σ (have been calculated by eq. (1). Figure 1 represents the specimens used for tensile testing manufactured on injection molding.

$$\sigma = \frac{\text{Load}}{\text{Cross} - \text{sectional area}} \quad \ldots\ldots 1$$

The ratio of stress and strain is called Hook's Law, which is normally constant and determined by eq. (2).

$$E = \frac{\text{Strees } (\sigma)}{\text{Strein } (\epsilon)} \quad \ldots\ldots 2$$

When the stress is proportional to strain, then it is called modulus of elasticity. The stiffness of the material is measured by the modulus of elasticity. It is the linear region of the curve. At this point, some permanent deformation starts to occur in the specimen. This point is normally referred to as proportional limit. At this point when the stress is removed, the material will not come to its original position. The 30 different samples have been tested for tensile properties. In these 30 samples, 10 samples are reinforced with 0 wt. % glass fibre, 10 samples with 30 wt. % glass fibre reinforcement and remaining 10 are 50 wt. % reinforced with glass fibre as shown in Table 3. All these specimens are manufactured on injection molding.

Flexural testing. The ability of a material to withstand bending forces applied perpendicular to its longitudinal axisis known as flexural strength. Flexural strength is

Table 2. Process parameters for injection moulding

Parameters	Units	Zone	0 wt.%	30 wt.%	50 wt.%
Barrel temperature (°C) 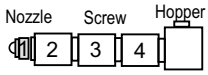	°C	1	310	310	310
		2	295	295	295
		3	295	295	295
		4	280	280	280
Mold temperature	°C	-	93	93	93
Shot size	mm		36.0	36.75	38.5
Injection velocity	mm/s		45	45	45
Transfer position	mm		10	10	10
Packing pressure	bar		375	375	375
Packing time	sec		19	19	19
Decompression distance	mm		3	3	3
Plasticization screw speed rpm			75	75	75
Plasticization back pressure	bar		50	50	50
Cooling time	sec		15	15	15

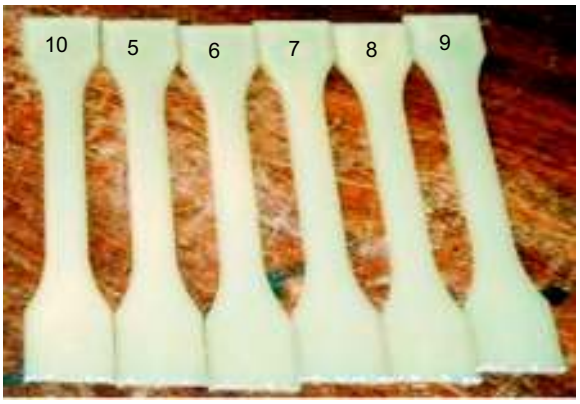

Fig. 1. Specimens used for tensile testing manufactured on injection molding.

Table 3. Tensile test data for 0 wt.%, 30 wt.% and 50 wt.% glass fibre reinforcement

Sample	Glass fibre	Time 'sec' wt.%	Load 'N'	Stroke 'mm'
1	0	34929.11	1018.36	2.879
2		151730.5	1441.056	12.61
3		135479.8	1428.059	11.263
4		138029.9	1424.617	11.476
5		122529.7	1428.608	10.179
6		35079.11	1011.957	2.891
7		115629.8	1384.97	9.609
8		120380.5	1418.92	10.005
9		150079.9	1450.82	12.483
10		28029.25	2453.26	2.309
11	30	28029.25	2453.26	2.309
12		26829.21	2430.266	2.209
13		27929.24	2473.81	2.3
14		34899.34	2401.206	2.879
15		30428.97	2476.67	2.504
16		31130.45	2045.78	2.563
17		29629.26	2473.58	2.443
18		30732.06	2437.1	2.53
19		35099.34	2253.21	2.89
20		29829.29	2381.32	2.459
21	50	29799.22	3511.43	2.454
22		29479.28	3446.68	2.430
23		34979.4	318.82	2.888
24		29401.51	3411.74	2.421
25		32129.34	3398.74	2.651
26		30428.97	3321.25	2.504
27		30529.31	3363.39	2.571
28		31198.93	3374.27	2.566
29		34429.09	3270.99	2.837
30		27780.68	3400.44	2.288

the combination of different stresses which include tensile stresses and compressive stresses. The calculation of flexural properties is done regarding stress and strain. Many polymers do not break, while testing flexural properties because it is a bending test and deflection is observed in these kinds of test. Three-point bending and four-point bending methods are used to determine the flexural properties. Normally the three-point bending method is used for the material which shows small deflection and four-point bending methods is used for the material which shows larger deflection during testing. In the flexural test the maximum stress can be obtained by the eq.(3) (Withers *et al*., 2015).

$$\text{Flexural stress} = \frac{3PL}{2w\,T^2} \quad \text{..... 3}$$

where:

'P' denotes the load, 'L' represents length of span, 'w' indicate the width of the specimen and 'T' for the thickness of the specimen. The flexural strain is calculated by the eq. (4).

$$\text{Flexural strain} = \frac{6DP}{L^2} \quad \text{..... 4}$$

where:

'D' is the deflection, 'T' is the thickness of the specimen and 'L' is the length of the span.

While, doing the flexural test, specimen preparation, temperature and test conditions may affect the test results. It is also called flexural modulus that measures the stiffness of material during the first bending process as given in eq. (5) (Chaichanawong *et al*., 2016). The procedure for calculating the flexural modulus is quite

Table 4. Flexural test data for 0 wt.%, 30 wt.% and 50 wt.% glass fibre reinforcement

Sample	Glass fibre wt.%	Time 'sec'	Load 'N'	Stroke 'mm'
31	0	35229.4	8.25267	2.91058
32		32381.41	8.22894	2.6735
33		31229.32	7.86097	2.57932
34		30581.1	8.25847	2.52349
35		30879.35	8.269	2.54832
36		30899.25	7.355	2.54829
37		30629.31	7.95389	2.52766
38		30679.31	7.44169	2.53162
39		30979.32	7.51479	2.55683
40		36749.37	8.63706	3.03536
41	30	31079.32	26.2042	2.56495
42		36680.14	31.9799	3.03193
43		30799.25	26.1726	2.53953
44		30979.32	26.148	2.55662
45		30680.81	26.8317	2.53116
46		31279.33	27.0856	2.5814
47		30648.91	25.62	2.52244
48		30978.87	26.632	2.55164
49		30678.98	25.2232	2.52682
50		30978.99	25.5128	2.55161
51	50	31069.19	46.0038	2.56078
52		31579.56	47.7945	2.60606
53		20828.85	32.1127	3.36771
54		30599.24	45.4467	2.52328
55		30749.25	45.6067	2.53599
56		30728.98	45.6265	2.53078
57		31059.39	46.5317	2.56432
58		30979.32	46.2518	2.55662
59		30929.32	46.7502	2.55203
60		30928.99	45.7217	2.54744

similar to the procedure of calculating tensile modulus. In many cases values of flexural modulus and tensile modulus are same. The 10 samples of Nylon 6,6 with glass fibre reinforcement of 0 wt.%, 30 wt.% and 50 wt.% were used for flexural testing. All these test bars were manufactured on injection molding. Table 4 represents the flexural test data for 0 wt.%, 30 wt.% and 50 wt.% glass fibre reinforcement.

$$\text{Flexural modulus} = \frac{\text{Flexural stress}}{\text{Flexural strain}} \quad \ldots\ldots\ldots\ldots\ldots 5$$

Results and Discussion

Pressure-velocity profile. According to the data provided for processing of nylon 6,6 it looks quite similar as shown in Table 2 for all the three materials, but certain differences changes have been observed in pressure velocity profile, which is shown in Fig. 2.

When nylon 6,6 is used with 0 wt.% glass fibre reinforcement, the initial injection pressure is not very high. That means low injection pressure is required to fill the mold cavity initially, then the pressure drops and constant holding pressure is applied to the mold. When the nylon is used with 30 wt.% glass fibre reinforcement, the initial injection pressure is quite higher as compared to the pressure that was observed in the processing of nylon 6,6 with 0 wt.% glass fibre reinforcement. However, the holding pressure looks constant for both the material but a wide difference has been observed between the initial injection pressure and holding pressure. When nylon 6,6 is used with 50 wt.% glass fibre reinforcement the initial injection pressure is relatively very high as compare to 0 wt.% and 30 wt.% glass fibre reinforcement. It was observed that increasing % glass fibre reinforcement would increase the initial pressure for pushing molten plastic to the mold cavity. This is because the melt viscosity will gradually increase due to the higher crystallinity in nylon 6,6 structure as two monomers contain 6 carbon atoms for each. The findings are accordance with the previous literature (Garcia *et al*., 2018; Fernandes *et al*., 2017; Bernasconi *et al*., 2015).

Shrinkage for tensile and flexural bar. Figures 3 and 4 representing the results for both tensile and flexural bars revealed that, the % of shrinkage increases with the increase is glass fibre reinforcement in both the direction that is in width and thickness. The mould

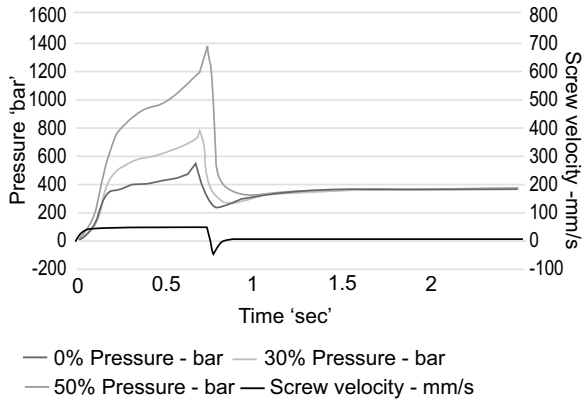

Fig. 2. Pressure-velocity profile comparison of nylon 6,6 with 0 wt.%,30 wt.% and 50 wt.% glass fibre reinforcement.

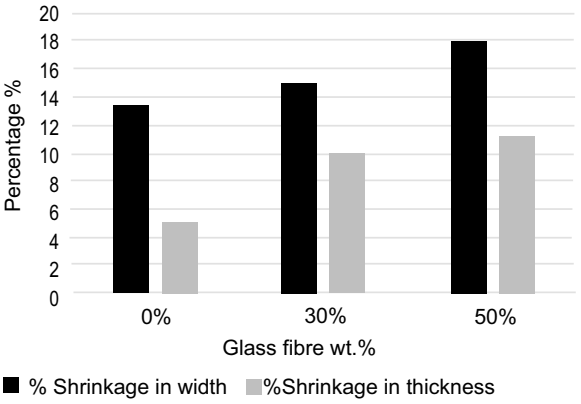

Fig. 3. Comparison between the percentage of shrinkage in width and thickness for the specimens of the tensile test.

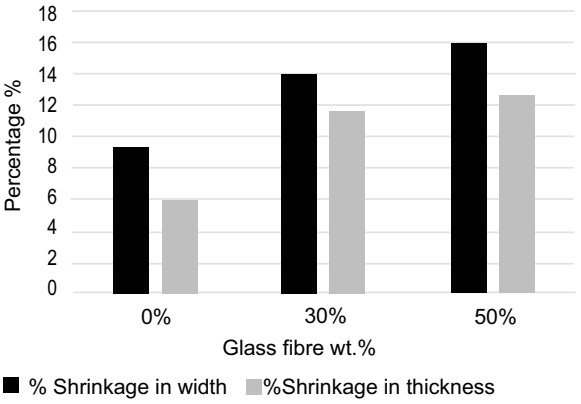

Fig. 4. Comparison between percentage shrinkage in width and thickness for the specimens of flexural test.

shrinkage of nylon 6,6 is further incresed by the re-bonding of glass fibre during the injection process and bonding strength has been increased. Table 5 is the summarized form of shrinkage results for tensile and flexural bar specimen with 0 wt. %, 30 wt. %, 50 wt. % glass fibre reinforcement. The present research work traced by the previous work.

The mechanical property of glass fibre filled polyamide composites are directed by the distinct properties of the fibre and blend, along with a multifaceted incorporation of some parameters such as fibre size, content, distribution and orientation, as well as physicochemical collaborations at the polymer-fiber interface (Graupner *et al*., 2016; Arif *et al*., 2014; Feldmann and Bledzki, 2014).

Tensile result of glass fibre reinforcement. Figure 5 represents the specimen of Nylon 6,6 with 0 wt.%, 30 wt.% and 50 wt.% glass fibre reinforcement after tensile testing. The obtained results revealed that with increasing the amount of glass fibre the tensile strength and elastic modulus is increasing significantly, whereas % elongation is decreasing as shown in Fig. 6 to 8. This means increasing the amount of glass fibre, increases the strength of the final product. The tensile test results for 0 wt.%, 30 wt.%, and 50 wt.% glass fibre reinforcement are shown in Table 6.

Table 5. Shrinkage results for tensile and flexural bar specimen with 0 wt. %, 30 wt. % and 50 wt. % glass fibre reinforcement

Shrinkage calculation	Glass fibre wt. %	Width 'mm'	Thickness 'mm'	% Shrinkage in width	% Shrinkage in thickness
Tensile bar	0	9.914	2.34	13.6	5
	30	9.90	2.29	15	10
	50	9.87	2.279	18	11.1
Flexural bar	0	9.967	3.971	9.3	5.9
	30	9.92	3.914	14	11.6
	50	9.903	9.903	15.7	12.6

According to the literature percentage elongation decreases due to rigid fibres restrain matrix deformation persuading strength gain and brittleness of the resultant

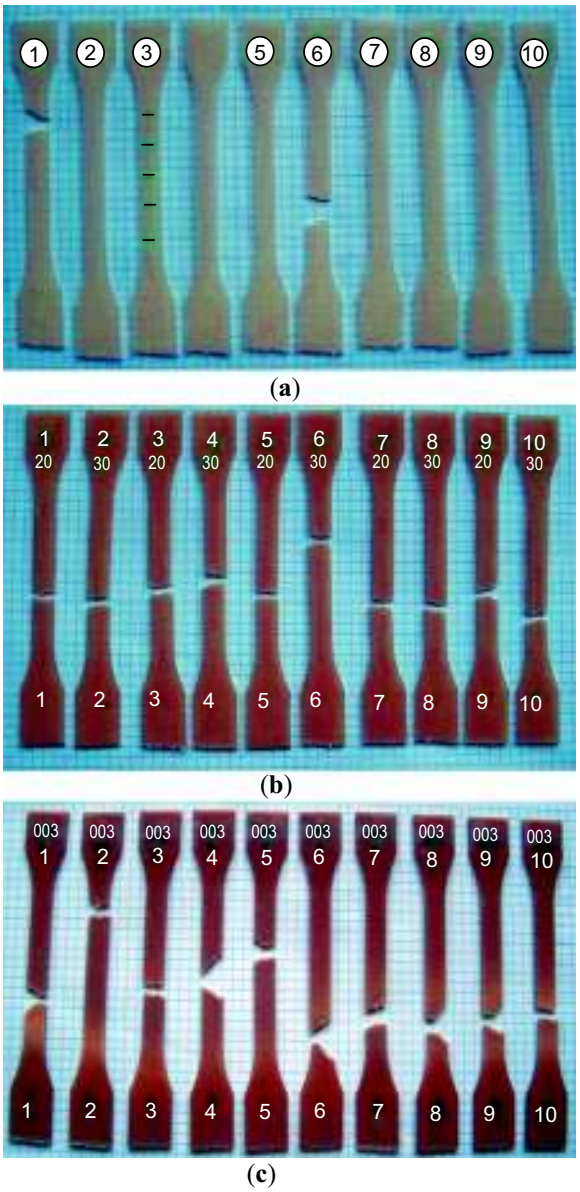

Fig. 5. Specimen of nylon 6, 6 with (**a**) 0 wt.%, (**b**) 30 wt.% and (**c**) 50 wt.% glass fibre reinforcement after tensile test.

Table 6. Tensile test results for 0 wt.%, 30 wt.% and 50 wt.% glass fibre reinforcement

Glass fibre reinforcement wt. %	Load 'P' N	Width 'w' m	Thickness 'T' m	Tensile strength M. Pa	Strain	%Elongation	Elastic modulus G. Pa
0	1450.82	0.009914	0.00234	62.53	0.24966	24.966	0.250
30	2401.20	0.00990	0.00229	105.915	0.05758	5.758	1.839
50	3411.74	0.00987	0.002279	151.68	0.04842	4.842	3.132

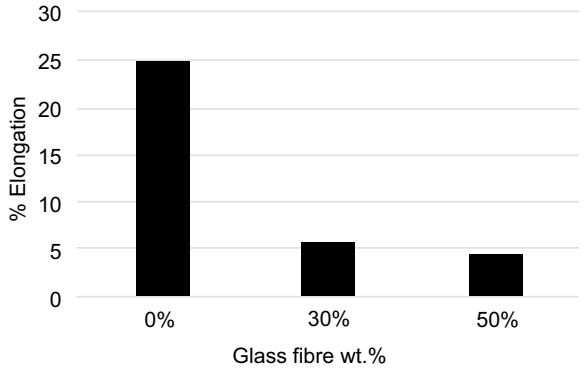

Fig. 6. Effect of % elongation for three sample of nylon with different wt. % reinforcement of glass fibre.

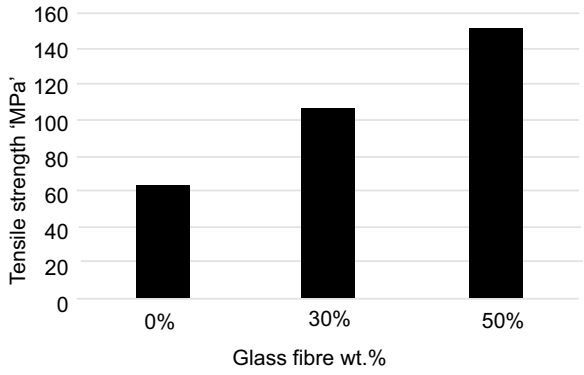

Fig. 7. Effect of tensile strength for three sample of nylon with different wt. % reinforcement of glass fibre.

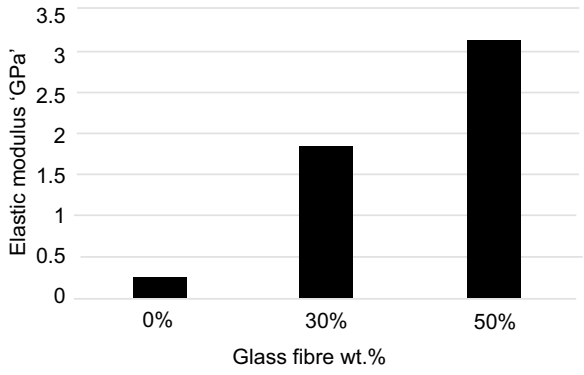

Fig. 8. Effect of elastic modulus for three sample of nylon with different wt. % reinforcement of glass fibre.

composites. Usually in polymer composites, glass fibres are used to increases the tensile properties. Numerous studies about glass fibre reinforced polymers have reported that increasing composition of glass fibre in the matrix (nylon 6,6), interfacial interactions leads to better load transfer. On the whole, the absence of agglomeration shows good affinity among the glass fibre and the nylon 6,6, that indicates good manufacturing conditions were used (Graupner *et al*., 2016; Ning *et al*., 2015; Sethi and Ray, 2015).

The nylon 6,6 with 50 wt.% glass fibre reinforcement represent high tensile strengths and elastic modulus. The highest value of strength and modulus were perceived for the glass fibre composites, attributable to higher strength, stiffness, better interfacial bonding of glass fibre (Basso *et al*., 2019; Mortazavian and Fatemi, 2015).

Flexural result of glass fibre reinforcement. Figure 9 shows that as the amount of glass fibre increases in nylon 6,6, the value of flexural modulus increases. When nylon 6,6 is used with 0 wt.% glass fibre reinforcement, the value for flexural modulus is very low, but it increases significantly. It means that stiffness of the material increases with the increase in glass fibre. Table 7, represents the summarized form of flexural test results for 0 wt.%, 30 wt.%, and 50 wt.% glass fibre reinforcement.

The reinforcement of glass fibre in the nylon 6,6 led to a change in mechanical properties also depending on the temperature and running conditions. This is anticipated as a result of the high modulus of glass fibre. However, all the results proved that nylon 6,6 make the interactions amongst the components stronger and this is proved by the solid-like behaviour of the composite at higher composition of glass fibre. The

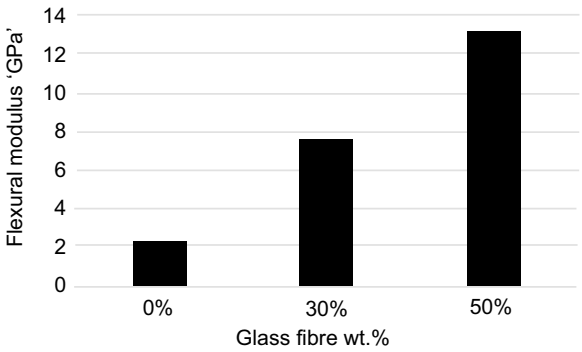

Fig. 9. Effect of flexural modulus on three sample of nylon with different wt. % reinforcement of glass fibre

Table 7. Flexural test results for 0 wt.%, 30 wt.% and 50 wt.% glass fibre reinforcement

Glass fiber reinforcement wt. %	Load 'P' N	Width 'w' m	Thickness 'T' m	Length 'L' m	Flexural stress M. Pa	Flexural strain	Flexural modulus M. Pa
0	8.25847	0.00996	0.00397	0.12	9.46	0.00417	2268.58
30	26.1726	0.00992	0.00389	0.12	31.384	0.004116	7624.59
50	45.7217	0.00991	0.0039	0.12	54.599	0.004139	13189.47

results obtained are in good agreement with previous literature concerning fiber reinforced composite (Garcia *et al*., 2018; Nagakura *et al*., 2017; Mortazavian and Fatemi, 2015).

Conclusion

In this study shrinkage calculations gave an approximate result that shrinkage regarding width and thickness increases from 0 wt. % to 50 wt.% samples. It was found that as percentage reinforcement increases percentage shrinkage increases at a lesser rate. The penultimate tensile test and its succeeding calculations declared that the tensile strength and elastic modulus significantly increased from 0 wt.% to 50 wt.% samples, whereas percentage elongation decrease. Synonymously, the concluding flexural test and its succeeding calculations showed a significant increase in flexural strength and flexural modulus from 0 wt.% to 50 wt.% glass fibre reinforced polyamide samples. Hence, it was concluded that mechanical properties of polyamide (nylon 6,6) significantly improve by increasing glass fibre reinforcement. The future recommendation is, shrinkage can be lowered by varying packing or holding pressure to changing in process parameters. Talc also can be used as reinforced material since it is cheap and will provide ease in processing.

Acknowledgement

The authors would like to acknowledge the Department of Polymer and Petrochemical Engineering, NED University of Engineering & Technology, Karachi, Pakistan for supporting this research work.

Conflict of Interest. The authors declare no conflict of interest.

References

Arif, M.F., Saintier, N., Meraghni, F., Fitoussi, J., Chemisky, Y. 2014. Multiscale fatigue damage characterisation in short glass fiber reinforced polyamide-66. *Composites Part B: Engineering*, **61:** 55-65.

Basso, M., Piselli, A., Simonato, M., Furlanetto, R., Pupure, L. 2019. Effect of food chemicals and temperature on mechanical reliability of bio-based glass fibers reinforced polyamide. *Composites Part B: Engineering*, **157:** 140-149.

Bernasconi, A., Conrado, E., Hine, P. 2015. An experimental investigation of the combined influence of notch size and fibre orientation on the fatigue strength of a short glass fibre reinforced polyamide 6. *Polymer Testing*, **47:** 12-21.

Chaichanawong, J., Thongchuea, C., Areerat, S. 2016. Effect of moisture on the mechanical properties of glass fiber reinforced polyamide composites. *Advanced Powder Technology*, **27:** 898-902.

Essabir, H., Rodrigue, D., Bouhfid, R., Qaiss, A.E.K. 2018. Effect of nylon 6 (PA6) addition on the properties of glass fiber reinforced acrylonitrile-butadiene-styrene. *Polymer Composites*, **39:** 14-21.

Feldmann, M., Bledzki, A.K. 2014. Bio-based polyamides reinforced with cellulosic fibres – processing and properties. *Composites Science and Technology*, **100:** 113-120.

Fernandes, F.C., Gadioli, R., Yassitepe, E., Paoli, M.A.D. 2017. Polyamide-6 composites reinforced with cellulose fibers and fabricated by extrusion: Effect of fiber bleaching on mechanical properties and stability. *Polymer Composites*, **38:** 299-308.

Frihi, D., Layachi, A., Gherib, S., Stoclet, G., Masenelli-Varlot, K. 2016. Crystallization of glass-fiber-reinforced polyamide 66 composites: Influence of glass-fibre content and cooling rate. *Composites Science and Technology*, **130:** 70-77.

Garcia, C., Trendafilova, I., Zucchelli, A. 2018. The effect of polycaprolactone nanofibers on the dynamic and impact behavior of glass fibre reinforced polymer composites. *Journal of Composites Science*, **2:** 43.

Graupner, N., Albrecht, K., Ziegmann, G., Enzler, H., Müssig, J. 2016. Influence of reprocessing on fibre

length distribution, tensile strength and impact strength of injection moulded cellulose fibre-reinforced polylactide (PLA) composites. *Express Polymer Letters*, **10:** 647-663.

Mortazavian, S., Fatemi, A. 2015. Effects of fibre orientation and anisotropy on tensile strength and elastic modulus of short fiber reinforced polymer composites. *Composites Part B: Engineering*, **72:** 116-129.

Nagakura, M., Tanimoto, Y., Nishiyame, N. 2017. Effect of fiber content on flexural properties of glass fiber-reinforced polyamide-6 prepared by injection molding. *Dental Materials Journal*, **36:** 415-421.

Ning, F., Cong, W., Qiu, J., Wei, J., Wang, S. 2015. Additive manufacturing of carbon fiber reinforced thermoplastic composites using fused deposition modeling. *Composites Part B: Engineering*, **80:** 369-378.

Palazzetti, R. 2015. Flexural behaviour of carbon and glass fiber composite laminates reinforced with nylon 6,6 electrospun nanofibers. *Journal of Composite Materials*, 1-7.http://doi.org110.1177/0021998314565410.

Pickering, K.L., Efendy, M.G.A., Le, T.M. 2016. A review of recent developments in natural fibre composites and their mechanical performance. *Composites Part A: Applied Science and Manufacturing*, **83:** 98-112.

Saba, N., Tahir, P.M., Jawaid, M. 2014. A review on potentiality of nano filler/natural fiber filled polymer hybrid composites. *Polymers*, **6:** 2247-2273.

Sethi, S., Ray, B.C. 2015. Environmental effects on fibre reinforced polymeric composites: evolving reasons and remarks on interfacial strength and stability. *Advance of Colloid Interface Science*, **217:** 43-67.

Teixeira, D., Giovanela, M., Gonella, L.B., Crespo, J.S. 2015. Influence of injection molding on the flexural strength and surface quality of long glass fibre-reinforced polyamide 6.6 composites. *Materials and Design,* **85:** 695-706.

Withers, G.J., Yu, Y., Khabashesku, V.N., Cercone, L., Hadjiev, V.G. 2015. Improved mechanical properties of an epoxy glass–fibre composite reinforced with surface organomodified nanoclays. *Composites Part B: Engineering*, **72:** 175-182.

Pak. j. sci. ind. res. Ser. A: phys. sci. 2021 **64A**(1) 19-25

Phase, Microstructural Characterization and Beneficiation of Iron Ore by Shaking Table

Sajad Ali*, Fahad Nawaz and Yaseen Iqbal
Materials Research Laboratory, Department of Physics, University of Peshawar, Peshawar-25120, Pakistan

(received Feburary 25, 2019; revised June 20, 2019; accepted July 2, 2019)

Abstract. To know about the nature of gangue associated with the ores, characterization has become an integral part in mineral processing and beneficiation, therefore, the as-mined iron ore collected from Karak region of KP has been characterized for its phase, microstructure and chemical composition *via* XRD, SEM and EDS respectively. Beneficiation of the iron ore has been carried out by shaking table and magnetic separator. XRD analysis confirmed the presence of iron oxide (Fe_2O_3) as the major phase along with quartz (SiO_2) as the minor phase. Finely grinded iron ore powder of 100 (149 μm) and 200 (74 μm) mesh sizes were passed via shaking table and magnetic separator subsequently. The iron ore was successfully upgraded from 28.27 wt.% to 36.51 wt.% at 100 mesh and 38.70 wt.% at 200 mesh *via* shaking table, thus achieving a maximum of 10% upgraded iron ore. The magnetic separator did not become so effective due to non-magnetic nature of hematite.

Keywords: iron ore, shaking table, microstructure, phase, minor magnetic seprator

Introduction

With increasing global demand of steel and rapid depletion of high grade iron ores, the utilization of low-grade iron ores acquired much attention in recent years. Complex mineralogy, high content of silica and other gangue minerals are the major difficulties in the processing and use of low grade iron ores. Thus, up-gradation of low grade iron ores to remove the gangue minerals and enhance their quality is a major area of research today (Ali 2004; Ali *et al.,* 2003; Abu-zeid 1967). In most of the known iron ore deposits in Pakistan, many deposits are low grade and needs proper beneficiation, so as to produce and fulfill the requirement of the steel making.

Iron ore deposit of Karak (KP) Pakistan is of low grade and the problem in up-grading this ore deposit is twofold. Firstly, it occur as a mixture of hematite and silica, and secondly, the fine dissemination of iron mineral in silica and silicates, which requires fine grinding to obtain adequate degree of liberation of the desired iron mineral and the gangue constituents.

Gravity and magnetic separation are the economical and most commonly used beneficiation techniques recovery of valuables from natural ores (Burt, 1999). Although other techniques i.e. hydrocyclon, jigging, spirals, flotation and magnetic separation partially replaced the gravity separation method but they have not made it obsolete. Due to the lowcost, ease of operation, and eco-friendly nature, the gravity separation techniques is widely used in mineral beneficiation practices, since it is based on the principle of settling velocities of the constituents of particles in ore (Mukherjee *et al.,* 2006).

The influential factors in the shaking table and jigging techniques that govern the settling velocity of ore particles include the weight (volume and density) of particles, buoyancy and drag forces (Roy, 2009). Being a powerful technique to recover fine particles of the valuable minerals, many researchers investigated the theoretical and experimental performance of shaking table (Mansar *et al.,* 1991; Gaudin, 1987; Shivamohan 1985). Shaking table efficiency has been reported to be high if the difference in specific gravity is high between valuable and gangue minerals (Samykina, 2005). For the beneficiation of iron ore, a single step magnetic separation cab be performed, if the nature of ore is magnetic and the gangue is nonmagnetic. However, if the ore is non-magnetic then a combination of magnetic separation along with gravity separation can be applied (Svoboda, 1994; Svoboda *et al,*. 1989).

Guney studied the beneficiation of Camdag hematite ore that is composed of limonite-hematite interlocked in each other. Using a combination of gravity separation and high intensity magnetic separation techniques he

*Author for correspondence; E-mail: sajjad2485@yahoo.com

successfully increased the ore grade from 5 - 7% in concentrates with ~ 60% recovery by both methods (Guney, 2000).

Abouzeid (Abu-zeid, 1967) worked on the beneficiation of El-Gedida iron ore using high intensity magnetic separator. An ore sample containing 51.6% Fe, 8.76% SiO_2 and 3.06% BaO was studied and successfully point out that high intensity magnetic separator was limited to ore size of 2 and 0.125 mm. The final magnetic product assayed 61% Fe at an iron recovery of 90.3%. However, 5% by weight was obtained as middling assaying 31.4% Fe. These middling products, together with the fine fraction minus 0.125mm which constitute 35% by weight of the whole sample, were not possible to be upgraded by magnetic separation.

Rowayshed (Rowayshed, 1983) investigated the beneficiation of El-Gedida iron ores using high intensity magnetic separator with limit up to 2 mm and concluded that neither the coarse nor the very fine sizes of ores can be treated using this technique. The dominant iron minerals present in this ore are the hydrated minerals, goethite and hydro-goethite, which are difficult to treat through high intensity magnetic separator. (Fatma *et al*., 1999) studied the beneficiation of iron ore sample containing 44% Fe, 1.59% SiO_2 and 20% BaO using magnetic separation. After cleaning several times an iron concentrate assaying 58.48% Fe, and 0.73% BaO is obtained. Faraghaly in 2002 studied an iron ore containing 23.5% Fe and 34% BaO. The beneficiation of iron ore was carried out using a dry high intensity magnetic separator and found a concentrate containing 56.78% Fe and 1.61% BaO at a recovery of 82.76%.

According to the Geological Survey of Pakistan (GSP) the total estimated reserves of different grades of iron ore in Pakistan are > 1.5 billion tons; however, there is only ~ 30,000 tons/year capacity for commercial mining. With further exploration, in depth geological study and appropriate mining techniques a medium scale steel plant can be installed using the local iron ore to fulfill the steel demand of the country (Shah *et al*., 2004; Kazmi *et al*., 2001; Siddiqui *et al*., 2000).

The major aim of this study was to investigate phase, microstructure and possible up-gradation of low-grade iron ore of Karak region via gravity and magnetic separation. The sieve parameters of 100 and 200 mesh sizes of iron ore were investigated through shaking table (exploiting the difference in specific gravity of the constituents in ore) and magnetic separator (exploiting the differences in magnetic susceptibility of the constituents in ore) were investigated.

Materials and Methods

The representative sample was collected from active mines of iron of Karak region, Khyber Pakhtunkhwa (KP), Pakistan. The sample was washed, dried and ground using a stainless steel mortar and pestle in Materials Research Laboratory (MRL), University of Peshawar. The powdered sample was sieved through 100 (149 μm) and 200 mesh (74 μm) size according to the US standards in MRL. A JEOL 3532, X-ray diffractometer with Cu Kα (λ ~ 1.54Å) radiations operating at 40 KV and 30 mA at Centralized Resource Laboratory (CRL) was used for phase analysis. For microstructural analysis, ~ 4×4×4 mm^3 piece was cut from iron ore sample with a TeckCut 4TM precision low speed diamond saw (Allied High Tech. Products, USA) in MRL. The sample was finely polished with a TwinPrep 3TM grinding/polishing machine (Allied High Tech Product, USA) using various grades of sand-paper (silicon carbide) and diamond paste on imperial adhesive back polishing cloth using water as a lubricant in MRL. The smooth polished surfaces were chemically etched in 40% hydrofluoric acid (HF) fumes for one minute. For SEM, the polished sample was mounted onto aluminum stub with silver paint and gold-coated to avoid charging in the SEM. The surface morphology and approximate size of the grains and micro-regions were examined using a JEOL JSM 5910 SEM. Elemental analysis were carried out using energy dispersive X-ray electron spectroscopy (EDS) coupled with SEM. A PMG-3 microscope coupled with a DP-12 CCD camera, Olympus (Japan) was used for recording optical images in the present study at CRL. For physical beneficiation via shaking table and magnetic separator, ~ 100 Kg iron ore was crushed in jaw and roller crushers and grinded in a ball mill to get fine powder up to 100 and 200 mesh at the Multipurpose Mineral and Metallic Ore Up-gradation Plant (MPMMOUP), Department of Physics, University of Peshawar.

The shaking table surface is made of 2 mm thick fibre glass with dimensions of chassis length (2450 mm) and width (1200 mm) connected with an adjustable variable speed induction motor (0.75 KW / 1 Hp) to generate back and forth movement and shake the table surface. Height of shaking table from floor surface depends on the angle of the table. The magnetic separator used in present study consists of a permanent cylindrical magnet

of 300 mm diameters and 460 mm length driven by a 0.75 KW / 1 Hp induction motor with a speed reducer with a ratio of 1:30. Both the shaking table and magnetic separators were locally manufactured and supplied by Mobashir Engineers, Peshawar.

Results and Discusssion

Figure 1 shows room temperature XRD pattern of the as-mined iron ore. The inter planer spacing (d-values) and relative intensities corresponding to the major XRD peak recorded for iron ore matched PDF # 5 – 490 for quartz of silicon oxide SiO_2 indicating to be major phase in the examined sample.

Additionally some peaks matched PDF # 6 – 502 for Iron Oxide Fe_2O_3 (Hematite) with main peaks appearing at 2θ of 33°, 36°, 56° and 68° as shown in Figure. Some peaks appeared to overlap with each other at 2θ of 36°, 56° and 68°. The experimental d-values and intensities of the as-mined iron ore is given in Table 1.

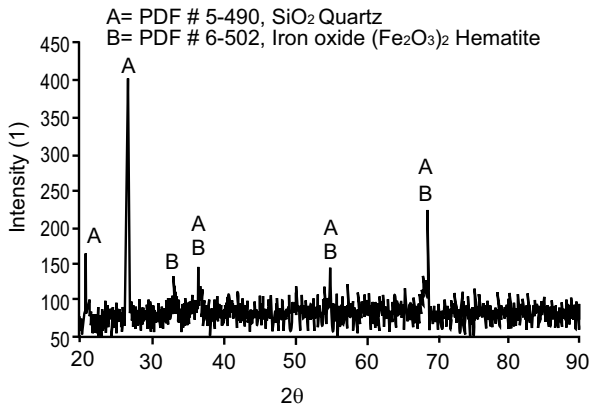

Fig. 1. XRD pattern of as-mined iron ore showing presence of Quartz (labeled as A) as the major phase along with iron oxide (Hematite) as minor phase (B).

The microstructure and the distribution of the impurities within the matrix of iron ore was investigated and analysed using reflected light optical microscopy and scanning electron microscopy (SEM). Figure 2 shows the reflected light micrograph of chemically etched (40 % HF fumes for 50 sec) iron ore sample showing the presence of three contrasted microregions with different texture and appearance. The micro region with dark grey texture comprising quartz, appearing as a plane and smooth surface with crystalline plates of irregular shapes (marked as "A") with size ranging from 10 – 70 mm. The rough microregion with whitish appearance is Hematite matrix (marked as "B") and is very finely immersed along the grain boundary and cracks of the large platy type silica grains. The hematite grains are very finely immersed though out the matrix and the

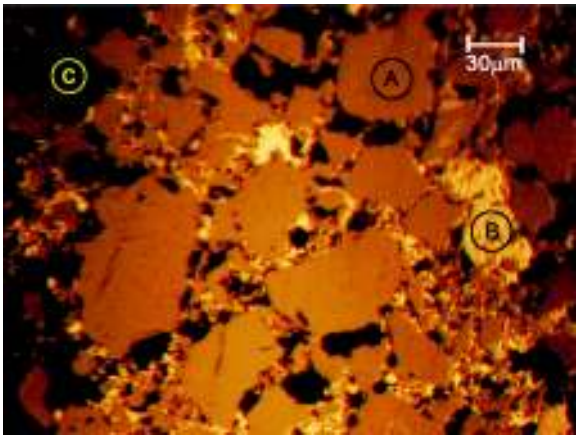

Fig. 2. Reflected light micrograph of iron ore showing dark grey quartz micro-region marked as "A", the rough micro-region with whitish contrast of hematite marked as "B" and black opaque contrast of magnetite marked as "C".

Table 1. comparison of d-value and relative intensity for observed XRD pattern of as-mined iron ore

Iron ore sample		PDF # 5- 490, SiO_2 Quartz			PDF # 6- 502, Iron oxide (Fe2O3), Hematite		
d-value	I/Io	d-value	I/Io	(hkl)	d-value	I/Io	(hkl)
3.34	100	3.34	100	(101)	--------	-------	
4.28	25	4.26	35	(100)	-------	-------	
2.70	23	-------	-----		2.69	100	(104)
2.46	27	2.45	12	(110)	2.51	80	(113)
1.67	26	1.67	7	(202)	1.69	80	(110)
1.36	49	1.37	11	(203)	1.38	20	(100)

grain size ranges from 5 – 25 mm. The blackish and opaque grains of roughly rectangular and rounded shape may appear to be magnetite (marked as "C"), with an average grain size to be ~ 15 µm (Miaha *et al.,* 2009).

All the three type morphologies are non-uniformly immersed among each other with no clear boundaries among them. Since the average size of the identified hematite grain is ~ 50 µm as clear in the Fig. which showed that the representative iron ore must be crushed to a mesh size of ~ 300 (47µm) in order to unlock the hematite grains from the gangue.

Figure 3 shows the secondary electron SEM image (SEI) of as-mined iron ore sample demonstrated the presence of two distinct microregions i.e. plane micro-region with grey contrast and rough microregion with whitish contrast. The grey plane microregion with platy type morphology of large irregular shape labeled as "A" is quartz. The average size of the quartz is ~ 30 mm, with grains ranges in size from 10 – 90 µm. The rough and granular type white microregion/grains labeled as "B" is hematite. The hematite grains are observed to be irregular in shape with an average size of ~ 50 µm. They appeared to be along the grain boundary of the quartz grains and seemed to interlock these grains. The alternated layers of hematite and quartz with microfolds and faulted features dissecting each other can be clearly viewed in the SEM micrograph. The concentration of iron is more or less uniform in hematite layer. From SEM image, the ore shows a complex sort of interlocking between quartz and hematite. Nirlipta *et al*., 2013 observed that in such type of iron ores the hematite phase is of secondary origin and form a Martite phase due to the oxidation of magnetite.

A well crystalline formation of the three phases i.e. martite, hematite and quartz occur in such ores. However, hematite which occurs as Martite is pseudomorphic magnetite and it retains the shape of an original magnetite. From geological point of view the transformation of one mineral phase to another occurs due to variation in heat, temperature and pressure that causes the homogeneous crystallization and eventually small crystals are formed by re-crystallization in a large number. Bhattacharya *et al*., (2007) during their investigation confirmed that hydrothermal fluids caused the re-crystallization of hematite and due to oxidation magnetite gets converted to hematite and then appeared in the form of martitized product. SEM pattern shows presence of acicular hematite with interstitial spaces

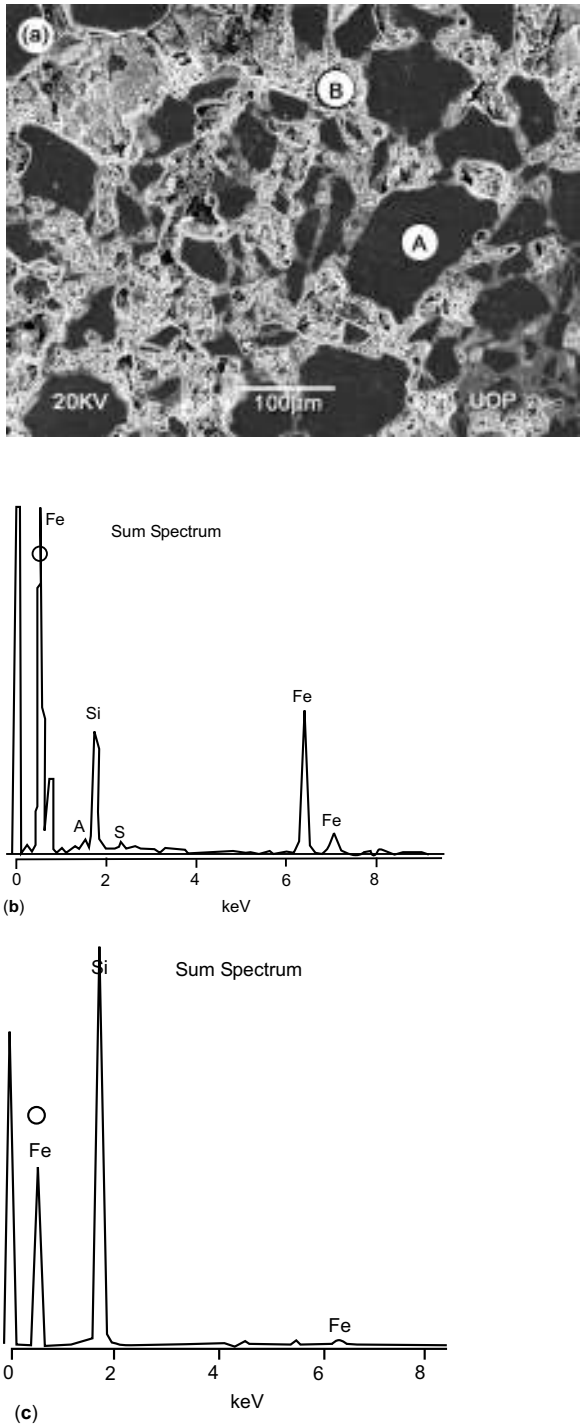

Fig. 3. (a) SEI of the as-mined iron ore sample showing the presence of Quartz with blakish contrast and plan morphology marked as "A" along with Hematite with white contrast and rough granular morphology marked as "B", (**b**) EDS spectra of the marked regions B (**c**) EDS spectrum of the marked region A.

occupied by quartz. EDX analysis shows a high percentage of Si (71 wt.%) and complex interlocking of hematite and silica which made it very difficult for beneficiation. The detailed elemental and relevant oxide composition of the gross and marked micro-regions shown in Fig. 3 is given in Table 2.

EDS analysis showed the presence of high concentration of iron in rough granular micro-regions marked as 'B' and high concentration of silicon in the microregion with black contrast marked as 'A'.

Beneficiation of iron ore *via* shaking table. EDS spectra of the concentrate obtained from shaking table for iron ore at 100 and 200 mesh sizes are shown in Fig. 4 (a, b). The gross elemental and oxide compositions for 100 and 200 meshes are given in Table 3.

Table 2. Elemental and oxide composition of different micro-regions shown in Fig. 3.

Micro-region/ grain	Elemental composition (wt.%)		Oxide composition (wt.%)		
	Fe	Si	O	Fe_2O_3	SiO_2
Gross	23.37	39.64	36.99	28.27	71.73
A	…..	99.99	---	---	100
B	71.12	8.35	20.53	85.06	14.94

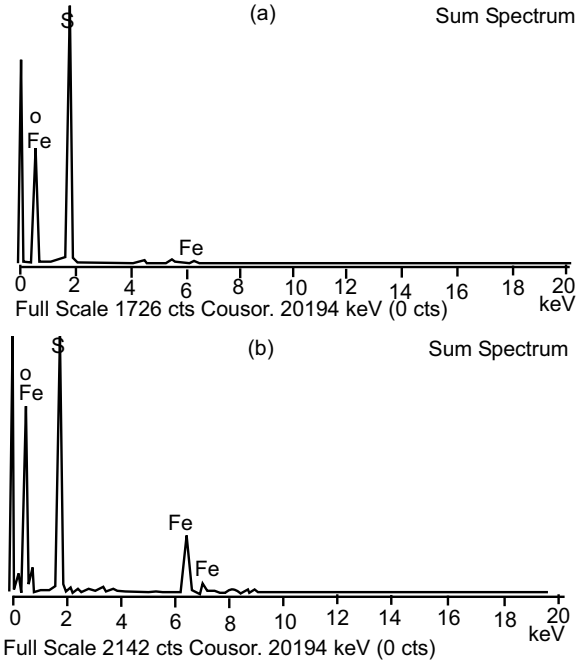

Fig. 4. (a, b): EDS spectra of iron ore after passing via shaking table at 100 and 200 meshes.

EDS study confirmed the concentration of iron in the as-mined ore sample to be 23.37 wt.% and after beneficiation through shaking table at 100 and 200 mesh it was 36.51 and 38.70 wt.% respectively indicating an increase in the concentration after beneficiation. Similarly the content of silica decreased from 39 to 27 wt. %. A comparison of oxide concentration of iron and silica before and after beneficiation is shown in Table 4. Figure 5 shows as increase in concentration of iron and decrease of silica by increasing mesh size from 100 to 200 mesh.

From these results it can be conclude that by reducing particle size of ore the concentration of iron increases and that of silica decreases and more beneficiation will take place. It indicates that minerals begin to separate into iron and silica after 100 mesh particle size due to differences in density. But economically it is not fruitful due to high energy consumption for getting fine particle size. Isnugroho *et.al.* (2011) observed that the process of iron mineral separation from concern gangue will be higher with increasing level of fine particle size. Passing the ore through magnetic separator brings no up-gradation because of non-magnetic nature of hematite

Table 3. Elemental and oxide composition of iron ore concentrate obtained from shaking table at 100 and 200 mesh sizes.

Mesh size	Gross elemental and oxide composition (wt. %)				
	Elements			Oxide	
100	Fe	Si		O	
Fe_2O_3	SiO_2				
	23.50	27.30	49.20	36.51	63.49
200	25.90	25.06	49.04	38.70	61.30

Table 4. Comparison of iron oxide and silica content in the as-mined ore and after beneficiation *via* shaking table at 100 and 200 mesh sizes.

Gross oxide of as-mined iron ore		Oxide composition of iron ore at 100 mesh (149 μm) after beneficiation *via* shaking table		Oxide composition of iron ore at 200 mesh (74 μm) after beneficiation *via* shaking table	
Oxides	wt%	Oxide	wt%	Oxide	w t %
Fe_2O_3	28.26	Fe_2O_3	36.51	Fe_2O_3	38.70
SiO_2	71.73	SiO_2	63.49	SiO_2	61.30

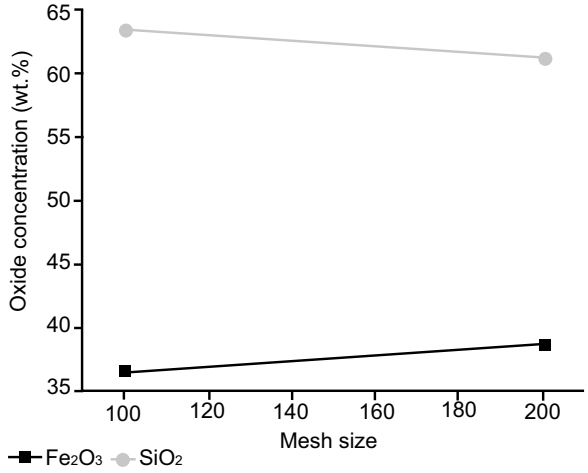

Fig. 5. Variation of the oxide concentration of iron and silica with mesh size, indicating an increase in the iron oxide content and decrease in silica content.

ore. The nonmagnetic iron ore can be changed into a magnetic iron ore through roasting.

Conclusion

In this research work iron ore from Karak, KP, Pakistan was characterized using XRD, SEM and RLM. Karak iron ore is a low grade siliceous iron ore. The major elements detected by EDS in this ore are Iron and silicon. From XRD the presence of iron oxide (Hematite) and silica phases were identified. The up-gradation/ beneficiation of iron ore was performed using shaking table and magnetic separator. Through shaking table the iron ore was up-graded from 28.27 wt.% to 38.70 wt.% at 200 mesh, thus achieving a maximum of 10% upgraded ore. Due to non-magnetic nature of the ore the technique of magnetic separation was proved to be ineffective.

Acknowledgement

The authors acknowledge the financial support of Higher Education Commission (HEC), Pakistan. The authors also acknowledge the financial support of the Khyber Pakhtunkhwa Government through the Pilot Research Studies Program of the Directorate of Science & Technology (DoST), KP for extension in the Mineral Up- gradation Pilot Plant and Up-gradation of Materials Research Laboratory, University of Peshawar, Pakistan.

Conflict of Interest. The authors declare no conflict of interest

References

Abu-zeid, A.M. 1967. A Contribution to the Beneficiation of El-Gedida Iron ore, Bahariya Oases, Egyp, *M.Sc. Thesis*, 60-62pp Faculty of Engineering, Cairo University page.

Ali, M.N.W. 2004. A study on the oolitic iron ore mineralization of wadi halfa, *Arab Mining Conference*, University of Amman, Jorden.

Ali, M. N.W., Babiker, M.E., Eltayeb, H., Haroun, A. 2003. A study on the oolitic iron ore mineralization of wadi halfa, Arab Mini Conference *Geolocal Research Authority of Sudan*.

Bhattacharya, H.N., Chakraborty, I. Ghosh, K.K. 2007. Geochemistry of some banded iron formations of the Archean supracrustals, Jharkhand-Orissa region, India. *Journal of Earth Systems Science*, **116:** 3, 245-259.

Burt. R. 1999. The role of gravity concentration in modern processing plants, *Minerals Engineering* **12:** 1291-1300.

Fatma, H.A., Arafa, M.A. 1999. Concentrate from an egyptian baritic iron ore. *Proceedings of the 6th International Conference on Mining, Petroleum, and Metallurgy*, Faculty of Engineering, Cairo University, 1999.

Faraghaly, M.G. 2002. Beneficiation of el-gedida barite iron ore, *Journal of Engineering Science*, **30:** 779-812.

Gaudin, A.M. 1987. *Principles of Mineral Dressing*, Tata Mcgraw-Hill Publishing Company Limited, Mohan Makhijani at Rekha Printers pvt. ltd, New Delhi, India.

Guney, A. 2000. The beneficiation of camdag iron ore, ITU, Mining Eng. Dep. Min and Coal processing Section, 80626, Maslak, Istanbul, Turkey.

Isnugroho, K., Birawidha, D.C. 2011. Beneficiation of low grade iron ore with manganese content as raw material for ferro. *Mineral Processing Division* – Indonesian Institute of Science (LIPI),

Kazmi, A.H., Abbas, S.G. 2001. *Metallogeny and Mineral Deposits of Pakistan*. pp. 47-58 Graphic Pulisher, Karachi.

Mansar, R.J., Barley, R.W., Wills, B.A. 1991. The shaking table concentrator the influence of operating conditions and table parameters on mineral separation the development of a mathematical model for normal operating conditions, *Minerals Engineering*, **4:** 369-381.

Miaha, P.P., Mohapatara, B.K., Mahanta, K. 2009. Upgradation of low grade siliceous manganese ore from Bonai-Keonjhar belt, Orrisa, India*, Journal of Minerals and Materials Characterization and Engineering*, **8:** 47-56.

Mukherjee, A.K., Bhattacharjee, D., Mishra, B.K. 2006. Role of water velocity for efficient jigging of iron ore, *Minerals Engineering*, **19:** 952-959.

Nirlipta. P.N. 2013. Mineralogical constraints in beneficiation of low grade iron ores of barsua, eastern India, *International Journal of Engineering and Innovative Technology (IJEIT)* **3:** 109.

Roy, S. 2009. Recovery improvement of fine iron ore particles by multigravity separation. *The Open Mineral Processing Journal*, **2:** 17-30.

Rowayshed, S.A. 1983. "Beneficiation of El-bahariya Oasis Low Grade Iron Ores", *M.Sc. Thesis*, Faculty of Engineering, Al-azhar University, Cairo, 103.

Samykina, E., Surkov, A., Eppelbaum, L., Semenov, S. 2005. Do old spoils contain large amounts of economic minerals? *Minerals Engineering*, **18:** 643-645.

Shah, M.T., Moon, C.J. 2004. Mineralogy, geochemistry and genesis of the ferromanganese ores from Hazara area, NW Himalayas, northern Pakistan. *Journal of Asian Earth Sciences*, **23:** 1-15.

Shivamohan, R., Forssberg, E. 1985. Principles of tabling, *International Journal of Mineral Processing*, **15:** 281-295.

Siddiqui, R.H., Naghma, H.S., Ghazanfar, A. Kakepoto, A.A. 2000. Mineralogy and gensis of dilbnad iron ore Balochistan, Pakistan, Geolgica, Geoscience Laboratory'. *Geologica, Islamabad Pakistan*, Islamabad Pakistan, vol. **5:** 67-97.

Svoboda, J., Ross, V.E. 1989. Particle capture in the matrix of magnetic separator, *International Journal of Mineral Processing*, **27:** 75-94.

Svoboda, J. 1994. The effect of magnetic field strength on the efficiency of magnetic separation, *Mineral Engineering*, **7:** 747-757.

Pak. j. sci. ind. res. Ser. A: phys. sci. 2021 **64A**(1) 26-34

Characterization of Cleaning Potential of Khokhar-Bala, Punjab (Pakistan) Coal and Simulation-Based Study for Identification of Best Strategy for its Cleaning

Muhammad Shahzad*, Syed Mahmood Arshad, Zulfiqar Ali, Rana Ahmad Ali and Hamza Shabeer
Mining Engineering Department, University of Engineering and Technology, Lahore, Pakistan

(received September 4, 2019; revised January 6, 2020; accepted January 27, 2020)

Abstract. This study involves the characterization of Khokhar-Bala coal of Punjab (Pakistan) coal field to establish its particle distribution data for size, density and floatability through sizing, float-sink tests and release analysis. Khokhar Bala coal contains high amounts of unwanted impurities like ash (35.22%) and sulphur (8.38%). Over 93% of its mass consists of +1.00 mm particles, when run-of-mine coal is crushed to 38 mm. Washability curves, degrees of washing and the S-values show that the coarser fractions (–38+25 mm; –25+13.33 mm; –13.33+3.35 mm) are extremely difficult to clean, whereas the cleaning potential is high for size fractions –3.35+1.00 mm (moderately difficult) and –1.00+0.15 mm (relatively easy). Modelling and simulation of several processing configurations indicate that at 16% target ash content, dense medium cyclone treating 38 × 1 mm coal particles will provide the maximum clean yield of 37.39% with sulphur content of 4.80%.

Keywords: characterization, Punjab coal, washability, float-sink, release analysis, simulation

Introduction

Coal is a complex heterogeneous mixture of organic and inorganic constituents (Shahzad *et al*., 2016; Ural, 2007), which is primarily used in electricity generation, cement manufacturing and steel making. The other important uses of coal include coal-derived fuels and chemicals (Osborne and Gupta, 2013). The inorganic constituents, also called mineral matter are the non-combustible materials such as shale, clay, pyrite, quartz, carbonate, etc. These materials are unwanted impurities that act as diluent which result in reduced heating value and increase transportation cost of unit coal mass (Ali, 2012; Ward, 2002). These impurities also affect the suitability of coal for its use in formation of coke, synthetic fuels and petrochemicals described by Ali (2012). Moreover, coals containing sulphur and sulphur-bearing minerals like pyrite produce sulphur dioxide during the burning of coal which cause harmful impacts on the environment and human health (Oteyaka *et al*., 2008).

To overcome the problems caused by the non-combustible mineral matter in coal, it is generally required to reduce the amount of these materials to the limits dictated by end-user by employing coal preparation techniques. When designing a coal preparation plant, generation of extensive laboratory data related to coal characteristics is usually required. This generally involves the determination of mineral matter distribution and washability characteristics of coal at various size levels. After generation of such data, modelling and simulation work is usually performed to find the most appropriate processing circuit that provides maximum yield at the target impurity level.

Various simulation programs are available to design and optimize coal processing circuits including MODSIM (King, 1999), CPDES (Yaqun *et al*., 2002), SUI-SIM (Huang *et al*., 2008), and LIMN (Noble *et al*., 2014; Bergh *et al*., 2013; Hand and Wiseman, 2008) *etc*. LIMN is a spread sheet-based flowsheet simulation software package which has significantly contributed in the coal preparation industry especially in south Africa and Australia due to its ability to readily handle particulate solid flow and separation calculations. The advanced features in LIMN can be used for circuit optimization, equipment selection, evaluation of operational configurations, modelling of complicated processing circuits and to produce simulations for plant design and performance evaluations (Noble *et al*., 2014).

Punjab province of Pakistan possesses the *in-situ* coal resources of 588 million tons (Scott *et al*., 2013). These

*Author for correspondence;
E-mail: m.shahzad87@uet.edu.pk

resources are found in two coal horizons in the upper Indus Basin (salt range) and the Surghar range; extending from Joggi Tilla (Jhelum) to Makerwal covering more than 250 km (Fig. 1) (Shah, 2009). Punjab coal is characterized by high amounts of ash-forming and sulphur bearing minerals which restrict its consumption to brick making industry only (Shahzad *et al*., 2014) whereas, high quality coal is imported to fulfill the energy needs of power, cement and other industries of Punjab. To utilize indigenous coal resources in these industries, it is essential to upgrade their quality by reducing the amount of ash-forming and sulphur-bearing minerals to an acceptable level.

Previously, some studies were performed to establish washability characteristics and flotation response of Punjab coal, and to evaluate its cleaning potential by gravity separation and froth flotation techniques (Shahzad and Ali, 2019; Shahzad and Ali, 2018a; Shahzad *et al*., 2017; 2015) but no systematic study was conducted to design a coal processing circuit. At present, there is not a single State-of-the-art coal preparation plant in operation in Punjab province to improve the quality of indigenous coal to make it suitable for cement and power industries of the province which limit coal ash and sulphur at 16.0% and 1.0%, respectively. This research work was conducted with intention to address this deficiency. The basic objective of this research work is to characterise the coal in a systematic manner for establishing its particle distributions for size, density and floatability. The main aim is to evaluate different processing options by running simulations using limn software to identify the best processing strategy.

Materials and Methods

Gross coal sample amounting over 345 Kg was collected from the stockpiles of Geo-Mineral Associates coal mines located near Khokhar Bala village in Dalwal zone of salt range coalfield of Punjab in accordance to ASTM standards (ASTM D-6883 and ASTM D-2234) and the method described elsewhere (Shahzad *et al*., 2016). Gross coal sample was crushed by using Blake type jaw crusher set at 25 – 38 mm. The crushed product was thoroughly mixed and divided into four parts. One part was prepared following ASTM D-2013 to obtain an analytical sample for proximate analysis and determination of forms of sulfur. The proximate properties were measured as per ASTM D-3172, -3173, -3174, and -3175, whereas ASTM D-2492 were followed for the determination of forms of sulphur.

The other three parts were combined and sieved at 25.00, 13.33, 3.35, 1.00, and 0.15 mm aperture sizes. The resultant fractions were divided separately into two halves; one half of each fraction was prepared to determine its ash and sulphur contents whereas, the other halves were separately subjected to float-sink tests except that of –0.25 mm which was used to perform Dell release analysis. Total 10 dense mediums having specific gravities of 1.30, 1.35, 1.40, 1.45, 1.50, 1.55, 1.60, 1.65, 1.70 and 1.80 were utilised for each float-sink test. Organic liquids (petroleum spirit, carbon tetra chloride, bromo form) were used to prepare heavy mediums for 1.00 × 0.25 mm size fraction, while, aqueous solution of zinc chloride was used for the remaining fractions. In Dell release analysis, kerosene

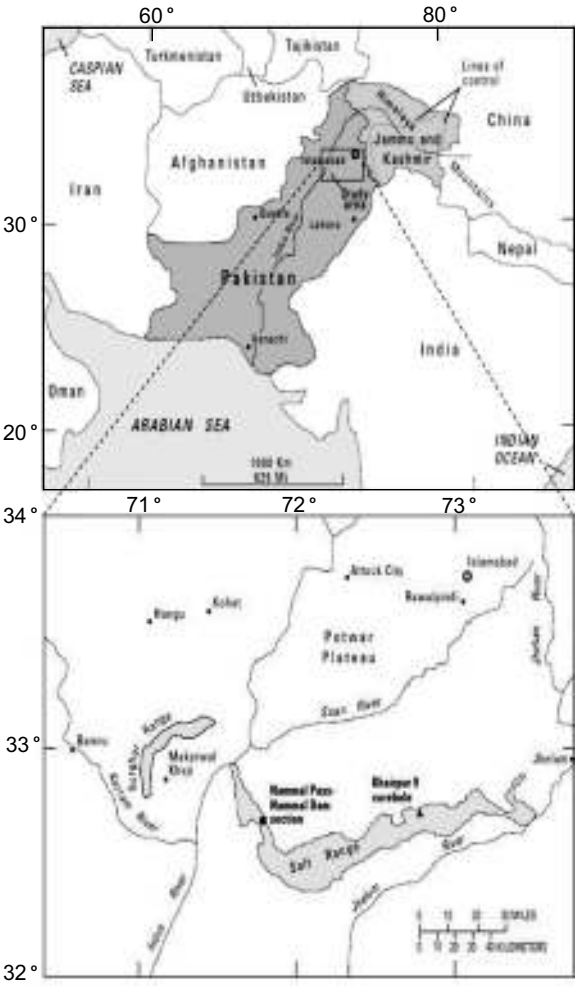

Fig. 1. The coal horizons of Punjab coalfield; salt range and Surghar range (Bybell and Self-Trail, 2007).

oil and methyl iso-butyl carbinol (MIBC) were used as collector and frother in the range of 400 g/t and 100 g/t respectively. The mixing and conditioning time was kept at five minutes each. The solid percentage and impeller speed were maintained at 15% and 1300 rpm respectively whereas, pH was kept natural. The fractions obtained from float-sink and release tests were analysed for ash and sulfur as per ASTM D-3174 and ASTM D-3177, respectively.

Results and Discussion

Proximate and sieve analysis. Proximate analysis performed on raw coal revealed that Khokhar Bala coal contained low inherent moisture (2.20%), high ash (35.22%), high volatile matter (33.70%) and low fixed carbon (28.87%). It contained very high amount of total sulphur of 8.38%. Total sulphur comprised of 0.89% organic, 6.34% pyritic and 1.15% sulphate components. The results of sieve analysis and proximate properties of each size fraction are presented in Fig. 2. The sizing analysis showed that coarse fraction (+25 mm) constituted nearly half of the total feed mass whereas, over 93% of coal consisted of +1.00 mm particles. Typically, 38 × 1 mm coal particles are cleaned by either dense medium cyclones or jigs throughout the world.

The proximate properties of various size fractions revealed that ash contents, in general, increased with decreasing particle size. This trend may be due to the presence of ash forming minerals in the form of amalgamates of fine particles and the nodules of variable sizes. Crushing broke the cementing forces which trickled down these fine particles and nodules to finer size fractions (Shahzad *et al*., 2016). The total sulphur content remained nearly the same (8.29–8.75%) for +1.00 mm size fractions whereas, finer fractions exhibited relatively lower sulphur values ranging between 5.59% and 5.99%. This behaviour may be associated with high amounts of pyrite present in Punjab coal. Pyrite is relatively hard and does not break easily into fine particles by crushing forces, resulting in its higher amounts in the coarser fractions. Since the ultrafine fraction (–0.15 mm) constituted a minute proportion (1.55%) of feed coal with the highest amount of ash content (51.74%). It can be discarded directly into tailings without processing.

Washability analysis. The washability curves plotted from the float-sink data of –38+25 mm, –25+13.33 mm, –13.33+3.35 mm, –3.35+1.00 mm and –1.00+0.15 mm are presented in Fig. 3-7, respectively. The washability curves predict the theoretical yield of clean coal along with operating specific gravity of separation and the amount of near-gravity material at the specified ash/sulphur content. In addition, these curves also predict the yield and quality of tailings/waste product at the same specific gravity of separation (Gupta and Yan, 2006). At 16% limit ash content, the yield and sulphur contents of clean coal, specific gravity of operation,

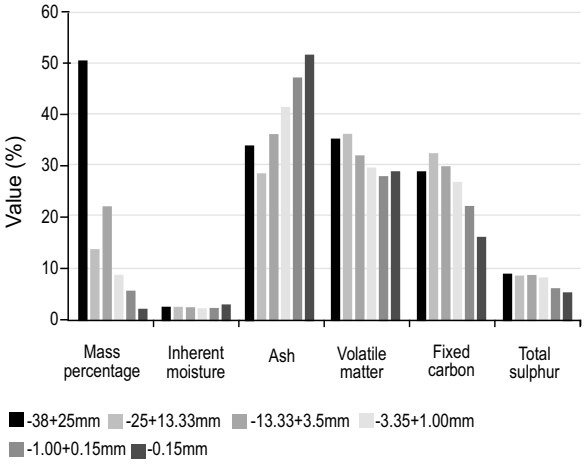

Fig. 2. Sizing characteristics of Khokhar Bala, Punjab coal.

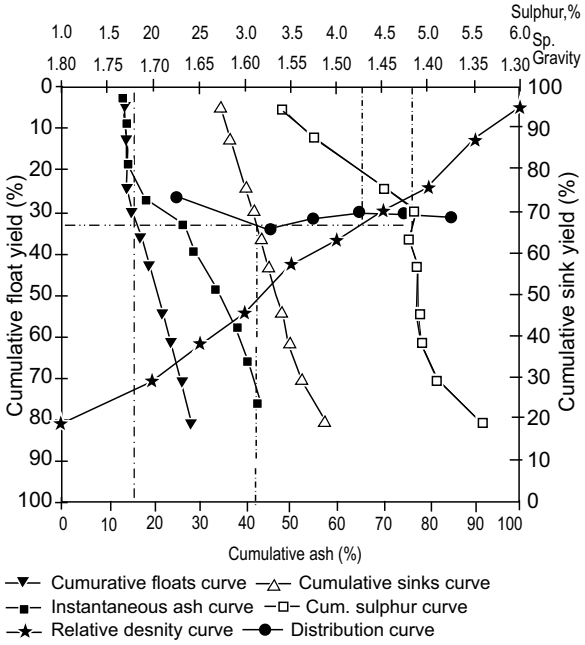

Fig. 3. Washability characteristic curves of size fraction 38 × 25 mm.

amount of near gravity material and yield and quality of tailings product are presented in Table 1 along with the feed ash and sulfur contents for the above-mentioned size fractions of Khokhar-Bala, Punjab coal.

At 16% target ash, the size fractions –38+25 mm and –25+13.33 mm gave the minimum and maximum yields of clean coal, respectively. The maximum yield of –25+13.33 mm size fraction could be due to its minimum

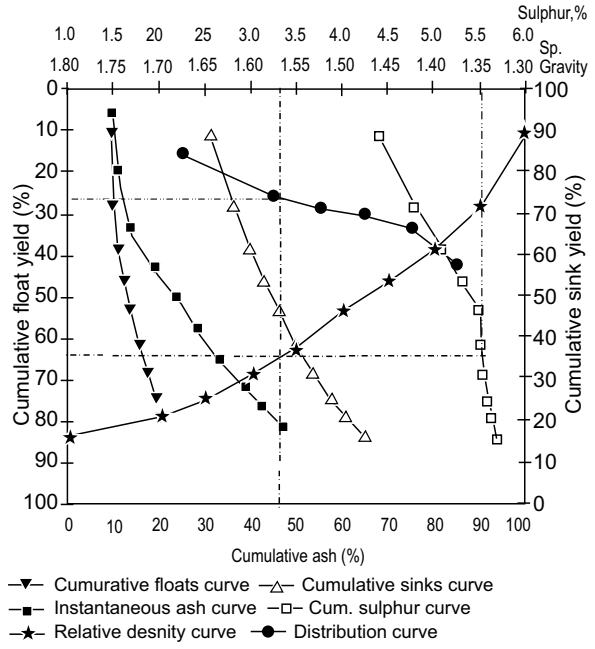

Fig. 4. Washability characteristic curves of size fraction 25 × 13 mm.

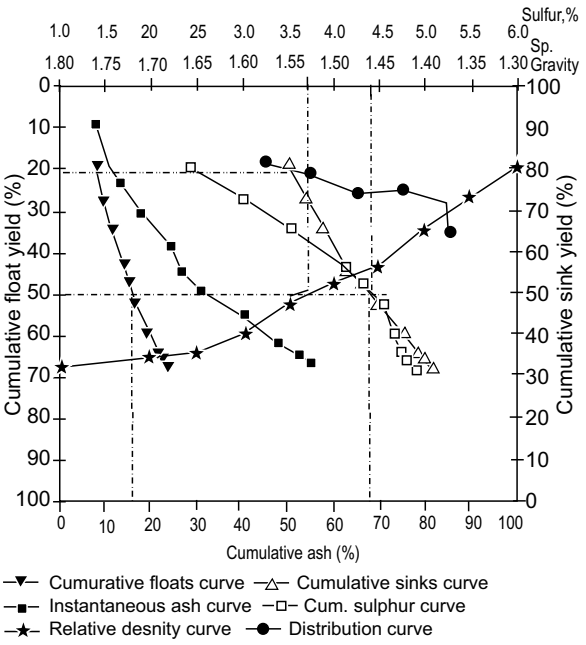

Fig. 6. Washability characteristic curves of size fraction 3.35 × 1.00 mm.

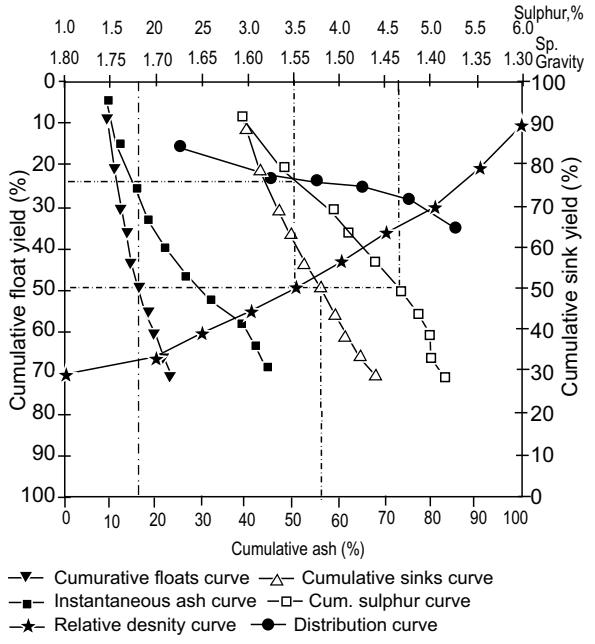

Fig. 5. Washability characteristic curves of size fraction 13 × 3.35 mm.

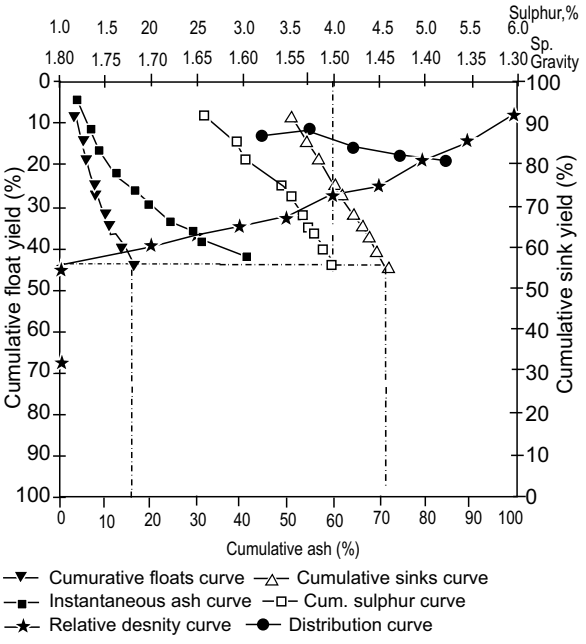

Fig. 7. Washability characteristic curves of size fraction 1.00 × 0.15 mm.

feed ash content and relatively better liberation of coal particles whereas the minimum yield of –38+25 mm may be attributed to the poor liberation of ash-forming minerals in the coarser particles. The clean coal yield remained in the range of 43 – 49% for the remaining finer size fractions despite increasing feed ash content with decreasing particle size. This indicates that liberation of ash-forming minerals improves with decreasing particle size, especially below 25 mm.

On the other hand, sulphur bearing minerals exhibited different behaviour as indicated by the amount of clean coal sulphur at 16% ash content (Table 1). The coarsest and the finest fractions provided the minimum reduction of sulphur (≈ 33%) whereas, the sulphfur reduction values (≈ 43 – 47%) were higher for the middle fractions. The lower reduction in the coarsest fraction may be attributed to the less liberation of sulphur-bearing minerals whereas, the presence of sulphur-bearing minerals within coal matrix in the form of finely disseminated particles may be the cause of lower reduction in the finest size fraction.

Conventionally, the ease of coal washing is indicated by the shape of instantaneous ash curve also called primary washability curve. More it close to the shape of letter L, easier it will be to wash the coal (Shahzad *et al*., 2015; Lin *et al*., 1999; Meyers *et al*., 1992). The shape of primary washability curves for all size fractions of Khokhar-Bala coal was found nearly identical and far away from the shape of letter L. However, the fractions finer than 3.35 mm size produced relatively better primary washability curves, indicating enhanced washability characteristics of finer coal particles.

Another method to describe the ease or difficulty of coal cleaning is by percentages of near gravity material (±0.1 SG) at the required specific gravity (Bird, 1931). The percentage of near gravity materials at various specific gravities of separation is typically represented by the distribution curve. The more the percentage of near-gravity material, the more difficult will be to clean the coal (Gupta and Yan, 2006). It was found that the amount of near-gravity material was decreased with decreasing particle size showing better washing characteristics of finer size fractions.

Recently, a simple method to quantify the degree of coal washing was proposed by Shahzad and Ali (2018b). They introduced a simple mathematical equation for estimating the degree of coal washing in percentage at various specific gravities of separation. The higher the degree of coal washing, the easier will be to clean the coal. They also proposed an index, termed as S-value to represent the washability characteristics of coal by a single number, the value of which ranges between 0 and 100. The equations for degree of washing and S-value proposed by them are reproduced here:

$$DWi = \tan\left(\tan^{-1}\left[\frac{Y_i}{R_i}\right] - 45\right) \quad \text{..... 1}$$

$$\text{S-value} = \sqrt[4]{DW_{1.3} \times DW_{1.4} \times DW_{1.6} \times DW_{1.8}} \quad \text{..... 2}$$

where:

DWi, Yi and Ri represent the degree of washing, cumulative float yield and cumulative ash recovery at 'i' specific gravity respectively. $DW_{1.3}$, $DW_{1.4}$, $DW_{1.6}$ and $DW_{1.8}$ are the degrees of washing at specific gravities of 1.3, 1.4, 1.6 and 1.8, respectively in percentages. They also proposed a classification system based on S-value to determine the extent of coal cleaning. The degrees of washing and S-values were calculated for all size fractions of Khokhar-Bala coal which are provided in Table 2.

The degrees of washing were found higher at lower specific gravities of separation for all size fractions

Table 1. Washability characteristics of various size fractions of Khokhar-Bala, Punjab coal at 16% target ash content of clean coal

Size fraction	Feed coal		Clean coal		Tailings product			Specific gravity of separation	Near gravity material (%)
	Ash	Sulphur	Yield	Sulphur (%)	Yield	Ash	Sulphur		
–38+25	33.78	8.57	33.07	4.82	66.93	42.55	10.43	1.47	30.30
–25+13.33	28.62	8.29	63.79	5.52	36.21	50.93	13.22	1.57	27.82
–13.33+3.35	36.00	8.75	48.78	4.62	51.22	55.09	12.69	1.55	24.40
–3.35+1.00	42.04	8.38	49.49	4.59	50.51	67.61	12.28	1.53	23.66
–1.00+0.15	47.35	5.99	43.42	4.00	56.58	71.41	7.52	1.80	7.76

Table 2. Degree of washing and S-values for various size fractions of Khokhar-Bala coal

Specific gravity	– 38+25 mm	–25+13.33 mm	–13.33+3.35 mm	–3.35+1.00 mm	–1.00+0.15 mm
1.30	42.83	51.35	58.04	69.74	83.48
1.35	41.57	49.18	53.27	62.08	79.27
1.40	40.78	45.50	48.88	56.92	76.53
1.45	38.51	41.18	45.93	49.43	71.34
1.50	32.77	35.97	41.89	46.53	69.17
1.55	28.15	29.93	37.98	42.85	63.84
1.60	21.16	24.95	33.67	35.76	60.99
1.65	17.08	20.20	29.44	31.73	58.17
1.70	12.91	17.27	25.42	30.51	54.47
1.80	9.01	13.56	22.25	28.31	48.07
S-Value	24.02	29.82	38.18	45.37	65.79
Cleaning extent	Extremely difficult	Difficult	Difficult	Moderately difficult	Relatively easy
Coal class	F	D	D	C	A

indicating higher cleaning extent at lower specific gravities of separation. The values of degree of washing increased with decreasing particle size, thus indicating improved washability characteristics of Khokhar-Bala coal with decreasing particle size. The same trend was also found for the S-value. The coal class and the cleaning extent were also determined for all size fractions based on S-value and the proposed classification. It was found that the coarsest size fraction was extremely difficult to clean and the middle fractions belonged to difficult to moderately difficult class of coal cleaning. The finest fraction was found to be relatively easy to clean.

Release analysis. The flotation response of ultrafine fraction (-0.15 mm) measured by release analysis is presented in Fig. 8 in the form of yield-ash and yield-sulphur curves. These curves specified that ultrafine fraction of Khokhar-Bala coal would be difficult to clean by froth flotation. It would be extremely difficult to produce clean coal having ash content below 16% ash limit. At 40% yield, a clean coal with ash content of 21.24% and sulphur content of 4.53% was obtained from a feed coal having ash and sulphur contents of 51.74% and 5.59%, respectively. The yield-sulphur curve showed very low reduction in sulphur contents. This behaviour may be attributed to the high floatability of pyrite. Since, the ultrafine size fraction constitutes only 1.55% of the total coal mass and the cost of treating ultrafine coal by froth flotation is always higher, it will be the best to discard this size fraction directly into the waste/tailings product during coal preparation.

Modelling and simulation of processing circuits. Modern coal preparation plants typically involve four separate parallel processing circuits for treating coarse (+50 mm), small (50 × 1 mm), fine (1 × 0.15 mm) and ultrafine (-0.15 mm) coal (Luttrell *et al*., 2014). Dense medium baths, dense medium cyclones, and jigs are the most common choices for treating coarse coal. Nowadays, almost all the small coal is treated in the dense medium cyclones. Spirals, shaking tables, fluidized-bed separators and water-only cyclones are the available technologies for cleaning fine coal, while froth flotation is the only technique to clean ultrafine coal at the commercial level (Osborne, 2013).

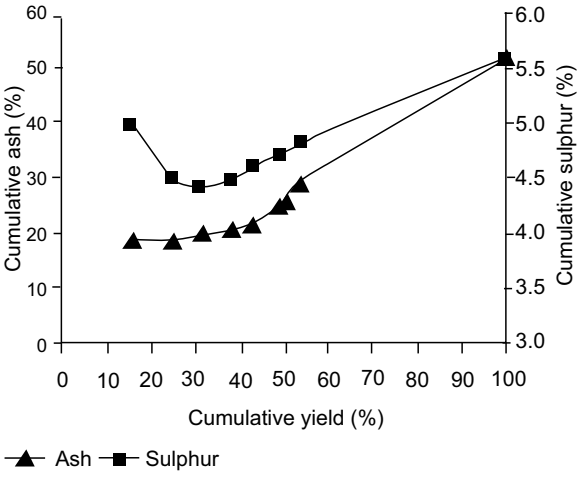

Fig. 8. Floatability response of size fraction –0.15 mm.

LIMN was used to model and simulate several types of coal processing circuits to generate simulated data for predicting clean coal yield, ash and sulphur. Since washability characteristics of Khokhar Bala coal dictated that it contained high percentage of near-gravity material, the water-based techniques would be less efficient. For coals containing higher amounts of near-gravity materials, dense medium separators are considered the best choice for their cleaning (Sripriya *et al*., 2007). Thus, three circuits based on dense medium separators along with one circuit based on water-based separators were modelled and simulated to generate clean coal data at specific gravity of separation ranging from 1.30 to 1.80. These circuits are described in Fig. 9-10. The simulated data generated for clean coal yield, ash and

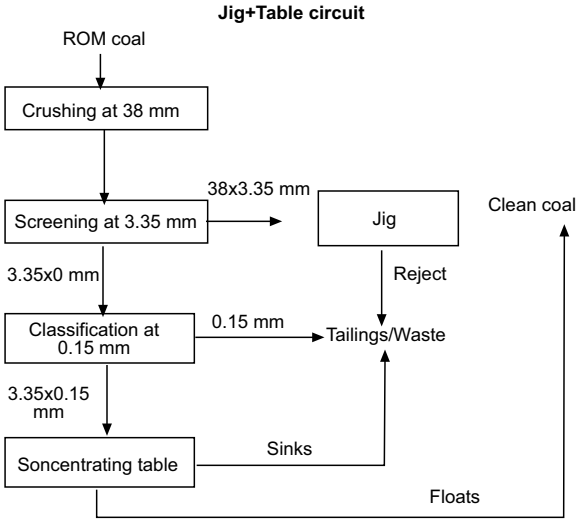

Fig. 10. Circuit consisting of water-based separators involving jig and concentrating Table.

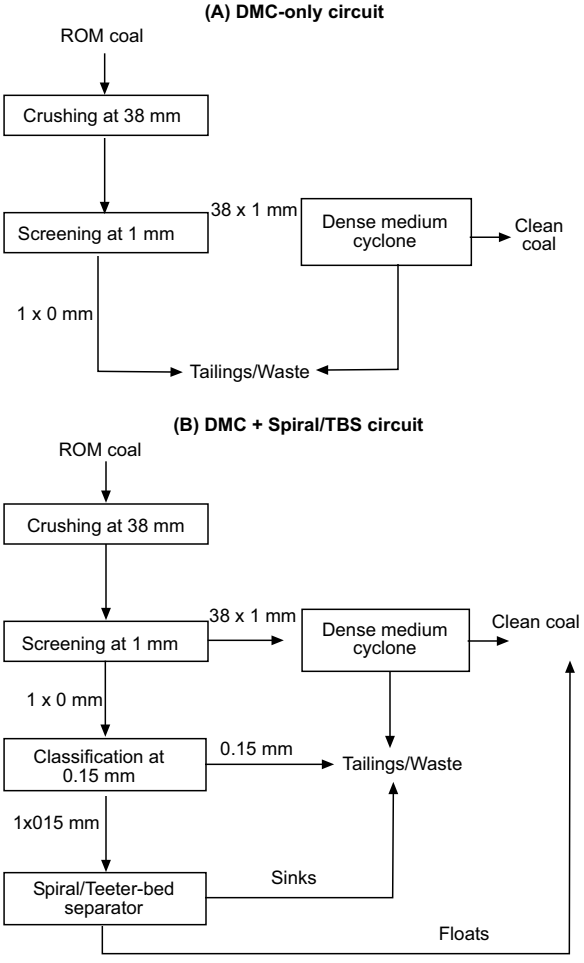

Fig. 9. Dense-medium based circuits: **(A)** Dense-medium cyclone (DMC) only circuit, **(B)** Circuit consisting of dense medium cyclone and spiral separators.

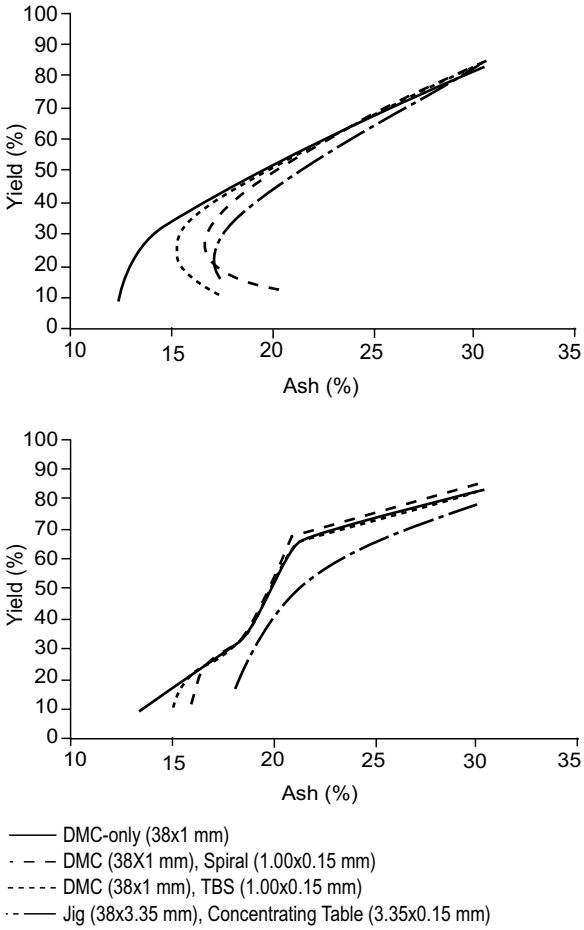

Fig. 11. Simulated yield-ash and yield-sulphur curves for the three circuits.

sulphur for these circuits were plotted and are portrayed in Fig. 11.

Figure 11 shows that DMC-only circuit provides the highest yield with lower amounts of ash and sulphur in the clean coal at target ash content below 20%, whereas above 20% ash, the circuit consisting of DMC and TBS is the better choice. At 16% limit ash, the maximum clean coal yield of 37.39% with sulphur content of 4.80% is achievable through coal preparation. To meet the sulphur limit of 1.0%, blending of clean coal with low sulphur imported coal would be required.

Above 20% target ash content, the difference between the predicted yields provided by dense-medium and water-based circuits becomes less than 5% which further decreases at higher values of target ash. Since, the capital and operating costs of water-based circuits is less than dense medium circuits, the economics may favour water-based circuit over dense medium circuits above 20% target ash content. Therefore, the economic analysis would be required before choosing the best circuit for cleaning Khokhar Bala coal.

Conclusion

Particle distribution data for size, density and floatability was established for Khokhar-Bala, Punjab coal. More than 93% of Khokhar-Bala coal is constituted by +1.00 mm particles. Overall, Khokhar-Bala coal is difficult to wash. The washing characteristics improve with decreasing particle size. The ultrafine fraction of Khokhar Bala coal exhibits poor flotation response. The 16% ash limit required by cement industry of Punjab can be achieved with reasonable clean coal yield. However, the sulphur contents could not be reduced below 1.0% limit. The dense-medium cyclone treating +1.00 mm coal particles will be the most suitable choice for treating Khokhar-Bala coal below target ash content of 20%. Above 20% ash, the combination of dense medium cyclone and teeter-bed separator will be a better option.

Conflict of Interest. The authors declare no conflict of interest.

References

Ali, Z. 2012. *Identification of Improved Strategies for Processing Fine Coal*, *Bulletin 2078-B*, Virginia Polytechnic Institute and State University, Virginia, USA.

Bergh, J.P., Falcon, R.M.S., Falcon, L.M., 2013. Techno-economic impact of optimized low-grade thermal coal export production through beneficiation modelling. *The Journal of South African Institute of Mining and Metallurgy*, **113:** 817-824.

Bird, B.M. 1931. Interpretation of float-and-sink data, *3rd International Conference on Bituminous Coal*. Carnegie Institute of Technology, Pittsburgh, USA, 722 pp.

Bybell, L.M., Self-Trail, J.M. 2007. *Calcareous Nannofossils from Paleogene Deposits in the Salt Range*, Punjab, Northern Pakistan.

Gupta, A., Yan, D.S., 2006. *Mineral Processing Design and Operation*. eBookISBN:9780444516367, Elsevier, The Netherlands.

Hand, P.E., Wiseman, D.M. 2008. Combined coal and medium circuit simulation for design and optimisation. In: *12th Australian Coal Preparation Conference and Exhibition*, Mathewson, D. J. (editor), Darling Harbour, New South Wales, Australia.

Huang, Z., Mohanty, M., Sevim, H., Mahajan, A., Arnold, B. 2008. Techno-economic analysis of coal preparation plant design using siu-sim simulator. *International Journal of Coal Preparation and Utilization*, **28:** 15-32.

King, R.P. 1999. Practical optimization strategies for coal-washing plants. *Coal Preparation*, **20:** 13-34.

Lin, C.L., Parga, J.R., Drelich, J., Miller, J.D. 1999. Characterization of washability of some Mexican coals. *Coal Preparation*, **20:** 227-245.

Luttrell, G.H., Bethell, P., Honaker, R.Q. 2014. Designing and operating fine coal processing circuits to meet market specifications. *International Journal of Coal Preparation and Utilization*, **34:** 172-183.

Meyers, R.A., Laskowski, J.S., Walters, A.D. 1992. Coal preparation. In: *Encyclopedia of Physical Science and Technology*, Meyers, R. A. (editor), Academic Press, Inc., San Diego, pp. 409-435.

Noble, A., Bratton, R., Luttrell, G.H., Wiseman, D. 2014. Solving process engineering and flowsheet design challenges with limn, *Annual Meeting & Exhibition*. Society for Mining, Metallurgy and Exploration, pp. 352-358, Salt Lake City, Utah, USA.

Osborne, D. 2013. *The Coal Handbook Toward Cleaner Production*, vol. **1,** edition 1, Woodhead Pubishing Limited, Philadelphia, USA.

Osborne, D.G., Gupta, S.K. 2013. 1-Industrial uses of coal. In: *The Coal Handbook: Towards Cleaner*

Production. D. Osborne (editor), pp. 3-30, Woodhead Publishing.

Oteyaka, B., Yamik, A., Ucar, A., Sahbaz, O., Demir, U. 2008. The washability of lignites for clay removal. *Energy Sources, Part A: Recovery, Utilization and Environmental Effects*, **30:** 797-808.

Scott, M., Radonich, A., Gort, S., Smallwood, C., Ryan, N., Garsteling, M. 2013. *Coal Resources of the Salt Range and Trans Indus Range*, Punjab. Mines and Mineral Department. Government of Punjab, Pakistan.

Shah, S.M.I. 2009. *Stratigraphy of Pakistan*. Geological Survey of Pakistan, *Ministry of Petroleum and Natural Resources*, vol. **22,** Government of Pakistan.

Shahzad, M., Ali, Z., 2018a. Cleaning of Dalwal-Punjab coal by using shaking table. *Pakistan Journal of Scientific and Industrial Research*, Series A: Physical Sciences, **61A:** 56-58.

Shahzad, M., Ali, Z. 2018b. Development of simple techniques for determining the extent of coal cleaning-part 2: Estimating coal washability characteristics and separator performance. *International Journal of Coal Preparation and Utilization*, 1-14.

Shahzad, M., Ali, Z. 2019. A simple and efficient process for small-scale cleaning of poorly liberated, difficult-to-wash low-rank coal. *Energy Sources, Part A: Recovery, Utilization, and Environmental Effects*, 1-14.

Shahzad, M., Ali, Z., Majeed, Y., Emad, Z., Aaqib, M., Adeel, B. 2016. Liberation studies of Padhrar coal by using fractionation method, XRD analysis and megascopic and microscopic techniques. *Pakistan Journal of Scientific and Industrial Research*, Series A: Physical Sciences, **59:** 90-95.

Shahzad, M., Ali, Z., Siddique, A. 2017. Cleaning of Dulmial-Punjab coal by froth flotation. *Pakistan Journal of Scientific and Industrial Research*. Series A: Physical Sciences, **60:** 169-171.

Shahzad, M., Iqbal, M.M., Hassan, S.A., Saqib, S., Waqas, M. 2014. An assessment of chemical properties and hardgrove grindability index of Punjab coal. *Pakistan Journal of Scientific and Industrial Research*, Series A: Physical Sciences, **57:** 139-144.

Shahzad, M., Tariq, S.M., Iqbal, M.M., Arshad, S.M., Saqib, S. 2015. An assessment of cleaning amenability of salt range coal through physical cleaning methods. *Pakistan Journal of Scientific and Industrial Research*, Series A: Physical Sciences, **58:** 74-78.

Sripriya, R., Banerjee, P.K., Soni, Baijal, A.D., Dutta, A., Rao, M.V.S., Chatterjee, S. 2007. Dense-medium cyclone: plant experience with high near-gravity material Indian coals. *Coal Preparation*, **27:** 78-106.

Ural, S. 2007. Quantification of crystalline (mineral) matter in some Turkish coals using interactive rietveld-based X-ray diffractometry. *International Journal of Coal Geology*, **71:** 176-184.

Ward, C.R. 2002. Analysis and significance of mineral matter in coal seams. *International Journal of Coal Geology*, **50:** 135-168.

Yaqun, H., Shan, L., Maixi, L., Yali, K., Huaiyu, L. 2002. A profit-oriented expert system for coal washery optimization. *Coal Preparation*, **22:** 93-107.

Pak. j. sci. ind. res. Ser. A: phys. sci. 2021 **64A**(1) 35-45

Assessing Impact of Naphthalene Acetic Acid on the Growth and Yield of Okra (*Abelmoschus esculentus* (L.) Moench)

Muhammad Nisar[a], Habib Ur Rahman[a], Muhammad Sohail Khan[a]*, Ilham Khan[b], Saba Fatima[a], Kashif Waseem[a] and Khalid Rahman[a]

[a]Department of Horticulture, Faculty of Agriculture, Gomal University, Dera Ismail Khan, Khyber Pakhtunkhwa, Pakistan

[b]Institute of Chemical Sciences, Gomal University, Dera Ismail Khan, Khyber Pakhtunkhwa, Pakistan

(received June 11, 2019; revised January 23, 2020; accepted February 3, 2020)

Abstract. This study assessed the impact of naphthalene acetic Acid (NAA) on the growth and yield of Okra cv. Sabz Pari at Agricultural Research Institute, Dera Ismail Khan, Khyber Pakhtunkhwa, Pakistan. A field experiment was set out in randomised complete block design with NAA application as a main factor. Different NAA concentrations were obtained by dissolving NAA in distilled water at the rate of 0 (control), 10, 30, 50, 70, 90 and 110 mg/L. NAA treatments along with control were foliar applied to okra plants after 30 days of sowing. Lower concentration of NAA (30-50 mg/L) stimulated maximum increase in plant height (59.5-57.2%), number of leaves/plant (50.4-45.5%,), total plant leaf area (113.9-119.4%), internodes/plant (72.5-61.6%), internode length (53.2-44.5%), pod diameter (53.5-49.9%), pod fresh weight (126.8-111.8%), pod yield (271.2-255.8%) compared to control (0 mg NAA/L). NAA at higher concentrations (>50 mg/L) had a supressing effect on most parameters. It was inferred that yield production in okra is influenced by multiple yield-determining component traits and their mutual interactions which could be manipulated by the application of NAA. Foliar application of NAA (30-50 mg/L) have a beneficial impact on plant characters and yield of Okra, hence recommended in Okra cultivation.

Keywords: *Abelmoschus esculentus*, NAA, component traits, foliar application, growth, pod yield

Introduction

Okra (*Abelmoschus esculentus* L. Moench) is a monetarily critical crop, indeterminate in nature and widely grown in tropical and subtropical regions of the world (Gemede *et al*., 2015). The crop is produced for tender pods (fruits) which can be harvested over multiple times. It is far more nutritious than tomato, brinjal, and several other cucurbits with average nutritive value of 3.21 (Adelakun and Oyelade, 2011). The pods are highly nutritious and a very good source of dietary fibre, protein, phosphorus, potassium, zinc, copper, calcium, magnesium, manganese, and fair amount of vitamins *viz*., thiamine, riboflavin, niacin, ascorbic acid, etc., (USDA Nutrient Database for Standard Reference, 2018). The immature pods (fresh or dried) are consumed as boiled or fried vegetables, as soup thickeners as well as used in salads and stews (Yadev and Dhankhar, 2002). Hence, Okra is a worthful crop ensuring excellent means of livelihood to small-scale farmers.

Okra is mostly grown in areas with plentiful sunlight throughout the day. It prefers loamy to sandy loam soils, however, heavier soils with good drainage capacity can produce well. It can tolerate a wide range of soil pH, but prefers soil with a pH ranging between 6.0-6.8. Soil-based NPK fertilizer application has been reported to ensure good yield in Okra (Babatola, 2006).

Despite the wider production and numerous uses of Okra, there are many constraints contributing to the lower yields, some major ones include soil infertility, limited irrigation resources, adverse environmental conditions leading to unwanted abscission of floral bud and/or developing fruit (Iderawumi *et al*., 2017), etc. For normal growth an production, Okra crop need a temperature between 24 °C and 28 °C (Benchasri, 2012). Seed germination is delayed and decreased, at higher temperatures beyond 38 °C to 42 °C, flowers may parch and drop, causing yield loss. Despite its considerable tolerance to drought, the crop requires good availability of soil water for optimum growth. High yield reduction has been shown in the water stressed plants (Gunawardhana and de-Silva, 2011). In such situations, exogenous application of plant growth regulators (PGRs) have been found to be effective and useful (Husen *et al*., 2016; Liu *et al*., 2014), if applied in suitable forms and at appropriate concentrations.

*Author for correspondence; E-mail: sohail.wur@gmail.com

The PGRs are known to modify and regulate many growth and physiological processes in plants (Raddadi *et al*., 2008). They can improve the physiological efficiency of plants such as enhancing the photosynthetic ability of plants as well as stimulating the translocation of photo-assimilates to yield related plant components due to better source-sink relationships and, thereby increasing the overall crop productivity (Dawood and Sadak, 2008). The PGRs have therefore, been known to be one of the quick means of increasing production (Maity *et al*., 2016).

Auxins are considered an important group of PGRs (Anjum *et al*., 2011) which play a vital role in cell multiplication and enlargement, adventitious roots formation (Majda and Robert, 2018), apical dominance (Abdoli *et al*., 2013), and inducing flowering (Malik, 1999). Naphthalene acetic acid (NAA) is among one of the most beneficial PGRs in auxin family. Studies have shown that NAA plays a key function in improving the growth, yield as well as quality of the produce (Singh *et al*., 2017).

Although, PGRs have great potential, their application, optimal concentration, and plant species specificity have not been fully assessed in important vegetable crops and particularly in Okra. Along these lines, taking into account the positive role of PGRs, this study was designed to determine the impact of exogenous application of NAA on the pod yield including pod quality attributes by optimizing the concentration of NAA.

Materials and Methods

Plant material. A certified Okra cv. "Sabz Pari" was used in this study. It is early maturing (< 90 days) with light green pod colour (Fatima *et al*., 2019; Khan *et al*., 2013).

Field experiment. The field experiment was conducted to assess yield formation in aforementioned Okra variety in two consecutive growing seasons (March-July) of 2014 and 2015 referred to as GS_1 and GS_2, respectively throughout the text. The experimental site was under the auspices of Agricultural Research Institute, Dera Ismail Khan, Khyber Pakhtunkhwa, Pakistan and situated between latitude 31º 52' N, longitude 70º 53' E with altitude of 182 m from sea level.

The experiment was set out in a randomised complete block design with different NAA treatments replicated thrice. Six NAA solutions were obtained by dissolving NAA in distilled water using concentrations of 10, 30, 50, 70, 90, and 110 mg/L along with control (0 mg NAA/L) having distilled water only. Ethanol (10 mL) was used to facilitate the dissolution process.

The experimental site was assessed for basic physico-chemical soil properties prior to execution of the experiment (Table 1). Soil samples were air-dried, ground in a mortar and pestle and screened through ≥ 2 mm mesh for measuring the soil texture (Koehler *et al*., 1984). Soil pH was assessed by hand-held pH meter (JENWAY-3020). Electrical conductivity (EC) was evaluated *via* conductivity meter (inoLab). Soil organic matter (OM) content (Nelson and Sommers, 1982), ammonium-N, nitrate-N, total N (Keeney and Nelson, 1982), phosphorus (Olsen and Sommers, 1982), and potassium (Knudsen *et al*., 1982) contents were also ascertained. Soil properties did not vary considerably between the two growing seasons. The soil was a clay-loam, marginally alkaline (pH: 7.15-7.51), salt-free (EC: 140-170 µS/cm), short in OM (0.93-1.01 %), appropriate regarding ammonium-N (9.21-9.37 mg/Kg), nitrate-N (7.89-8.05 mg/Kg), total N (0.089-0.096%), potassium (157-163 mg/Kg) contents and rich in phosphorus (43.64-45.13 mg/Kg).

Standard cultivation practices were used in seedbed preparation. N (120 Kg/ha), phosphorus (90 Kg/ha), and potassium (60 Kg/ha) were incorporated before seed sowing as urea, single super phosphate (SSP), and

Table 1. Pre-planting physical and chemical properties of the soil.

Parameters	Unit	GS_1†	GS_2‡
AB-DTPA extractable phosphorus (P_2O_5)	mg/Kg	45.13	43.64
Ammonium acetate extractable potassium (K_2O)	mg/Kg	163	157
Ammonium nitrogen (NH_4-N)	mg/Kg	9.37	9.21
Nitrate nitrogen (NO_3-N)	mg/Kg	8.05	7.89
Total nitrogen	%	0.096	0.089
Organic Matter (OM)	%	1.01	0.93
pH	-	7.15	7.51
Electrical Conductivity (EC)	µS/cm	170	140
Texture class	-	Clay-loam	Clay-loam

† = Growing season of 2014; ‡ = Growing season of 2015.

sulphate of potash (SOP), respectively. Nitrogen was given in two equal split doses, first at time of planting and second at the onset of flowering. Seeds were pre-soaked in distilled water before sowing for 24 h to ensure consistent germination. The pre-germinated seeds were planted on ridges 60 cm apart and maintaining 30 cm intra-row spacing. Each block consisted of seven plots of afore-mentioned treatments making total of 21 plots across the three replicates. There were 4 ridges per treatment plot each possessing 10 plants thereby constituting the net plot size of 7.2 m^2 (2.4×3 m) with a total of 40 plants.

NAA treatments along with control were applied to each plot after 30 days of sowing by foliar application with the help of atomizer (Unamba *et al*., 2009). An adhesive Tween-20 (0.1%) was added to each solution according to Roy *et al*. (1991). Control plots were treated only with distilled water. Crop was managed well to avoid any kind of plant stress.

Meteorological temperature and precipitation data were collected from a local weather station during both the growing seasons (Fig. 1). The average monthly air temperature in GS_1 (March-July) was 18.0 to 33.0 °C, whereas it ranged from 19.0 to 32.5 °C in GS_2. The total precipitation was 248.5 and 156.5 mm during the growing season GS_1 and GS_2, respectively. This clearly indicated that the weather during GS_1 was comparatively wetter than GS_2.

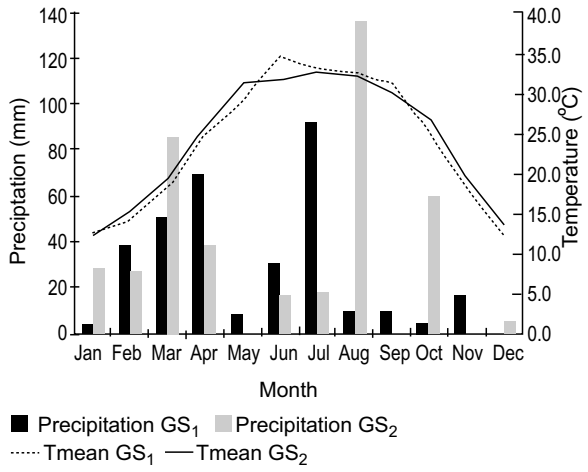

Fig. 1. Meteorological trends during two growing seasons of Okra (*i.e*., GS_1 = 2014; GS_2 = 2015).

Measurements. Data were compiled on a range of parameters shaping vegetative and reproductive growth, pod characteristics and yield during the crop cycle in two growing seasons. Plant height (cm), leaves/plant, total plant leaf area (cm^2), internodes/plant, and internode length (cm) were noted at time of first flowering. The onset of first flowering was estimated at commencement of 50% plants' flowering. Pod length (cm), pod diameter (mm), and pod fresh weight (g) was noted at every picking and mean value was estimated. Total pods/plant and pod yield (t/ha) were estimated from the summation of all pickings made. Standard rules developed by the International Union for the Protection of New Varieties of Plants (UPOV, 2018) and The International Plant Genetic Resources Institute (IPGRI, 1991) were adopted for all parameters measuring.

Statistical analysis. Recorded data were analysed statistically in Genstat (Payne *et al*., 2009). A preliminary analysis of data indicated non-significant differences between the two growing seasons (data not shown). Therefore, a general one-way analysis of variance (ANOVA) technique for each growing season was followed to test the extent and significance of variations among NAA treatments. Differences among treatments means were compared through Fisher's multiple comparison test using 5% probability level. Pearson correlations were quantified to appraise the inter-relationships among the parameters.

Results and Discussion.

Assessing impact of NAA on vegetative growth of Okra. Various concentrations of NAA had highly significant ($P \leq 0.001$) impact on parameters determining the vegetative growth of Okra in both growing seasons (*i.e*. GS_1 and GS_2). In GS_2, NAA at 30 mg/L produced the maximum plant height (84.0 cm), leaves/plant (29.1), total plant leaf area (13818 cm^2), internodes/plant (22.2), and internode length (8.0 cm) (Table 2). Values of most parameters remained statistically at par with 50 mg/L NAA. Data obtained in GS_2 indicated almost similar trend with 30 and 50 mg/L NAA producing the maximum plant height (78.5 and 77.4 cm) leaves/plant (24.4 and 23.0), total plant leaf area (10946 and 10038 cm^2), internodes/plant (19.8 and 18.5), and internode length (5.6 and 5.2 cm, accordingly) and remained statistically alike with each other for most parameters. Data also indicated that the maximum concentration of NAA (110 mg/L) led to reduced plant height (50.7 and 45.1 cm), leaves/plant (18.4 and 14.5), total plant leaf

area (5048 and 4529 cm^2), internodes/plant (16.4 and 14.0), and internode length (5.2 and 4.3 cm) in GS_1 and GS_2, respectively. However, results were statistically alike at control (0 mg NAA/L) for most parameters. Data pooled over two growing seasons indicated gain in most parameters determining vegetative growth in response to certain NAA concentration (mostly up to 30 mg/L). Additional rise in NAA concentration (> 30 mg/L) had a supressing effect on most of parameters. This was also apparent from a quadratic relationship between plant height, leaves/plant, total plant leaf area, internodes/plant, internode length and NAA concentrations with R^2 ranging from 80 to 98% (Fig. 2a-e).

Assessing impact of NAA on reproductive growth of Okra. NAA application induced a highly significant ($P \leq 0.001$) impact on earliness to flowering in both the growing seasons. Days required to first flowering ranged between 53.0–72.7 in GS_1 and 51.1–70.7 in GS_2 (Table 3). The plants without NAA application (*i.e*., control) exhibited delayed onset of first flowering significantly and took 60.0 and 58.0 days, whereas earlier start of flowering (53.0, 51.1 days) was recorded with 10 mg/L NAA concentration in GS_1 and GS_2, respectively. NAA applied at 30 mg/L appeared second most influential concentration in initiating early flowering (55.8 and 52.6 days) in plants during both the seasons. Data further indicated a strong quadratic link (R^2 = 96%) between days required to first flowering and NAA concentrations (Fig. 2f). In conclusion, onset of first flowering advanced with lowest NAA concentration and gradually delayed with increase in NAA concentration till 110 mg/L and produced maximum delay in first flowering in GS_1 and GS_2, respectively.

Assessing impact of NAA on pod characteristics. Parameters determining the pod characteristics were significantly ($P \leq 0.001$) influenced by NAA application in both seasons. Maximum pod length (11.0 and 12.3 cm) was noted with the foliar application of 30 mg NAA/L among the treatments apart from 10 mg NAA/L (10.7 and 12.0 cm) and 50 mg NAA/L (10.1 and 11.4 cm) in GS_1 and GS_2, respectively (Table 3). Similarly, NAA concentration (30–50 mg/L) exhibited major increase in pod diameter and pod fresh weight and ranged between 14.3–16.0 mm and 15.2–17.6 g, respectively across both the seasons. However, statistically both NAA treatments were alike. The absence of NAA application (control) produced minimum pod length (8.9 and 10.2 cm), pod diameter (9.3 and 10.6 mm), and pod fresh weight (6.8 and 8.1 g) in GS_1 and GS_2, respectively. Data also indicated that higher concentration of NAA (70–110 mg/L)

Table 2. Effect of naphthalene acetic acid (NAA) concentrations on the vegetative growth of Okra during two growing seasons.

NAA (mg/L)	Plant height (cm)	Leaves/ plant	Total plant leaf area (cm^2)	Internodes/ plant	Internode length (cm)
GS_1†					
0	52.5 e	18.8 d	6161 cd	13.4 d	4.9 f
10	73.0 c	23.9 c	10102 b	18.1 abc	7.7 b
30	84.0 a	29.1 a	12314 ab	22.2 a	8.0 a
50	82.8 a	28.5 ab	13818 a	20.9 ab	7.6 b
70	78.0 b	23.6 bc	10661 b	19.8 abc	7.0 c
90	67.0 d	19.7 cd	7361 c	17.2 bcd	5.9 d
110	50.7 e	18.4 d	5048 d	16.4 cd	5.2 e
LSD ($P \leq 0.05$)	4.0	5.0	2313.6	4.1	0.13
GS_2‡					
0	49.3 d	15.7 d	4715 c	11.0 d	4.0 f
10	69.8 b	20.1 bc	7734 b	15.8 bc	5.3 b
30	78.5 a	24.4 a	10946 a	19.8 a	5.6 a
50	77.4 a	23.0 ab	10038 a	18.5 ab	5.2 bc
70	71.3 b	21.0 b	7934 b	17.4 abc	5.0 c
90	59.2 c	17.4 cd	5842 c	14.8 bc	4.7 d
110	45.1 e	14.5 d	4529 c	14.0 cd	4.3 e
LSD ($P \leq 0.05$)	3.4	3.3	1663.5	3.7	0.20

Means with unlike letter(s) are significantly different; † = Growing season of 2014; ‡ = Growing season of 2015.

Table 3. Effect of naphthalene acetic acid (NAA) concentrations on the reproductive growth, pod characteristics and yield of Okra during two growing seasons

NAA (mg/L)	Onset of first flowering	Pod length (cm)	Pod diameter (mm)	Pod fresh weight (g)	Total pods/plant	Pod yield (t/ha)
GS1†						
0	60.0 c	8.9 c	9.3 e	6.8 f	11.5 g	5.8 f
10	53.0 f	10.7 a	13.0 c	12.7 d	22.3 a	15.7 d
30	55.8 e	11.0 a	14.7 a	16.3 a	21.5 b	20.8 a
50	57.0 de	10.1 ab	14.3 a	15.2 ab	19.9 c	19.8 b
70	59.1 cd	9.6 bc	13.5 b	14.3 bc	18.3 d	18.0 c
90	67.0 b	9.5 bc	13.1 bc	13.5 cd	14.0 e	14.8 d
110	72.7 a	9.1 c	11.8 d	10.5 e	13.3 f	10.7 e
LSD (P≤0.05)	2.6	0.97	0.51	1.4	0.67	1.0
GS2‡						
0	58.0 c	10.2 c	10.6 e	8.1 f	10.3 f	5.0 e
10	51.1 e	12.0 a	13.0 d	14.0 d	19.7 a	15.0 c
30	52.6 e	12.3 a	16.0 a	17.6 a	18.9 b	19.0 a
50	53.3 de	11.4 ab	15.6 ab	16.5 ab	18.5 b	18.4 a
70	56.0 cd	10.9 bc	14.8 bc	15.6 bc	17.3 c	16.7 b
90	63.5 b	10.4 bc	14.4 c	14.8 cd	13.4 d	14.1 c
110	70.7 a	10.0 c	13.1 d	11.8 e	12.8 e	9.0 d
LSD (P≤0.05)	3.4	1.0	0.79	1.2	0.60	1.5

Means with unlike letter(s) are significantly different; † = Growing season of 2014; ‡ = Growing season of 2015.

negatively affected the pod length, diameter and fresh weight among all the treatments in both the growing seasons. The combined data from two growing seasons further indicated a strong quadratic relationship between pod length, diameter, fresh weigh and NAA concentration with R^2 ranging from > 63% to 90% (Fig. 2g-h & Fig. 3a). In other words, all these parameters increased positively with NAA application up to certain concentration (30 mg/L) and reduced with further rise in NAA concentration. These results indicated that higher concentration of NAA (≥ 70 mg/L) may induce a negative effect on pod characteristics. However, NAA application is still better than control (0 mg NAA/L) which overall resulted into minimum values of these parameters.

Assessing impact of NAA on yield formation in Okra. The reposted data showed significant (P≤0.001) effect of NAA application on the yield formation in Okra. The significantly greater (22.3 and 19.7) pods/plant were observed in treatments receiving 10 mg/L NAA followed by 30 mg/L NAA producing 21.5 and 18.9 pods/plant in GS_1 and GS_2, respectively (Table 3). On the other hand, foliar application of 30 and 50 mg/L NAA produced maximum pod yields during both the seasons and ranged from 18.4 to 20.8 t/ha. However, results were statistically alike in GS_2 between these two NAA treatments. The control treatment (0 mg NAA/L) exhibited lowest (11.5 and 10.3) pods/plant and minimum pod yield (5.8 and 5.0 t/ha) in GS_1 and GS_2, respectively among all the treatments. Data showed the quadratic relationship between pods/plant, pod yield and different concentration of NAA (R^2 = 86–93%) as illustrated by Fig. 3b-c. The results overall suggested that pod production enhanced with lower NAA concentrations (10–30 mg/L). Further concentration of NAA induced a gradual declination in pod yield.

Assessing correlations between yield and yield-contributing parameters of Okra. Data revealed significant (P≤0.001) inter-relationships among the parameters (Fig. 4). There existed positive very strong correlations (r ≥ 0.70) between plant height and leaves/plant, total plant leaf area, internodes/plant, internode length, pod fresh weight, and pods/plant (r = 0.77–0.88), between leaves/plant and total plant leaf area, internodes/plant, internode length, and pods/plant (r = 0.72–0.96), between total plant leaf area and internodes/plant, internode length, and pods/plant (r = 0.77–0.80), between internodes/plant and internode length (r = 0.73), between pod diameter and pod fresh weight (r = 0.93), between pods/plant and internode length (r = 0.72).

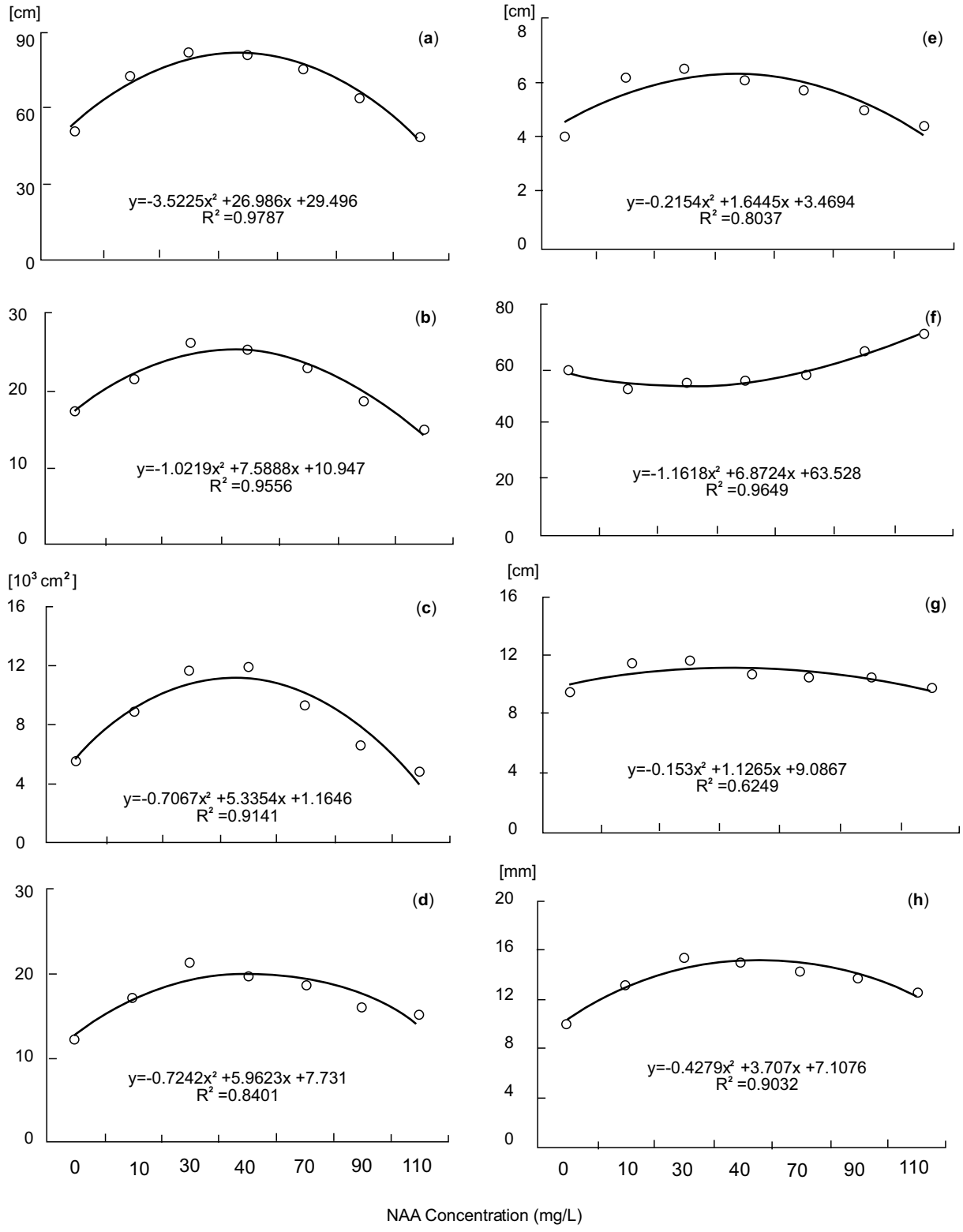

Fig. 2. Effect of different concentrations of naphthalene acetic acid (NAA) on (**a**) plant height, (**b**) leaves/plant, (**c**) total plant leaf area, (**d**) internodes/plant, (**e**) internode length, (**f**) onset of first flowering, (**g**) pod length, (**h**) pod diameter.

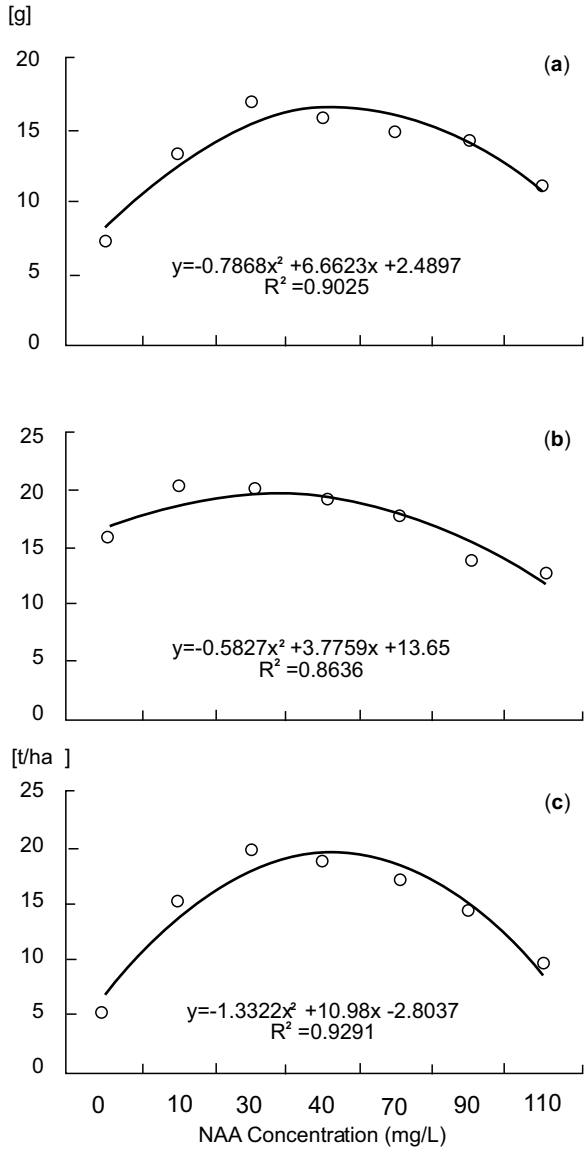

Fig. 3. Effect of different concentrations of naphthalene acetic acid (NAA) on (**a**) pod fresh weight, (**b**) total pods/plant, (**c**) pod yield.

Furthermore, fairly strong positive correlations (0.40 $\leq$ r $\leq$ 0.70) existed between plant height and pod length, pod diameter (r = 0.47-0.68); between leaves/plant and pod diameter, pod fresh weight (r = 0.47–0.53), between total plant leaf area and pod diameter, pod fresh weight, pods/plant (r = 0.60–0.64), between internodes/plant and pod diameter, pod fresh weight (r = 0.47–0.53), between internode length and pod fresh weight (r = 0.42), between pod length and pod diameter, pod fresh weight, pods/plant (r = 0.43–0.65), between pod fresh weight and pods/plant (r = 0.45).

Data also exposed very strong negative correlations (r = - 0.80) between pods/plant and onset of first flowering. There existed fairly strong negative correlations (- 0.40 $\leq$ r $\leq$ - 0.70) between onset of first flowering and plant height, leaves/plant, total plant leaf area, pod length, pod fresh weight with "r" values ranging from - 0.40 to - 0.67.

Data further revealed very strong positive correlations (r $\geq$ 0.70) between pod yield and most of the parameters including plant height, leaves/plant, total plant leaf area, internodes/plant, pod diameter, pod fresh weight with value of r ranging between 0.70 to 0.92 (Fig. 4). Data also showed reasonably strong positive correlations (0.40 $\leq$ r $\leq$ 0.70) between pod yield and pod length, pods/plant (r $\leq$ 0.48 – 0.64). Pod yield indicated strong negative relationship (r = - 0.51) with the onset of first flowering amongst the rest of parameters.

This study aimed to assess the influence of NAA on the growth and yield production in Okra. Foliar application of NAA positively affected the parameters determining the vegetative, reproductive and yield formation in Okra. Lower concentration of NAA (30–50 mg/L) induced maximum plant height, leaves/plant, total plant leaf area, internodes/plant, internode length, pod length, pod diameter, pod fresh weight, and pod yield. Furthermore, results indicated the mean increase in plant height (59.5 and 57.2 %), number of leaves/plant (50.4 and 45.5 %,), total plant leaf area (113.9 and 119.4 %), internodes/plant (72.5 and 61.6 %), internode length (53.2 and 44.5 %), pod diameter (53.5 and 49.9 %), pod fresh weight (126.8 and 111.8 %), and pod yield (271.2 and 255.8 %) with the application of 30 and 50 mg/L NAA, respectively, over control (0 mg NAA/L). However, NAA concentration of 10 and 30 mg/L increased the pod length up to 19.0 and 21.07 %, and pods/plant up to 31.1 and 27.9 %, respectively over control (0 mg NAA/L).

The increase in vegetative growth could be due to stimulated cell multiplication and elongation of internodes (Dhage *et al*., 2011). Studies by Abdo and Abdel-Aziz (2009) and Kumar *et al*. (2018) also revealed that exogenous application of NAA up to 50 mg/L improved the overall vegetative growth and leaf area of the plant. Furthermore, more pod yield with lower NAA concentrations (30 and 50 mg/L) might be due to

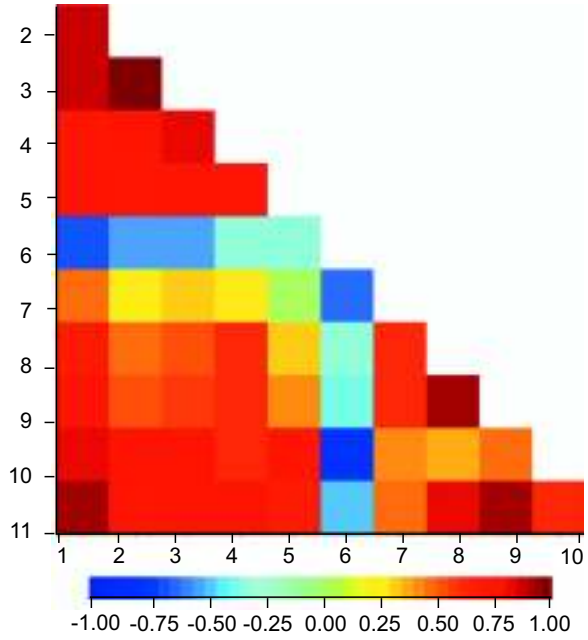

Fig. 3. A colour heat map exposing correlations among growth and yield-determining parameters of Okra, where:

1 = Plant height; 2 = Leaves/plant; 3 = Total plant leaf area; 4 = Internodes/plant; 5 = Internode length; 6 = Onset of first flowering; 7 = Pod length; 8 = Pod diameter; 9 = Pod fresh weight; 10 = Total pods/plant; 11 = Pod yield. Colour bars represent the strength of the Pearson's correlation coefficient "r".

better translocation of photo-assimilates to the developing pods and seeds (Ravat and Makani, 2015). This could also be due to enhanced source sink relationship initiated by exogenous NAA application that in turn stimulated the heavier build-up of sufficient food reserves thereby helping in effective pod development and ultimately enhancing the pod yield (Huang *et al*., 2018). Various studies have reported the effectiveness of NAA towards inducing pod production in other crops including lablab bean (Uddin *et al*., 1994), pigeonpea (Rao and Narayan, 1997), and chickpea (Karim, 2005). Our results were supported by Meena (2015) and Singh *et al*. (2017), who also accounted increase in most of the growth traits, yield-components and overall pod yield in Okra with the application of NAA.

Furthermore, it was observed that application of NAA at higher concentrations (> 50 mg/L) had a supressing effect on most of parameters. This was also apparent from a quadratic relationship between most of parameters and NAA concentrations. For instance, the onset of first flowering became 7 and 5 days earlier with the application of lower rates of NAA (10 and 30 mg/L, respectively) and gradually delayed with rise in NAA concentration till the maximum level (110 mg/L) and produced maximum delay (12.7 days) in the start of first flowering over control (0 mg NAA/L) (Mustafa *et al*., 2016). This could be associated with suppression of metabolic pathways responsible for early flowering at higher NAA concentration (Huang *et al*., 2018). It was interesting to note that results of NAA (110 mg/L) and control (0 mg NAA/L) were statistically alike for most parameters. However, NAA application was still better than control (0 mg NAA/L) which overall led to minimum vegetative growth and pod yield. This was evident from the fact that different NAA concentrations (10, 30, 50, 70, 90, 110 mg/L) increased the pod yield in the range of 185.8, 271.2, 255.8, 224.3, 169.7 and 83.6 %, respectively over control (0 mg NAA/L).

Analysis of correlation coefficients revealed strong and positive inter-relationships between most of the parameters (Fatima *et al*., 2019). Highly strong association between pod yield and growth parameters *viz*., plant height, leaves/plant, total plant leaf area, internodes/plant, internode length and yield-components such as pod diameter, pod fresh weight, and number of pods/plant revealed that these are the vital yield determinants in Okra (Falusi *et al*., 2012). Negative association between pod yield and the onset of first flowering suggested that a delay in flowering might have a detrimental impact on yield production in Okra mainly due to shortening of the reproductive growth period influenced by uncongenial environmental conditions (Bruns, 2009). It was inferred that yield constitution in Okra is influenced by multiple yield-contributing traits and their mutual inter-associations. Selecting for such traits would assist in formulating an indirect selection criterion for yield improvement in Okra (Fatima *et al*., 2019).

Conclusion

This study clearly indicated that foliar application of NAA had a marked impact on parameters determining the vegetative, reproductive, and yield formation in

Okra. Overall, application of NAA in the range of 30–50 mg/L appeared the best levels for increased pod yield. Results concluded that yield-contributing characters and pod yield of Okra could be manipulated by the application of NAA. Therefore, foliar application of NAA at the rate of 30-50 mg/L may be recommended for ensuring better Okra yield.

Acknowledgement

We thanks the staff of Department of Soil and Environmental Sciences, the University of Agriculture, Peshawar, Pakistan for performing the soil analyses.

Conflict of Interest. The authors declare no conflict of interest.

References

Abdo, F.A., Abdel-Aziz, E.S.A. 2009. Response of soybean to foliar spraying with growth regulators mixture and zinc. *Egyptian Journal of Applied Science*, **24:** 215-238.

Abdoli, M., Saeidi, M., Jalali-Honarmand, S., Azhand, M. 2013. The effect of foliar application of indol-3-acetic acid (IAA) and roles of ear photosynthesis on grain yield production of two wheat cultivars (*Triticum aestivum* L.) under post anthesis water deficit. *International Research Journal of Applied and Basic Sciences*, **4:** 1406-1413.

Adelakun, O.E., Oyelade, O.J. 2011. Chapter 99 - Chemical and antioxidant properties of okra (*Abelmoschus esculentus* Moench) seed. In: *Nuts and Seeds in Health and Disease |Prevention*, Preedy, V.R., Watson, R.R., Patel, V.B., (eds.), pp. 841-846, Academic Press, USA.

Anjum, M.A., Zahir, Z.A., Arshad, M., Ashraf, M. 2011. Isolation and screening of rhizobia for auxin bio-synthesis and growth promotion of mung bean (*Vigna radiata* L.) seedlings under axenic conditions. *Soil and Environment*, **30:** 18-26.

Babatola, L.A. 2006. Effect of NPK 15:15:15 on the performance and storage life of okra (Abelmoschus esculentus). *In: Proceedings of the Horticultural Society of Nigeria Conference*, 125-128.

Benchasri, S. 2012. Okra (*Abelmoschus esculentus* (L.) Moench) as a valuable vegetable of the world. *Ratarstvo i povrtarstvo - Journal on Field and Vegetable Crops Research*, **49:** 105-112.

Bruns, H.A. 2009. A survey of factors involved in crop maturity. *Agronomy Journal*, **101:** 60-66.

Dawood, M.G., Sadak, M.S. 2008. Physiological response of canola plants (*Brassica napus*) to tryptophan and benzylalanine. *Seria Agronomie*, **50:** 198-207.

Dhage, A.A., Nagre, P.K., Bhangre, K.K., Papu, A.K. 2011. Effect of plant growth regulators on growth and yield parameters of Okra. *Asian Journal of Horticulture*, **6:** 170-172.

Falusi, O.A., Dangana, M.C., Daudu, O.Y., de-Silva, J.A.T. 2012. Studies on morphological and yield parameters of three varieties of Nigerian Okra [*Abelmoschus esculentus* (L.) Moench]. *Journal of Horticulture and Forestry*, **4:** 126-128.

Fatima, S., Khan, M.S., Nadeem, M., Khan, I., Waseem, K., Nisar, M., Iqbal, M. 2019. Interactive effects of genotype and nitrogen on the phenology and yield determination of Okra (*Abelmoschus esculentus* L.). *International Journal of Plant Production*, **13:** 73?90.

Gemede, H.F., Ratta, N., Haki, G.D., Woldegiorgis, A.Z., Beyene, F. 2015. Nutritional quality and health benefits of Okra (*Abelmoschus esculentus*): a review. *Journal of Food Processing and Technology*, **6:** 1-6.

Gunawardhana, M.D.M., de-Silva, C.S. 2011. Impact of temperature and water stress on growth yield and related biochemical parameters of Okra. *Journal of Tropical Agricultural Research*, **23:** 77-83.

Huang, Y., Zeng, X., Cao, H. 2018. Hormonal regulation of floret closure of rice (*Oryza sativa*). *PLoS One*, **13:** e0198828.

Husen, A., Iqbal, M., Aref, I.M. 2016. IAA-induced alteration in growth and photosynthesis of pea (*Pisum sativum* L.) plants grown under salt stress. *Journal of Environmental Biology*, **37:** 421-429.

Iderawumi, A.M., Friday, C.E., Mubo, O.A. 2017. Nutritional evaluation of Okra pod and mother soil as influenced by sawdust ash, ammonium nitrate and NPK. *Environment and Ecology Research*, **5:** 334-339.

IPGRI (*The International Plant Genetic Resources Institute*). 1991. International crop network series. Report of an international workshop on Okra genetic resources. International Board for Plant Genetic Resources, Rome.

Karim, M.F. 2005. Physiological and biochemical responses of chickpea (*Cicer arietenum* L.) following application of fertilizers and growth regulators. *Ph.D. Thesis*. Department of Botany, Dhaka University, Dhaka-1000, Bangladesh.

Keeney, D.R., Nelson, D.W. 1982. Nitrogen-inorganic forms. In: *Methods of Soil Analysis*, Part-2, Page, A.L. Miller, R.H. Keeney D.R. (eds.), pp. 643-698, American Society of Agronomy, Madison, W.I., USA.

Khan, M.A., Sajid, M., Hussain, Z., Rab, A., Marwat, K.B., Wahid, F.I., Bibi, S. 2013. How nitrogen and phosphorus influence the phenology of Okra. *Pakistan Journal of Botany*, **45:** 479-482.

Knudsen, D., Peterson, G.A., Pratt, P.F. 1982. Lithium, sodium and potassium determination. In: *Methods of Soil Analysis*, Part-2, Page, A.L., Miller, R.H., Keeney, D.R. (eds.), pp. 228-239. American Society of Agronomy, Madison, W.I., USA.

Koehler, F.E., Moodie, C.D., McNeal, B.L. 1984. *Laboratory Manual for Soil Fertility.* Washington State University, Department of Agronomy and Soils. Pullman, Washington, USA.

Kumar, V., Jat, P.K., Mukherjee, S., Singh, S.P. 2018. Role of plant growth regulator's in strawberry. *International Journal of Chemical Studies*, **6:** 949-954.

Liu, L., Guo, G., Wang, Z., Ji, H., Mu, F., Li, X. 2014. Auxin in plant growth and stress responses. In: *Phytohormones: A Window to Metabolism, Signaling and Biotechnological Applications*, Phan, L.S., Tran, S., Pal (eds.), pp. 35. Springer Science + Business media New York, USA.

Maity, U., Dutta, P., Layek, B. 2016. Effect of plant growth regulators on growth, yield and quality of Okra (*Abelmoschus esculentus* (L.) Moench). *Journal of Agroecology and Natural Resource Management*, **3:** 251-253.

Majda, M., Robert, S. 2018. The role of auxin in cell wall expansion. *International Journal of Molecular Sciences*, **19:** 1-21.

Malik, C.P. 1999. *Introduction in Advances in Plant Hormones Research: Indian Scenario. Agro Botanica*, New Delhi, India, pp. 14-15.

Meena, O.P. 2015. A review: role of plant growth regulators in vegetable production. *International Journal of Agricultural Science Research*, **5:** 71-84.

Mustafa, A.,Hussain, A., Naveed, M., Ditta, A., Nazli, Z.E.H., Sattar, A. 2016. Response of Okra (*Abelmoschus esculentus* L.) to soil and foliar applied L-tryptophan. *Soil and Environment*, **35:** 76-84.

Nelson, D.W., Sommers, L.E. 1982. Total carbon, organic carbon and organic matter. In: *Methods of Soil Analysis*, Part-2, Page, A.L., Miller, R.H., Keeney, D.R. (eds.), pp. 539-577. American Society of Agronomy, Madison, W.I., USA.

Olsen, S.R., Sommers, C.E. 1982. Phosphorus in soil Analysis. In: *Methods of Soil Analysis*, *Part-2*, Miller, A.L., Keeney, R.H., Keeney, D.R. (eds.), pp. 403-430. American Society of Agronomy, Madison, W.I., USA.

Payne, R.W., Murray, D.A., Harding, S.A., Baird, D.B., Soutar, D.M. 2009. *GenStat for Windows* (12th edition) Introduction. VSN International, Hemel, Hempstead.

Raddadi, N., Cherif, A., Boudabous, A., Daffonchio, D. 2008. Screening of plant growth promoting traits of *Bacillus thuringiensis*. *Annals of Microbiology*, **58:** 47-52.

Rao, J.S.P., Narayanan, A. 1997. Effect of water, light stress and foliar application of auxins on flower abscission and seed yield of pigeon pea. *Madras Agricultural Journal*, **84:** 127-129.

Ravat, A.K., Makani, N. 2015. Influence of plant growth regulators on growth, seed yield and seed quality in Okra (*Abelmoschus esculentus* (L.) Moench) cv. GAO-5 under middle Gujarat condition. *International Journal of Agricultural Sciences*, **11:** 151-157.

Roy, D.S., Kabir, J., Chatterjee, R., Mitra, S.K. 1991. Effect of postharvest foliar spray of some chemicals in storage behaviour of onion. *Onion Newsletter for the Tropics*, **3:** 23-25.

Singh, D., Vadodaria, J.R., Morwal, B.R. 2017. Effect of GA3 and NAA on yield and quality of Okra (*Abelmoschus esculentus* L). *Journal of Krishi Vigyan*, **6:** 65-67.

Uddin, M.M., Quadir, M.A., Choudhury, A.R., Choudhury, M.K. 1994. Effects of growth regulators on growth and pod yield of lablab bean grown in summer. *Journal of Bangladesh Agricultural University*, **4:** 79-85.

Unamba, C.I.N., Ezeibekwe, I.O., Mbagwu, F.N. 2009. Comparative effect of the foliar spray and seed

soaking application method of gibberellic acid on the growth of *Abelmoschus esculentus* (Okra dwarf). *Journal of American Science*, **5:** 133-140.

UPOV (Union for the Protection of New Varieties of Plants). 2018. http://www.upov.int

USDA (United States Department of Agriculture, Agricultural Research Service), 2018. USDA nutrient database for standard reference, Release 1 April 2018. Retrieved January 21, 2019, from http://ndb.nal.usda.gov/ndb/

Yadev, S.K., Dhanker, B.S. 2002. Performance of 'Varsha Uphar' cultivar of Okra as affected by sowing dates and plant geometry. *Vegetable Science*, **27:** 70-74.

Pak. j. sci. ind. res. Ser. A: phys. sci. 2021 **64A**(1) 46-51

Soil Characteristics and Fertility Indexation in Gujar Khan Area of Rawalpindi

Obaid ur Rehman[a]*, Shahzada Munawar Mehdi[b], Raja Abad[a], Shahid Saleem[a], Rizwan Khalid[a], Sarosh Tariq Alvi[a] and Asia Munir[a]

[a]Soil & Water Testing Laboratory for Research, Rawalpindi, Pakistan

[b]Director Soil Fertility Research Institute, Punjab, Lahore, Pakistan

(received April 2, 2018; revised November 21, 2019; accepted December 9, 2019)

Abstract. Soil characteristics of Gujar Khan area of Rawalpindi district were evaluated through physical and chemical analysis. About 3002 soil samples were received/collected from farmers' fields of Gujar Khan during the period between 2012 and 2017 and analysed for texture, electrical conductivity (ECe), pH, organic matter (OM), available phosphorus (AP) and available potash (AK). The analysis results revealed that texture of the soils varied from sandy loam (33.5%) to loam (61.6%). The 98.6% soils had ECe values within the normal range (< 4 dS/m) and almost 74% soil had from 7.5 to 8.5 pH values with an average of 7.76. Thus there was no salinity/alkanity hazard in the area. Generally most of the soils were poor from the fertility point of view. About 96% soils were poor in both OM and AP contents, whereas, 3.0% soils have OM (>0.86%) and 3.4% satisfactory levels and AP (>7.0-14 mg/Kg). However, 62% soils has satisfactory to adequate AK status. The frequency distribution analysis indicated that 45% soils of Gujar Khan and OM content in the range of 0.4-0.6%, 57% and soil have AP in the range of 4.0-6.0 mg/Kg, while 50% and AK in the range of 81-120 mg/Kg. The soil fertility indexes in respect of OM and AP were low (1.0), whereas AK (1.7) indicating a medium fertility status of Gujar Khan soils.

Keywords: soil characteristics, Pothwar, NPK, Gujar Khan, fertility index

Introduction

In the North Eastern part of the Punjab province of Pakistan (latitude 32° 10' to 34º 9' N and longitude 71° 10' to 71° 55' E), the Pothwar plateau comprises of the district of Attock, Jhelum, Chakwal and Rawalpindi. It covers an area of 1.82 million ha, and topography ranges from flat to gently undulating, locally broken by gullies and low hill ranges. In general, the Pothwar soils are alkaline, calcareous, low in organic matter and deficient in plant nutrients like N and P (Khan and Joergensen, 2006; Nizami *et al*., 2004). Although it constitutes an important area for rainfed agriculture in the country, however crop yields are low as compared to irrigated regions of Pakistan. Main cause of low production are, highly erratic rainfall, water erosion and widespread deficiency of plant nutrients. Due to the loss of fine soil particles along with essential plant nutrients through runoff and inadequate fertilization, the soils of Pothwar suffer with multiple nutrient deficiencies (Rashid *et al*., 1997). In general, the Pothwar soils are alkaline, calcareous, low in organic matter and deficient in plant nutrients like nitrogen and phosphorus.

*Author for correspondence;
E-mail: agrichemist.rwp@gmail.com

Soil analysis is useful instrument for assessing the amount of nutrients availability. It is a rapid and less expensive method for evaluation of fertility status of soil and for recommendation of optimum fertilizer rates for economic crop production. There is a network of soil and water testing laboratories established throughout the country under the provincial setup. These laboratories are designed to meet the routine needs of farmers *i.e.* water analysis, soil analysis for texture, salinity/sodicity, and fertility status (Ahmed and Rashid, 2003).

The Gujar Khan area fall in Rawalpindi district lies between latitude 33° 10' to 33° 15' N and longitude 73° 15' to 73° -20' E. Soils of this area derived their parent material of underlying rocks like sandstone, limestone and shale, have medium (loam) to light (sandy loam) texture, poor fertility status in terms of organic matter and available phosphorus (Shaheen, 2016; Mahmood *et al*., 2010). However, majority of soils of Gujar Khan are generally well supplied with potassium (Khalid *et al*., 2002). Objective of this study is to evaluate soil fertility status of Gujar Khan area on the basis of soils samples collected from different areas during the years 2012-17.

Material and Methods

During the year 2012-17 approximately 3002 soil samples were either collected or obtained from farmers at the soil and water Testing Laboratory, Rawalpindi, Pakistan. Samples were dried, sieved and analysed for physico-chemical characteristics *i.e*., texture, EC_e, pH, soil organic matter, available P and available K by methods described by Page (1982). Soil texture was determined by measuring saturation percentage and Electrical Conductivity (ECe) by preparing soil and water (1:10) suspension (Malik *et al*., 1984a). The data was analysed using the MS Excel package for statistical analysis, shown in Table 1. Soil nutrient Index (SNI) was also calculated by following formula (Parker, 1951).

$$\text{Nutrient Index (NI)} = ((N_i \times 1) + (N_m \times 2) + (N_h \times 3))/ N_t$$

where:

N_t = Total number of samples analyzed in a given area; N_i = Number of samples falling in low category of given nutrient; N_m = Number of samples falling in medium category of given nutrient; N_h = Number of samples falling in high category of given nutrient.

The following criteria has been used for the categorisation of soil samples Malik *et al*. (1984a)

Results and Discussion

Soil texture. Soil texture is basic with many other properties and used as an indicator of water and nutrient holding capacity of soil. It is also a major factor in defining the proper soil management practices to be followed. Generally the soils of Gujar Khan area are light to medium textured. The analysis data showed that 33.5% soils was light and 61.6 % was medium textured (Table 2), whereas the proportion of heavy soil was just 4.9%. Khalid *et al*. (2002) reported 65% of soils as medium textured loam in Gujar Khan area. The soils of Gujar khan area derived from loess and sandstone parent material, moderately to severely eroded, have medium to light texture (Nizami *et al*., 2004). These light textured soils with less water holding capacity needs to be enhance through addition of organic manures. The medium textured (loam) soils, however, these are suitable for cultivation of all common crops. Ho *et al*. (2019) found siliceous sandy nature Spodosols soils in Sabal area of Malaysia, poor in nutrient retention capacity due to sandstone parent material and low clay contents.

Soil salinity/sodicity. In Gujar Khan region, the electrical conductivity (ECe) of most of the soil (98.6%) was within normal range (<4.0 dS/m) only 1.4% had salinity/sodicity with values > 4.0 dS/m. The soil pH ranged from 7.0 to 8.6 with in average value of 7.76 (Table 3). The data showed that 26 % soils has pH >7.5, while, 74% has 7.5-8.5 (Table 3). The soils have pH < 8.5 are considered as normal, while those having pH value > 8.5 as sodic. However, these were very rare (0.1%) in the study area (Table 2-3). Similar results were also reported by Shaheen (2016) and Fateh *et al*., (2006) for Gujar Khan area.

Table 1. Soil statistical analysis

(a)	**Soil texture**		
	SP (%)	Texture	
	19	Sandy	
	20-30	Sandy loam	
	31-45	Loam	
	46-60	Clay loam	
	> 60	Clay	
(b)	**Soil salinity/sodicity**		
	EC (dS/m)	Soil pH	Remarks
	<4.0	7.0 – 8.1	Normal
	>4.0	7.0– 8.5	Saline soil
	>4.0	> 8.5	Saline-Sodic soil
	< 4.0	> 8.5	Sodic soil
(c)	**Essential soil nutrients**		
	Organic matter (%)		Remarks
	< 0.86		Poor
	0.86 – 1.29		Satisfactory
	> 1.29		Adequate
	Phosphorus (mg/Kg)		Rating
	< 7.0		Poor
	7.1 – 14.0		Medium
	14.0 – 21.0		High
	> 21.0		Very high
	Potassium (mg/Kg)		Rating
	< 80		Poor
	80-180		Satisfactory
	> 180		Rich

a = soil texure; b = salinity/sodicity; c = essential soil nutrients.

Table 2. Soil characteristics of Gujar Khan

Parameter	Range	Mean	SD
Soil pH	7.0 – 8.6	7.76	0.26
EC	0.15 – 6.02	0.79	0.07
Organic matter	0.23- 1.29	0.53	0.25
Available phosphorus	2.3 -17.2	3.89	0.58
Available potash	40 - 320	103	12.01

Soil fertility status. The fertility status of the Gujar Khan soils was determined through estimation of organic matter for nitrogen, available phosphorus and potash. The results based up on analytical data are given as under.

Organic matter. Soil nitrogen requirement usually recommended on the basis of nitrogen released by the organic matter (OM) contents by soil testing laboratories (Cooke, 1982). There is a significant positive correlation between N and OM indicating that N nutrition of crops largely depends on the maintenance of organic matter levels in soil (Tsozue *et al*., 2016). The present data revealed that the OM ranges from 0.23-1.29% in the area with mean value of 0.53 (Tables 2). Majority (97%) of soils of Gujar Khan area had poor (< 0.86%) while, rest had satisfactory to adequate OM contents (Table 3). The frequency distribution data indicated that 45% fall in the range of 0.41 to 0.60% followed by 33% in 0.21-0.40% whereas, only 1.2% had OM contents more than 1% (Table 4). However, Shaheen (2016) reported OM in the range of 0.89 to 1.25% in eroded soils of Gujar Khan area. Khalid *et al*. (2012) reported OM content in the range of 0.4-0.6 %, in soils of Chakwal.

Organic matter makes its greatest contribution to soil productivity not only by providing nutrients but also improving its water holding capacity and physical properties (Sarwari *et al*., 2008). The soils of Pakistan are quite low in organic matter. Atreya *et al*. (2005) associated much of the soil OM loss from farm fields with the eroded sediments. Thus, higher the soil loss higher will be the soil OM losses. Erosion reduces organic matter and ultimately soil fertility. Soil fertility declination due to soil erosion and nutrients losses through runoff is a serious problem of hilly areas

Table 3. Analysis of Gujar Khan soil samples during the years 2012-17

Particulars	Year						
	2012-13	2013-14	2014-15	2015-16	2016-17	Total	(%)
a. Soil texture							
1. Light	2	733	288	281	203	1507	33.5
2. Medium	40	687	622	941	486	2776	61.6
3. Heavy	2	39	34	26	120	221	4.9
b. Salinity/sodicity							
1. Normal (ECe <4.0)	43	1439	941	1220	799	4442	98.6
2. Saline (ECe >4.0)	1	20	3	28	10	62	1.4
c. Soil pH							
1. >7.5	30	733	142	182	80	1167	25.9
2. 7.5-8.5	14	729	802	1066	720	3331	73.9
3. >8.5		6				6	0.1
d. Oraganic matter							
1. Poor (<0.86%)	41	1371	935	1213	797	4357	96.7
2. Satisfactory (0.86-1.29%)	2	80	9	35	8	134	3.0
3. Adequate (>1.29%)	1	7	0		5	13	0.3
e. Available phosphorous							
1. Poor (<7.0 mg/Kg)	37	1404	921	1196	767	4325	96.0
2. Satisfactory (7.0-14.0 mg/Kg)	6	51	18	46	30	151	3.4
3. Adequate (>14 mg/Kg)	1	3	5	6	13	28	0.6
f. Available potash							
1. Poor (<80 mg/Kg)	3	566	235	333	288	1425	31.6
2. Satisfactory (80-180 mg/Kg)	39	805	633	836	481	2794	62.0
3. Adequate (>180 mg/Kg)	2	87	76	79	41	285	6.3

(Tripathi *et al*., 2000). The presence of vast eroded lands might be one of the main reasons of low organic matter contents in soils.

***Available phosphorus*.** The data revealed that 96% soils of Gujar Khan were poor in available phosphorus (AP). About 3.4% soils was satisfactory and only 0.6% was adequated (> 14 mg/Kg) AP contents (Table 3). The frequency distribution analysis indicated that majority of soils (57%) in Gujar Khan area has AP in the range of 4.0-6.0 mg/Kg (Table 5), followed by 34% in 2.1-4.0 mg/Kg, whereas only 0.6% samples has >14 mg/Kg AP contents. Shaheen (2016) reported phosphorus deficiency (< 7 mg/Kg) in 95% soils of Gujar Khan. Similar results were reported by Khalid *et al*. (2012) for Chakwal soil of Pothwar areas. Malik *et al*. (1984b) and Rashid (1994) reported a wide spread phosphorus deficiency in Punjab and reported 75-95% soils are lacking this major nutrient. Kumar *et al*. (2017) described medium to low available P contents in Rajistan, India soils and low mobility of this nutrient in soil.

In soils with pH 7-8, the soluble H_2PO_4 quickly reacts with calcium to form products of having less solubility. The pH also affects the applied P fertilizer by changing it into extremely insoluble calcium phosphate form. This problem is common in calcareous soils (Ali *et al*., 2000). The poor AP status of Gujar Khan soils might be attributed to this phenomenon.

***Available potash*.** The satisfactory level of available potassium (AK) contents was observed in the study area ranging from 40-320 mg/Kg with mean value of 103 mg/Kg (Tables 2). As many as 62% soils contained satisfactory, 6.3% which has adequate and 31.6% of poor (<80 mg/Kg) AK contents. The frequency distribution data (Table 6) indicated that 50% soil was AK ranged from 81-120 followed by 30% in 40-80 mg/Kg ranged. Soils of Pakistan are generally considered rich in mica minerals, the rich source of natural potassium (Khattak and Hussain, 2007; Bajwa and Rehman, 1996). Similarly the high to medium range of available K in Rajistan soils of India was attributed by Kumar *et al*. (2017) to the presence of potash bearing minerals (Muscovites, biotits and feldspar) which on weathering slowly release potash. Available potash was invariably reported as adequate in Punjab soils except eroded or light texture soils (Khalid *et al*., 2002; Bajwa, 1990).

Table 4. Frequency distribution of Gujar Khan area soil samples for organic matter

Organic matter range (%)	2012-13	2013-14	2014-15	2015-16	2016-17	Total	(%)
0.0 – 0.20	0	195	89	13	76	373	8.3
0.21 – 0.40	32	456	214	369	432	1503	33.4
0.41 – 0.60	8	670	625	530	213	2046	45.4
0.61 – 0.80	0	50	7	301	76	434	9.6
0.81 – 1.00	3	59	6	18	8	94	2.1
1.01 – 1.20	0	21	3	17	2	43	1.0
1.21 – 1.40	1	7		0	3	11	0.2
> 1.40	0	0	0	0.	0	0	0.0

Table 5. Frequency distribution of Gujar Khan area soil samples for Av. phosphorus

Available P range (mg/Kg)	2012-13	2013-14	2014-15	2015-16	2016-17	Total	(%)
0-2.0	0	0	0	9	11	20	0.4
2.1-4.0	30	1021	132	192	165	1540	34.2
4.0-6.0	7	386	663	965	553	2574	57.1
6.1-8.0	0	32	127	30	38	227	5.0
8.1-10.0	2	12	2	14	5	35	0.8
10.1-12.0	4	4	12	32	23	75	1.7
12.1-14.0	0	0	2	0	3	5	0.1
>14.0	1	3	5	6	12	27	0.6

Table 6. Frequency distribution of Gujar Khan area soil samples for Av. potash

Available K range (mg/Kg)	2012-13	2013-14	2014-15	2015-16	2016-17	Total	(%)
0-40	0	34	0	21	13	68	1.5
41-80	3	532	235	312	265	1347	29.9
81-120	29	623	526	705	389	2272	50.4
121-160	10	182	106	131	102	531	11.8
161-220	2	65	59	63	34	223	5.0
221-260	0	22	14	11	7	54	1.2
260-300	0	0	3	5		8	0.2
>300	0	0	0	0	0	0	0.0

Table 7. Soil fertility index of soils in Gujar Khan area

Available nutrients	Poor	Satisfactory	Adequate	Soil nutrient index (SNI)
	(%)			
Organic matter/ nitrogen	96.7	3.0	0.3	1.04
Available phosphorus	96.0	3.4	0.6	1.04
Available potassium	31.6	62.0	6.3	1.74

However, Rashid (1994) reported 30% of surface soils in groundnut growing areas of Gujar Khan contained low AK-22-158 mg/Kg.

Soil fertility index (SFI). Soil fertility index at nutrient index value of >2.5 is taken as higher, while values between 1.5-2.5 indicates medium and < 1.5 as low fertility status of the given area (Motsara, 2002). The fertility index values of Gujar Khan soils (Table 7) in respect of OM & AP are low (1.04), whereas of AK (1.74) indicating a medium fertility status. Similar results are reported by Kausar *et al*., (2016) for Sargodah soils and Khalid *et al*. (2012) for Chakwal area of Pothwar. While, medium nutrient index values for organic carbon (2.3), available phosphorus (2.2) and high for potassium (3.0) are observed by Singh *et al*. (2018) in the soils of Varanasi district, UP, India.

Conflict of Interest. The authors declare no conflict of interest.

Refrences

Ahmed, N., Rashid, M. 2003. *Fertilizer use in Pakistan*. NFDC. Planning and development division, Islamabad, 141 pp.

Ali, M., Sarir, M.S., Shirazi, M.U., Alam, S.M., Ansari, R. 2000. Phosphorus mineralization in some soil series of Peshawar valley. *Journal of Soil Science*. **18:** 13-18.

Atreya, K., Sharma, S., Bajracharya, R.M. 2005. Minimization of soil and nutrient losses in maize-based cropping systems in the mid-hills of central Nepal. Kathmandu University. *Journal of Science, Engineering and Technology*, **1:** 1-10.

Bajwa, M.1. 1990. Soil fertility management for sustainable agriculture. In: *Proceeding 3rd National Congress of Soil Science*, March 20-22, pp. 7-23, Lahore, Pakistan.

Bajwa, M.I., Rehman, F. 1996. Soil and fertilizer potassium. In: *Soil Science*, Rashid, A. and Memon, K.S. (Managing Authors), pp. 317-338, National Book Foundation Islamabad, Pakistan.

Cooke, G.W. 1982. An introduction to soil analysis. *World Crops*, **1:** 8-9.

Fateh, S., Arshad, M., Neem, M.A., Latif, I. 2006. Physioco-chemical characteristics of soil of Pothwar and determination of organic matter. *Pakistan Journal of Biological Sciences*, **9:** 473-476.

Soo Ying Ho, Wasli, M.E.B., Perumal, M. 2019. Evaluation of physic-ochemical properties of sandy-textured soils under small holder agricultural land use practices in Sarawak, east Malaysia. *Applied and Environmental Soil Science*, *ID-768545*, (14 pages).

Khalid, R., Kashif, S.R., Naz, S.Y. 2002. Potassium status of Gujar Khan soils. *Pakistan Journal of Soil Science*, **21:** 41-44.

Khan, K.S., Joergensen, R.G. 2006. Microbial C, N and P relationships in moisture stressed soils of Potohar, Pakistan. *Journal of Plant Nutrition and Soil Science*, **169:** 494-500.

Khalid, R., Mahmood, T., Bibi, R., Siddique, M.T. 2012. Distribution and indexation of plant available nutrients of rainfed calcareous soils of Pakistan. *Soil and Environment*, **31:** 146-151.

Kausar, R., Azam, M., Nawaz, S., Ahmad, I., Iqbal, N. 2016. Indexing soil fertility status and suitability of groundwater in Sargodah district. *Journal of Environment and Agriculture*, **1:** 12-21.

Khattak, R.A., Hussain, Z. 2007. Evaluation of soil fertility status and nutrition of orchards. *Soil and Environment*, **26:** 22-32.

Kumar, D., Yadav, S.R., Kaur, R., Choudhary, A., Meena, B.J.S. 2017. Soil fertility status and nutrient recommendations based on soil analysis of Jaisalmer district of western Rajasthan. *Asian Journal of Soil Science*, **12:** 103-107

Mahmood, S., Qazi, M.A., Ali, I. 2010. *Annual Report 2008-09. Soil and Water Advisory Service in Punjab*. Soil Fertility Research Institute, Department of Agriculture, Lahore, Pakistan.

Malik, D.M., Khan, M.A., Choudhry, T.A. 1984a. *Analysis Manual for Soil, Water and Plants*. Directorate of Soil Fertility and Soil Testing, Lahore, Pakistan.

Malik, D.M., Ahmed, B., Ahmed, M. 1984b. *Survey of Soil Fertility Status and Quality of Ground Waters*. Punjab Digest 1981-84 Lahore, Department of Agriculture, Punjab.

Motsara, M.R. 2002. Available nitrogen, phosphorus and potassium status of Indian soils as deicited by soil fertility maps. *Fertilizer News*, **47:** 15-21.

Nizami, M.I., Shafiq, M., Rashid, A., Aslam, A. 2004. *The Soils and Their Agricultural Development Potential in Pothwar.* WRRI & NARC, Islamabad, Pakistan. pp. 5-7.

Page, A.L. 1982. *Method of Soil Analysis, Part 2, Chemical and Microbiological Properties*, 2nd edition, American Society of Agronomy, Inc and Soil Science Society of America, Inc., Publisher, Madison, Wisconsin, USA.

Parkar, 1951. *Agronomy Journal*, **48:** 105-112.

Rashid, A. 1994. *Nutrient Indexing Surveys and Micronutrient Requirement of Crops*. NARC, Islamabad, Pakistan.

Rashid, A., Rafique, E., Bughio, N. 1997. Micronutrient deficiencies in rainfed calcareous soils of Pakistan. I. Iron chloresis in peanut. *Communication in Soil Science and Plant Analysis*, **28:** 135-148.

Sarwari, G., Hussain, N., Schmeisky, H., Suhammad, S., Ibrahim, M., Ahmad, S. 2008. Efficiency of various organic residues for enhancing rice-wheat production under normal soil conditions. *Pakistan Journal of Botany*, **40:** 2107-2113.

Shaheen, A. 2016. Characterization of eroded lands of Pothwar plateau, Punjab, Pakistan. *Sarhad Journal of Agriculture*, **32:** 192-201.

Singh, S.P., Singh, S., Kumar, A., Kumar, R. 2018. Soil fertility evaluation for macronutrients using parkers nutrient index approach in some soils of varanasi district of eastern Utter Pradesh, India. *International Journal of Pure and Applied Bioscience*, **6:** 542-548.

Tsozue, B.P., Shrestha, S.P., Tamfuh, P.A. 2016. Relationship between soil characteristics and fertility implications in two typical dystrandept soils of the Cameroon western highland. *International Journal of Soil Science*, **11:** 36-48.

Tripathi, B.P., Shrestha, S.P., Acharya, G.P. 2000. *Summary and Updating with 1999 Season Soil and Nutrient Losses from Bari Land Terraces in the Western Hills of Nepal*. Lumle technical paper No. 2000/2003. Lumle Agricultural Center, Kaski, Nepal.

Pak. j. sci. ind. res. Ser. A: phys. sci. 2021 **64A**(1) 52-58

Sunspots Influence on Climatic Variability of Karachi and Rohri

Kanwal Aftab and Saifuddin Ahmed Jilani*
Institute of Space and Planetary Astrophysics, University of Karachi, Karachi-75270, Pakistan
Department of Physics, University of Karachi, Karachi-75270, Pakistan

(received February 25, 2019, revised January 12, 2020; accepted January 15, 2020)

Abstract. The Sun is undoubtedly the most important thrust of the climate system. However, only little is known how variable this force is acting on different time scales ranging from minutes to millennia and how the climate system reacts to changes in this forcing. In the present study possible effect of solar activity on maximum temperature T (max) and minimum temperature T (min), humidity and precipitation have been investigated. The analysis comprises over a period of 2000-2015 that consists of the decreasing phase of solar cycle-23 and the increasing phase of solar cycle-24. To optimize the number of signicant trends, different phases of solar activity have been implemented there to observe the variation in climate of Karachi and Rohri in response of it. These detection and adjustment are carried out using the computer software Statistica and Minitab. Correlation analysis for different seasons of these two regions is performed in this study.

Keywords: sunspots, precipitation, humidity, temperature, solar cycle

Introduction

Change in climate is most evident from increase in temperature on the surface of the earth. For the period since 1976, the rate of change is roughly 3 times that for the past 100 years as a whole. There has been a small positive trend in global precipitation of about 1% during the 20th century over land (Houghton *et al*., 2001). Global warming is often confused with climate change by laymen electronic media print media and to the general public, news media and policy makers. Climate change is often synonymous with global warming, but this generally used term is quite wide in its real sense. It is not only characterised by changes in temperature and also by changes in other variables of the climate system for instance precipitation.

Climate of earth is most certainly affected by several natural phenomenons such as atmospheric composition, solar energy flux, albedo and anthropogenic (e.g. atmospheric pollution) factors. However, there are also slight natural phenomena which can have a significant impact on the climate. One of such phenomena is solar activity. In the current epoch, solar variation impacts on regional climate appear to be quite significant. For example, Europe in winter but on a global scale are likely to be much smaller than those due to increasing greenhouse gases (Elizbarashvili *et al*., 2013; Le Mouël *et al*., 2009).

*Author for correspondence;
E-mail: sajilani@uok.edu.pk

Environmentalists has been concerned about alteration in physical parameters like temperature and precipitation and a number of studies on these changes have already been made for different regions of the country in past (Keggenghoff *et al*., 2015; Six months into floods, 2011; TFCC, 2010). The Sindh province of Pakistan is lack in such research studies. One of the reason may be less access to the climate related data and some time because of the unpublished research studies. Sindh region has limited resources for different low-lying islands and is exposed to tropical cyclones, thus it is more susceptible to climatic changes. If reported climate change occurs and have adverse affect on eco-system and on human beings. The maximum temperature, heat waves and heavy rain expected to be increased (Easterling *et al*., 2000). These occasions, along side rising ocean levels, will compound surges and disintegration, debilitating essential foundation and water quality (Sheikh *et al*., 2014; Rasul *et al*., 2012; Wang and Zhao, 2012). The current data contrasted with the past changes in the mean atmosphere and so far is less thought about late changes in atmosphere extremes. There is a pressing need to nearly screen recent climatic variety in the locale and some arrangement making to secure assets for long haul use.

Study area. The region under investigation is situated in Sindh and the second biggest territory of the nation with an aggregate land region of 14.09 million hectares constituting 17.7 % of the Nation's Topographical Zone with a width of 4 to 6 km and length is too long around

855 kilometers. It begins shape Guddu barrage to Arabian sea (Abbasi, 2011).

Karachi. Karachi with its longitude and latitude 24.8607° N, 67.0011° E, has seared atmosphere, in spite of the fact that a direct form of this atmosphere. Karachi is situated on the drift and subsequently has a moderately tranquil atmosphere. Karachi has two principle seasons i.e. summer and winter, while spring and pre-winter are short. Summer season holds on for longest period amid the year. The level of precipitation is low for a large portion of the year. Less precipitation amid summer is because of reversal layer. The rain storm in the Karachi likewise downpours from July to September. The city appreciates a tropical atmosphere enveloping mellow winters and warm summers. The moistness levels generally stay high from March to November, while low in winter as the breeze bearing in winter is north Easterly. Since summer temperatures (from the end of April till the end of August) are around 30 °C or 86 °F to 36 °C or 97 °F, the winter months (from November till the end of March) are the best time to visit Karachi. Most guests, travelers come to Karachi amid the long stretch of December (WMO Climate Normals for Karachi 1961-1990).

Rohri. Rohri has 27.6752° N, 68.9003° E and also has sweltering desert atmosphere with a great degree sweltering summers and gentle winters. It is extremely dry with the little rain and gets generally falling in the rain storm season from July to September (Nadiem, 2004).

Materials and Methods

Data analysis. The specified data was used to analyze local climate:

- Means of monthly T (max) and T (min), humidity and precipitation have been obtain by the meteorological department of Sindh (observation period from 2000-2015).
- The variations of the Sun Spot Numbers (SSN) are analyzed by using monthly average Sun Spot Numbers from 2000-2015, taken by https://blog.quandl.com/category/free-data-on-quandl.
- Smooth Sun Spot Number from 2000-2015 taken from www.sws.bom.gov.au/solar/1/6

The climatic variables of T (max), T (min), humidity and precipitation for different months were analyzed separately during the solar period 2000-2015 and then for solar minima (2008), solar maxima (2001) the equinoxes (March and September) and solstices (June and December) of each year and the Sun's decreasing phase (2000-2008) and increasing phase (2009-2015). Both smooth and non-smooth series of SSN were use to examine solar climatic relation.

The significant correlation coefficients have been estimated in response of their P-values. The P-value less than 0.05 with respect to 95% confidence interval indicate the significant correlation.

The correlation coefficients between the climatic variables and SSN with their P-values are indicated in Table 1-4.

Result and Discussions

The correlation analysis for the monthly data gives us some significant relation between solar and the atmospheric variables. The significant results of correlation are obtained for humidity and precipitation during winter season at Rohri region with non-smooth series of SSN where, both these two climatic variable found negatively correlated. Again with non-smooth series of SSN significant correlation exist for T (max) and humidity in summer season at Karachi region, where T (max) is negatively correlated and humidity is positively correlated. This observation is not unexpected. It is in accordance with the already reported results by (Le Mouël *et al*., 2009). From Tables 1-4 have been observed that high correlation exist between climatic variables and smooth series of SSN rather than non-smooth series. The correlation between humidity and SSN (both for smooth and non-smooth series) are found significant at Rohri region during decreasing phase, winter season and for the period 2000-2015 whereas, precipitation have significant correlation with smooth series of SSN for Karachi region during the period 2000-2015. However, humidity found more strongly correlated with smooth series of SSN during winter for Karachi and while, for Rohri region the humidity and rain both are strongly correlated during winter and decreasing phase of both for smooth and non-smooth series of SSN.

Maximum temperature T (max) during summer for Karachi region found correlated with SSN while, using non smooth series this correlation disappears by using smooth series. It indicates that the solar activity is not only a possible parameter for the climatic variations but it can be a participant or the internal atmospheric processes effect or facade the solar effect. By utilizing

Table 1. Correlaton coefficients and P-level values between non-smooth SSN and climatic parameters for Karachi

For Karachi					
Non-smooth SSN Vs Climatic parameters					
		T (max)	T (min)	Humidity	Rain
Maxima	r	0.325	0.2	0.101	-0.351
	p	0.303	0.534	0.755	0.234
Minima	r	0.234	-0.151	-0.434	-0.581
	p	0.464	0.64	0.159	0.078
Solstices	r	0.072	0.047	0.028	-0.333
	p	0.697	0.799	0.879	0.103
Equinox	r	-0.204	-0.078	-0.09	0.024
	p	0.263	0.67	0.626	0.913
Decreasing	r	0.039	0.041	-0.003	-0.138
phase	p	0.69	0.674	0.975	0.187
Increasing	r	-0.043	-0.016	-0.048	-0.101
phase	p	0.698	0.882	0.665	0.4
Winter	r	0.144	-0.066	-0.285	-0.305
	p	0.334	0.657	0.052	0.05
Spring	r	-0.045	-0.307	-0.078	-0.068
	p	0.762	0.8	0.597	0.662
Summer	r	-0.247	-0.191	0.486	0.259
	p	0.049	0.131	0	0.067
Autumn	r	0.024	0.024	-0.035	-0.001
	p	0.897	0.897	0.851	0.996
2000-2015	r	0.008	0.020	-0.019	0.125
	p	0.909	0.782	0.795	0.109

Table 2. Correlaton coefficients and P-level values between non-smooth SSN and climatic parameters for Rohri

For Rohri					
Non-smooth SSN Vs Climatic parameters					
		T (max)	T (min)	Humidity	Rain
Maxima	r	0.112	0.126	0.174	-0.25
	p	0.728	0.695	0.589	0.516
Minima	r	0.044	-0.153	-0.541	-0.405
	p	0.891	0.634	0.069	0.245
Solstices	r	0.055	-0.004	-0.241	-0.373
	p	0.77	0.982	0.191	0.05
Equinox	r	0.034	-0.078	-0.337	0.001
	p	0.856	0.676	0.064	0.995
Decreasing	r	0.099	0.034	-0.249	-0.183
phase	p	0.309	0.725	0.009	0.071
Increasing	r	-0.041	-0.02	0.073	0.032
phase	p	0.721	0.857	0.512	0.777
Winter	r	0.119	-0.081	-0.381	-0.347
	p	0.426	0.588	0.008	0.023
Spring	r	0.089	0.026	-0.204	-0.078
	p	0.547	0.859	0.164	0.605
Summer	r	0.046	-0.235	-0.155	-0.057
	p	0.723	0.063	0.22	0.666
Autumn	r	-0.04	0.008	-0.021	0.001
	p	0.832	0.965	0.91	0.998
2000-2015	r	0.061	0.009	-0.178	-0.084
	p	0.403	0.906	0.014	0.262

Table 3. Correlaton coefficients and P-level values between smooth-SSN and climatic parameters for Karachi

For Karachi					
Smooth SSN Vs Climatic parameters					
		T (max)	T (min)	Humidity	Rain
Maxima	r	0.301	0.308	0.341	0.211
	p	0.341	0.33	0.278	0.534
Minima	r	-0.3	-0.21	-0.181	-0.165
	p	0.343	0.512	0.573	0.648
Solstices	r	0.092	0.06	0.021	-0.37
	p	0.615	0.745	0.907	0.068
Equinox	r	-0.259	-0.135	-0.156	-0.094
	p	0.152	0.461	0.394	0.669
Decreasing	r	-0.007	-0.021	-0.068	-0.164
phase	p	0.944	0.827	0.483	0.117
Increasing	r	-0.063	-0.014	-0.047	-0.164
phase	p	0.566	0.903	0.67	0.168
Winter	r	0.144	-0.018	-0.3	-0.252
	p	0.334	0.906	0.04	0.107
Spring	r	-0.067	-0.053	-0.091	-0.091
	p	0.65	0.719	0.539	0.556
Summer	r	-0.241	-0.188	0.45	0.214
	p	0.055	0.138	0.00	0.132
Autumn	r	0.05	0.04	-0.078	-0.061
	p	0.788	0.829	0.67	0.751
2000-2015	r	-0.027	-0.019	-0.062	-0.160
	p	0.707	0.793	0.390	0.040

Table 4. Correlaton coefficients and P-level values between smoothed SSN and climatic parameters for Rohri

For Rohri					
Smooth SSN Vs Climatic parameters					
		T (max)	T (min)	Humidity	Rain
Maxima	R	0.192	0.299	0.68	-0.176
	P	0.55	0.346	0.015	0.65
Minima	R	-0.058	-0.149	-0.494	-0.375
	P	0.858	0.645	0.102	0.285
Solstices	R	0.075	0.014	0.271	-0.371
	P	0.014	0.941	0.14	0.052
Equinox	R	0.022	-0.11	-0.395	-0.03
	P	0.907	0.556	0.028	0.875
Decreasing	R	0.039	-0.03	-0.263	-0.204
phase	P	0.686	0.756	0.006	0.043
Increasing	R	-0.005	0.009	0.024	0.042
phase	P	0.965	0.939	0.832	0.712
Winter	R	0.184	-0.043	-0.452	-0.334
	P	0.215	0.774	0.001	0.029
Spring	R	0.085	0.021	-0.212	-0.069
	P	0.567	0.886	0.148	0.647
Summer	R	0.057	-0.219	-0.171	-0.069
	P	0.658	0.085	0.176	0.605
Autumn	R	0.001	0.009	-0.132	-0.049
	P	0.995	0.961	0.486	0.804
2000-2015	R	0.024	-0.032	-0.190	-0.094
	P	0.746	0.658	0.008	0.209

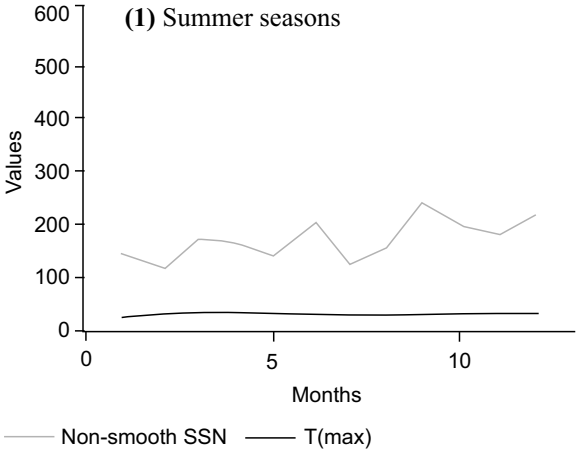

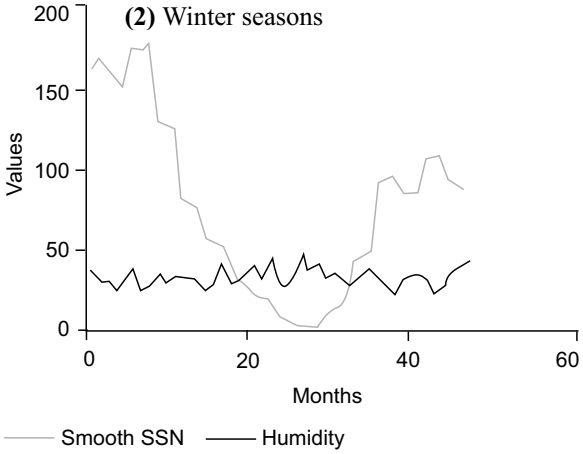

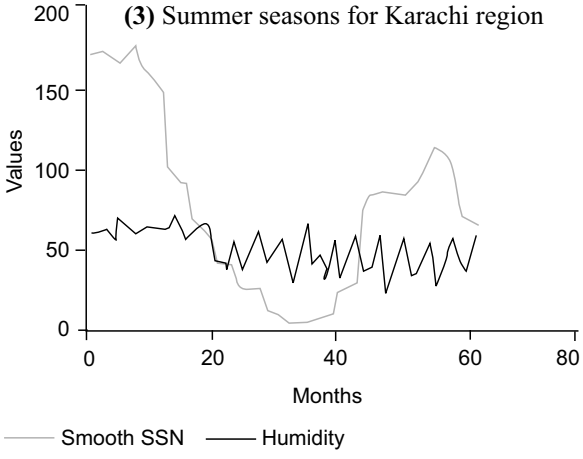

Fig. 1-3. Shows the correlation between the solar variable SSN both for smooth and non-smooth series and four climatic variables for different phases of Sun at Karachi region.

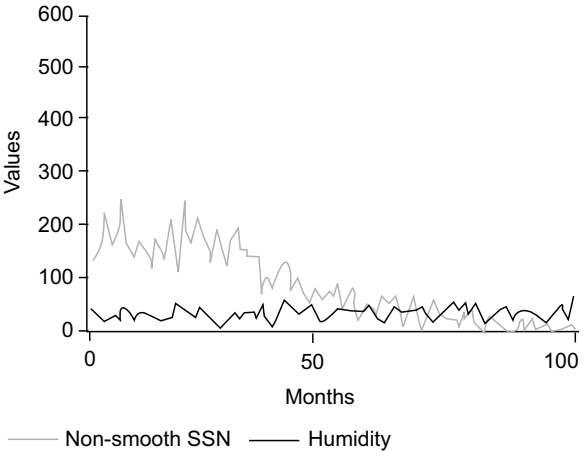

Fig. 4. Decreasing phase of Sun in Rohri region.

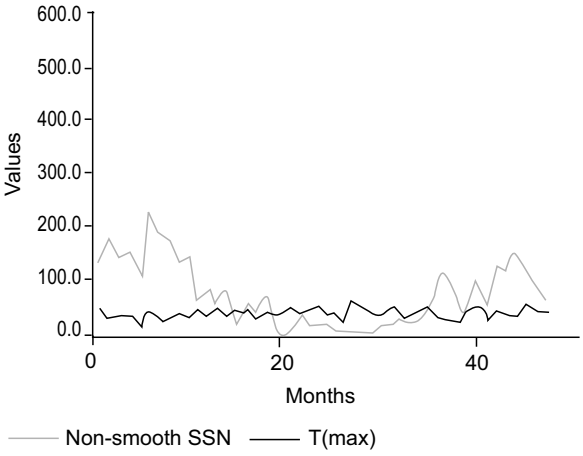

Fig. 5. Winter seasons in Rohri region.

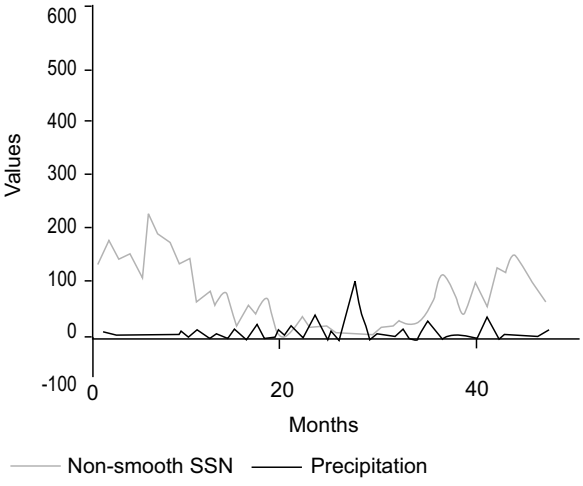

Fig. 6. Winter seasons in Rohri region.

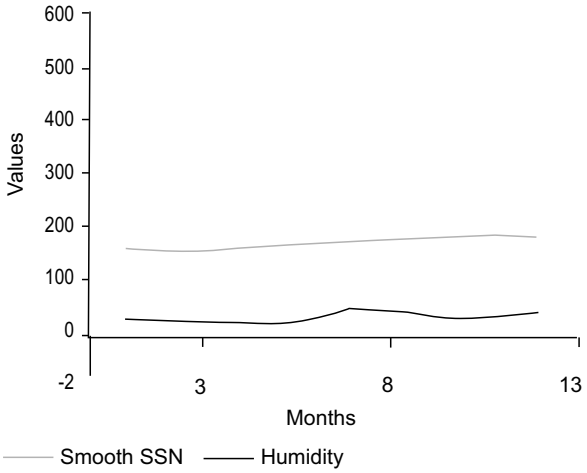

Fig. 7. Sunspot maxima in Rohri region.

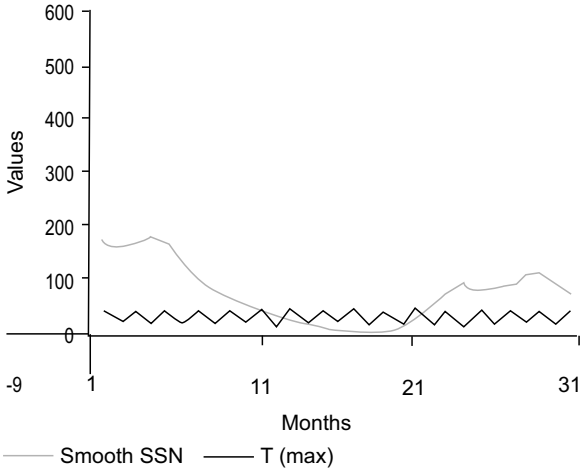

Fig. 8. Sun at solstices in Rohri region.

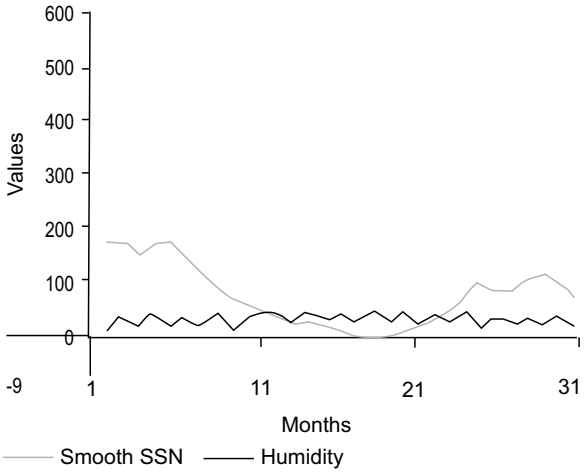

Fig. 9. Sun at equinox in Rohri region.

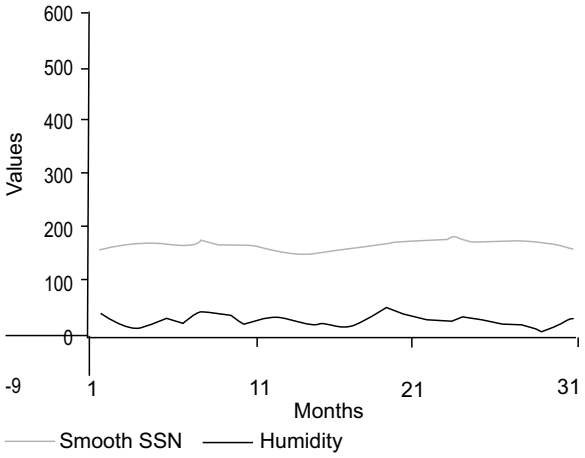

Fig. 10. Decreasing phase of Sun in smooth series in Rohri region.

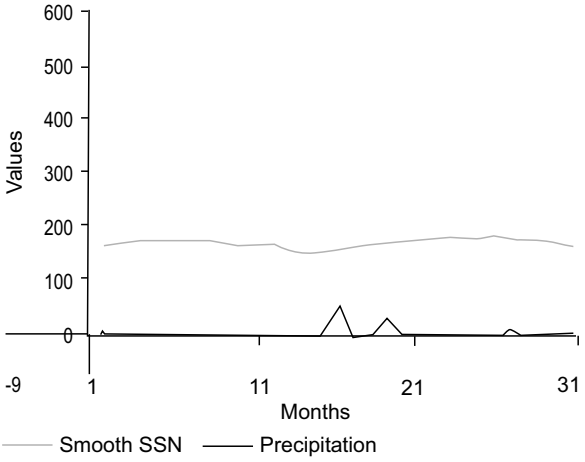

Fig. 11. Decreasing phase of Sun in smooth series in Rohri region.

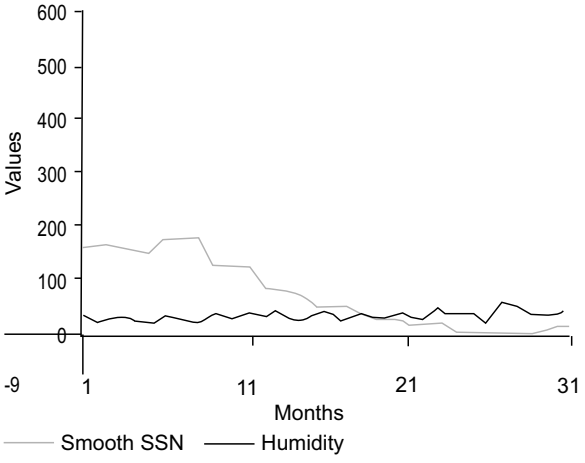

Fig. 12. Winter seasons in smooth SSN humidity in Rohri region.

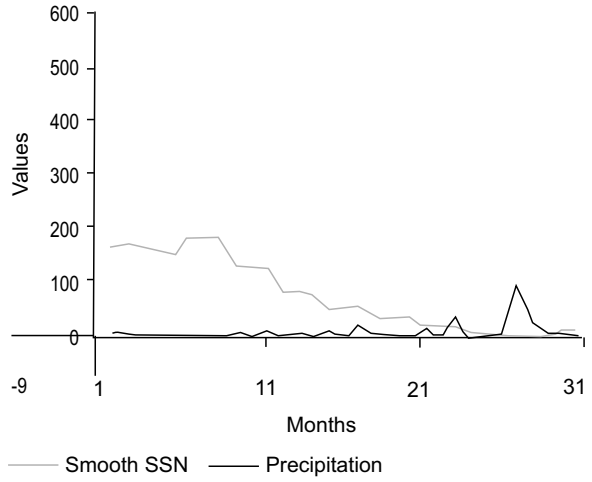

Fig. 13. Winter seasons in smooth SSN precipitations.

Figs. 4-13. Shows the correlation between the solar variable SSN both for smooth and non-smooth series and four climatic variables for different phases of Sun at Rohri region.

smooth series of SSN, the correlation turn out to be more associated with the climatic variables. The smooth SSN causes an expansion of the connection of the information. Therefore, if the smooth data series are subjected to authentic inspection, the signification of the measurable parameters must be computed by utilizing example sizes rather than the real sizes.

Conclusion

The correlation between the climatic variables with smooth & non-smooth series of SSN has been established in this study. This analysis defines that there is no significant correlation of T (min) with both smooth and non-smooth series of SSN in all phases of Sun for both Karachi and Rohri regions. Therefore, provides evidence for comparison of reliability between T (min) and T (max) in response of solar activity variable SSN.

In this study we measure the humidity variables and found mainly dependent on SSN. It is negatively correlated with SSN except at Rohri region during maxima for smooth series and at Karachi region during summer season for non-smooth series and it is found positively correlated. Albeit, SSN was not only the reason for climate change but it may be one of the factor for future climatic variability. In Rohri region there is more influence of SSN on humidity in comparison of Karachi region. In winter season Rohri region also found negatively correlated with Rain for both smooth and non-smooth series of SSN. Therefore, it conclude that climate of Karachi is not mainly depend on SSN activities, it may be because of the coastal area.

It has further been concluded that:

- Significant correlation is found between SSN and humidity, which further improved in case of smooth series of SSN.
- For T (max), T (min) and precipitation the correlation with SSN are relatively less significant.

Acknowledgment

Authors are thankful to the Metrological Department of Sindh and for data acquisition.

References

Abbasi, A.A. 2011. Team management: The Islamic Paradizm. *African Journal of Business Management*, **5:** 1975-1982.

Easterling, D.R., Meehl, G.A., Parmesan, C., Changnon, S.A., Karl, T.R., Mearns, L.O. 2000. Climate extremes: observations. *Modeling and Impacts Science*, **289:** 2068.

Elizbarashvili, E.S., Tatishvili, M.R., Elizbarashvili, M.E., Meskhiya. 2013. Air temperature trends in Georgia under global warming conditions. *Russian Meteorology and Hydrology*, **38:** 234-238.

Houghton, J.T., Ding, Y.H., Griggs, D.J., Noguer, M. 2001. Climate change 2001, *The Scientific Basis*. *The Intergovernmental Panel on Climate Change*, 881 pp.

Keggenhoff, A.N., Elizbarashvili, M., King, L. 2015. Recent changes in Georgia's temperature means and extremes: Annual and seasonal trends between 1961 and 2010. *Weather and Climate Extremes*, **8:** 34-45.

Le-Mouël, J.L., Blanter, E., Shnirman, M., Courtillot, V. 2009. Evidence for solar forcing in variability of temperatures and pressures in Europe. *Journal of Atmospheric and Solar Terrestrial Physics*, **71:** 1309-1321.

Nadiem, I.H. 2004. *Forts of Pakistan*. Al-Faisal Publishers, 54, Lahore, Pakistan.

Planning Commission Government of Pakistan. 2010. *Task Force on Climate Change (TFCC) Recommends Various Adaptations, Mitigation Measures*.

Rasul, G., Mahmood, A., Sadiq, A. 2012. Vulnerability of the Indus delta to climate change in Pakistan. *Pakistan Journal of Meteorology*, **8:** 89-107.

Sattar, A.A., Hameed, I., Bibi, A. 2011. Team management: the islamic paradigm. *African Journal of Business Management*, **5:** 1975-1982.

Sheikh, M.M., Manzoor, N., Ashraf, J., Adnan, M., Collins, D., Hameed, S., Manton, M.J., Ahmed, A. U., Baidya, S.K., Borgaonkar, H.P., Islam, N., Jayasinghearachchi, D., Kothawale, D.R., Premalal, K.H.M.S., Revadekar, J.V., Shrestha, M.L. 2014. Trends in extreme daily rainfall and temperature indices over South Asia. *International Journal of Climatology*, **35:** 1625-1637.

Six months into the floods resetting Pakistan's priorities through reconstruction. 2011. *144 Oxfam Briefing Paper, Oxfam Report on Climate Change*.

Wang, J.S., Zhao, L. 2012. Statistical tests for a correlation between decadal variation in June precipitation in China and sunspot number. *Journal of Geophysical Research*, **117:** 1-10.

WMO. 1961–1990. *Climate Normals for Karachi*, *Airport*. National Oceanic and Atmospheric Administration. Retrieved-03-15.

Pak. j. sci. ind. res. Ser. A: phys. sci. 2021 **64A**(1) 59-64

Source Rock Potential of Chichali and Samana Suk Formations Deposits in Panjpir Oilfield Subsurface, Punjab Platform, Pakistan

Syed Bilawal Ali Shah[a]*, Syed Haider Ali Shah[b], Adeeb Ahmed[c] and Muhammad Nofal Munir[c]

[a]Department of Geology, University of Malaya, Kuala Lumpur, 50603, Malaysia
[b]Department of Management Sciences, Bahria University Islamabad, 44000, Pakistan
[c]Department of Earth and Environmental Sciences, Bahria University Islamabad, 44000, Pakistan

(received April 3, 2019; revised January 8, 2020; accepted January 9, 2020)

Abstract. By using total organic carbon (TOC) and Rock-Eval pyrolysis analysis measurements, the hydrocarbon source rock potential of Chichali and Samana Suk formations found in the subsurface of Panjpir oilfield in Punjab platform located in the eastern part of the middle Indus Basin was investigated. Twenty two core samples were collected from producing well. The analysed samples of Chichali formation contains TOC ranging between 0.99-4.61 wt.% having average TOC of 1.51 wt.% and the S2 values of Rock-Eval show the poor to fair generative potential with values ranging from 0.99-3.08 mg HC/g rock. The samples have low hydrogen index values ranging from 21-302 mg HC/g TOC and also most of the samples have low T_(max) values ranging from 422-432 °C and have OI values ranging from 15-82 mg CO_2/g TOC. Samana Suk formation samples have TOC ranging between 0.28-1.38 wt.% having average TOC of 0.84 wt.%. S2 values of Rock-Eval shows poor generative potential with values ranging from 0.05-2.99 mg HC/g rock. The samples have low hydrogen index values ranging from 13-322 mg HC/g TOC and T_(max) values ranging from 423-435 °C, and have OI values ranging from 41-182 mg CO_2/g TOC. On the basis of analysis performed only one sample from Chichali and five samples of Samana Suk formations have entered early maturity zone, while all remaining samples lie in immature zone as indicated by HI vs T_(max) plot. HI vs OI plot and HI vs T_ (max) indicates the presence of kerogen Type III. All of the samples from Samana Suk formation shows poor generative potential as compared to Chichali formation having fair generative potential as indicated by S2 *vs* TOC plot. Hence, from the results some minor gas could be expected to have been generated from Chichali formation in Panjpir oilfield subsurface.

Keywords: Punjab platform, TOC, thermal maturity, rock-eval, organic matter

Introduction

The Punjab platform is covered monocline dipping westward and is located in the middle Indus basin. The Sulaiman fold belt, Sulaiman depression and Punjab platform were split into three units in the middle Indus basin (Shah and Ahmed, 2018; Shah and Abdullah, 2016; Fazeelat *et al*., 2010; Raza *et al*., 2008). In middle Indus basin Punjab platform is the least succssful part and is dipping gently towards Sulaiman depression. The Punjab platform is bounded by Sargodha high by its north, Mari high from its south, from west Punjab platform merges into Sulaiman depression and in east it extends into Bikaner-Nagaur of India (Shah *et al*., 2018; Raza *et al*., 2008; Kadri, 1995). In this region various potential source rocks have been identified and gas was produced from those recognised source rock with kerogen Type II and III (Shah and Abdullah, 2017; Wandrey *et al*., 2004).

*Author for correspondence;
E-mail: bilawalshah22@yahoo.com

In the region three gas fields have been explored in the infra Cambrian sediments in the region having TOC up to 30% and ranging from 0.80-4% wt. %, (Raza *et al*., 2008; Hasany *et al*., 2007; Peters *et al*., 1995).

Numerous formations in Punjab platform have the potential to produce hydrocarbons and acts as source rock (Shah and Ahmed, 2018; Fazeelat *et al*., 2010) *i.e*. Shinwari formation shales, Samana Suk limestone and Chichali formation of Mesozoic age. All of these have sufficient maturity to generate gas (Shah *et al*., 2019; Asim *et al*., 2014; Kadri, 1995). In this proven hydrocarbons province reservoiur rocks are Samana Suk, Shinwari and Datta formations, with discoveries at Meyal, Panjpir, Nandpur fields, and having seal provided by Ranikot shales (Asim *et al*., 2014).

Panjpir oil field is an important area and is host to proven hydrocarbon reserves but still hydrocarbons have not be explored as expected (Shah *et al*., 2018; Kadri, 1995). In this regards Chichali and Samana Suk

formations which are proven source rocks in other parts of the basin also present in Panjpir oil field have been investigated in this study for hydrocarbons source rock potential. In this study twenty two samples of two formations Chichali and Samana Suk have been investigated to evaluate source rock potentiality.

Geological background. The Indian plate started to rift in Late Proterozoic from supercontinent Gondwana-land (Shah and Abdullah, 2017; Kemal *et al*., 1991; Raza *et al*., 2008), which resulted in sediment deposition of Infra-Cambrian over Pre-Cambrian. Due to the effect of dragging of Infra-Cambrian strata the second phase of rifting in Punjab platform is not evidently observable however, the evidence of rifting can be seen on reflectors of seismic profile, where cretaceous strata have been displaced along normal faults system, along with rifting the Indian plate collision and its subduction underneath the Eurasian plate which is still continuing, have developed variable structural patterns in Punjab platform (Kemal *et al*., 1991). Sedimentary rocks are not exposed on the surface since these are heavily covered by alluvium deposits of sand, clay and silt layers. In terms of petroleum exploration Punjab platform has received much more attention due to discovery of various gases and a recent oil field discovery in nearby field in neighbouring country India on this platform (Shah and Ahmed, 2018).

The study area Panjpir oil field is at lat 30° 41' 2.8104" N 71° long 57' 29.4012" E. The study area has revceived deformation as it lies directly above collusion zone (Eurasian and Indian Plate), where this basin merges into Suliman depression, greater part of the basin northeast is more like Potwar basin as both basins, stratigraphy is matchable, Fig. 1.

From drilling in Punjab platform, the stratigraphic succession has been established which shows mainly marine Palaeozoic-Cenozoic rocks of carbonates and clastic origin, however Punjab platform and Potwar basin stratigraphy of early Triassic age is similar, in southern part stratigraphy of both is very much comparable from Late Triassic and onwards (Shah, 2009; Raza *et al*., 2008).

Material and Methods

From well A in Punjab Platform a total of 22 core cutting samples were obtained at 2-3 m interval, the samples were of Cretaceous and Jurassic age. Samples detailes are available in Appendix 1.

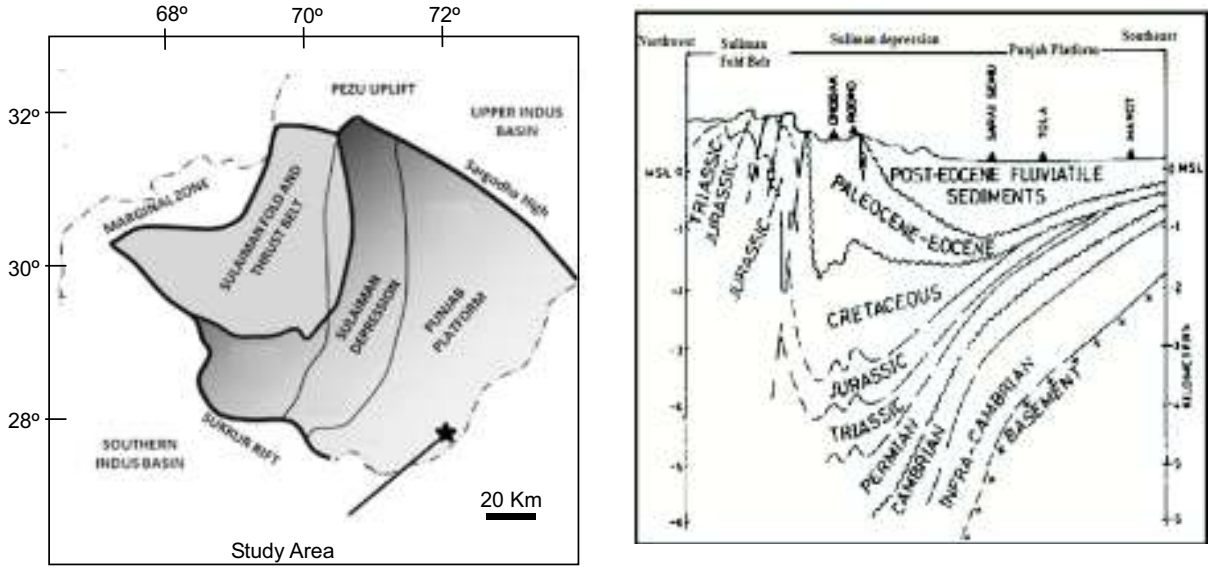

Retroeum Zone:
A1 = Punjab monocline; B3 = East sulaiman deprassion; C1 = Zindapir inner folded zone; C2 = Mart bugti inner folded zone; D1 = Sulaiman outer folded zone

Fig 1. Showing study area Panjpir oil field in the Punjab platform, middle Indus basin (Shah and Abdullah, 2018; modified after Asim *et al*., 2014; Kazmi and Snee, 1989).

Samples were thoroughly washed with water and then dried, crushed and were subjected to passed through 80 m mesh sieve. The crushed samples were subjected to (TOC) total organic carbon analysis, and after TOC analysis the samples were further subjected to Rock-Eval measurements, using Rock-Eval VI apparatus by following (Peters and Cassa, 1994; Peters, 1986). In a helium atmosphere the samples of 100 mg were pyrolysed for 4 min at 300 °C, and followed by scheduled pyrolysis at 25 °C per min from 300-550 °C. The flame ionisation detector (FID) has been used for advance hydrocarbons tracking by (Tissot and Welte, 1984).

During isothermal pyrolysis at 300 °C from volatilization of free hydrocarbons the first peak S1 was obtained. S2 the second peak which represents hydrocarbons generated by thermal cracking of kerogen during pyrolysis at 300-500 °C, and the third peak S3 which represents CO_2 generated from 1 g of rock during pyrolysis were analysed by (TCF) thermal conductivity detector. Following Shah and Ahmed, (2018) and Fazeelat *et al*. (2010) maturity and type of organic matter were interpreted. The TOC measurements of rocks were determined by utilizing Leco CR-12 carbon determinator at (HDIP) Hydrocarbon Development Institute of Pakistan. To remove carbonate the crushed samples of 100 g were treated with 6N HCL and were combusted at 1200 °C in O_2 atmosphere. By (TCD) thermal conductivity detector CO_2 amount were measured.

Results and Discussion

Total organic carbon content and Rock-Eval pyrolysis. Cretaceous age Chichali and Jurassic age Samana Suk formations were assessed for source rock potential at well A in Panjpir oilfield, the calculated values are shown in Table 2.

TOC contents of the analysed samples of Chichali formations are generally in poor to fair potential range, having TOC between 0.99-4.61 wt. %. From pyrolysis measurements the values of S2 of analysed sample are in poor to fair potential ranged from 0.99-3.08 mg HC/g rock. According to the classification by Peters and Cassa (1994) these values are in the normal appropriate values of a source rock to have hydrocarbon generative

Appendix 1.

Depth (m)	Formation	TOC (%)	S1 (mg/g)	S2 (mg/g)	S3 (mg/g)	Tmax (°C)	HI	OI	S2/S3
1675	Chichali	1.2	0.08	0.99	0.51	427	83	43	1.94
1676	Chichali	4.61	0.1	0.99	0.68	427	21	15	1.46
1678	Chichali	1.54	0.1	1.91	0.43	427	124	28	4.44
1679	Chichali	1.57	0.08	2.75	0.57	427	175	36	4.82
1681	Chichali	1.02	0.03	1.27	0.48	427	125	47	2.65
1683	Chichali	1.53	0.03	1.15	0.76	422	75	50	1.51
1685	Chichali	1.42	0.05	1.43	0.68	422	101	48	2.1
1687	Chichali	1.02	0.03	3.08	0.68	426	302	67	4.53
1694	Chichali	1.4	0.03	1.93	0.58	426	138	41	3.33
1697	Chichali	1.34	0.03	1.71	0.68	432	128	51	2.51
1701	Chichali	1.21	0.02	1.97	0.49	428	163	40	4.02
1705	Chichali	1.23	0.02	1.97	1.01	428	160	82	1.95
1708	Chichali	0.99	0.02	1.18	0.45	428	119	45	2.62
1711	Chichali	1.1	0.02	1.13	0.41	428	103	37	2.76
1752	Samana Suk	1.38	0.02	0.23	0.63	428	17	46	0.37
1754	Samana Suk	1.09	0.02	0.69	0.85	423	63	78	0.81
1756	Samana Suk	1.08	0.02	0.14	0.44	423	13	41	0.32
1758	Samana Suk	0.93	0.02	2.99	0.54	434	322	58	5.54
1760	Samana Suk	0.52	0.01	0.15	0.66	433	130	127	0.23
1762	Samana Suk	0.89	0.05	0.14	0.68	434	16	76	0.21
1763	Samana Suk	0.28	0.01	0.05	0.51	435	18	182	0.1
1765	Samana Suk	0.56	0.02	0.35	0.39	433	63	70	0.9

TOC = total organic carbon, wt.% TOC; S1 = volatile hydrocarbon (HC) content, mg HC/g rock; S3 = carbon dioxide yield, mg CO_2/ g rock; HI = hydrogen index = S2 x 100/ TOC, mg HC/g TOC; OI = oxygen index = S3 x 100 / TOC, mg CO_2/g; S2 = remaining HC generative potential, mg HC/g rock; T_{max} = temperature at maximum S2 peak.

potential. These samples have reasonal potential as indicated by S2 vs TOC plot (Fig. 2), whereas only one sample lies in poor range. The samples also have mostly low HI values ranging from 21-302 HC/g TOC, and have OI values ranging from 15-82 mg CO_2/g TOC having kerogen Type III (Fig. 3). of the analysed samples which represent the temperature at the point, where S2 peak is at its maximum have values ranging from 422-432 °C indicating that the samples are immature and lie in immaturity window, with only one sample that has entered early maturity window. For thermal maturity HI *vs* T_{max} were plotted which show that most of the samples lie in immature zone and only one sample shows maturity (Fig. 4). However, Samana Suk formation have poor generative potential having TOC ranging from 0.28-1.38 wt.%, S2 values ranging from 0.05-2.99 mg HC/g rock and low HI values ranging from 13-322 HC/g TOC, indicating that the samples have poor potential to generate hydrocarbons (Fig. 2-4).

The data shows the Samana Suk formation sediments have poor generation potential as compared to Chichali formation sediments which have poor to good generative after the analysis of samples potential. By pyrolysis data, the type of organic matter and the hydrocarbons

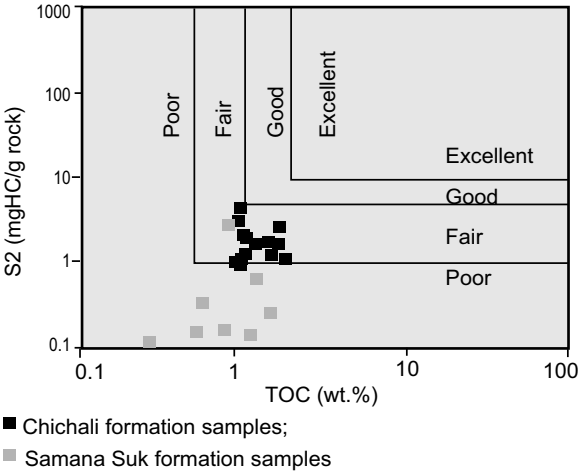

Fig. 2. Pyrolysis S2 versus (TOC) total organic carbon plot displaying source rock generative potential (after Peters and Cassa, 1994).

Table 1. Log based tratigraphy of Panjpir oil fied (developed from well 1)

Age	Formation	Lithology	Top (m)	Bottom (m)
Pliocene	Nagri	Sandstone	0	620
Miocene	Chinji	Sandstone and clay	620	1326
Eocene	Sakesar	Limestone	1326	1326
Early eocene	Nammal	Shale and marl	1326	1360
Early eocene	Ghazij Sui member	Shale	1360	1521
Paleocene	Dunghan	Limestone	1521	1542
Paleocene	Ranikot	Limestone and shale	1542	1602
Cretaceous	Lumshiwal	Sandstone and silt stone	1602	1672
Cretaceous	Chichali	Silt stone and sandstone	1672	1727
Middle jurassic	Samanasuk	Sandstone and limestone	1727	1854
Early jurassic	Shinwari	Sandstone and siltstone	1854	1931
Early jurassic	Datta	Sandstone and shale	1931	1949
Late triassic	Kingriali	Dolomite limestone	1949	2077
Middle triassic	Tredian	Sandstone	2077	2120

Table 2. Measure TOC and Rock-Eval pyrolysis measurements

Formation (no. of samples)	Depth (m)	Hydrocarbon potential			Maturity	OM Quality		Main Kerogen type	Source rock potential
		TOC %	S1	S2	Tmax °C	HI	S2/S3		
Chichali formation (14)	1676-1711	0.99-4.61	0.08-0.10	0.99-3.08	422-432	21-302	1.45-4.82	III	Poor-Fair
Samana Suk (08)	1752-1765	0.28-1.38	0.01-0.05	0.05-2.99	423-435	13-322	0.10-5.54	III	Poor

that may have been generated by Chichali and Samana Suk formations have been characterized. According to Hunt (1995) the sediments that have Type III kerogen are expected to have generated gas with HI values less than 200 mg HC/g TOC, whereas HI values greater than 300 mg HC/g TOC along with TOC values greater than 1 wt. % should generate oil. The analysed samples of Chichali and Samana Suk formations have average TOC 1.51 and 0.84% and have average HI values 129 and 80 mg HC/g TOC having Type III kerogen. The analysed Chichali formation is considered to have a poor to fair generative potential and gas could be expected to have been generated by Chichali formation, however analysed Samana Suk formation have poor generative potential.

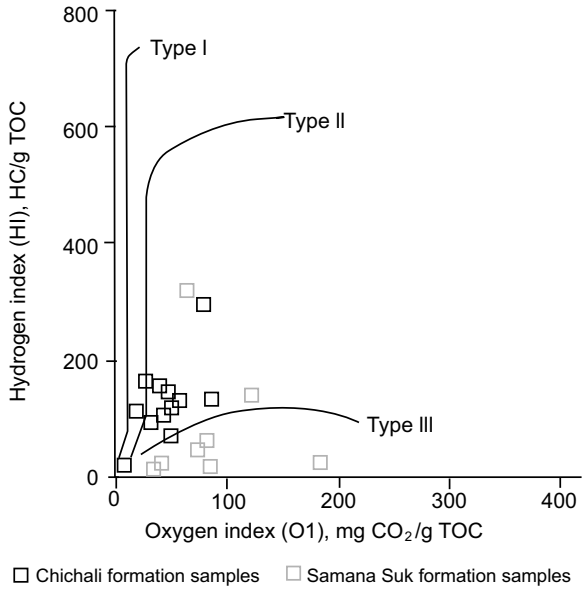

Fig. 3. Plot of HI *vs* OI showing type of organic matter of analysed samples.

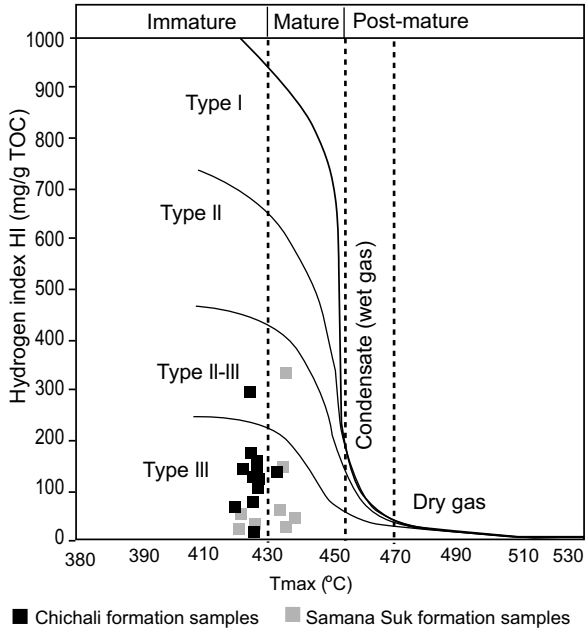

Fig. 4. (HI) versus T_{max} displaying thermal maturity and kerogen quality of the analysed samples.

Conclusions

The investigation of Chichali and Samana Suk formations sediments shows poor generative potential for oil, which is indicated by S2 values which are ranging from 0.05-3.08 mg HC/g rock and low HI values ranging from 13-322 HC/g TOC, and have OI values ranging from 15-182 mg CO_2/g TOC, having kerogen Type III as indicated by HI vs OI plot and HI vs plot. Only one sample of Chichali formation and five from Samana Suk formation shows early maturity window as indicated by HI vs Tmax plot. Chichali formation samples have TOC values ranging from 0.28-4.61 wt.% having average TOC of 1.51 wt.%. Therefore, some minor gas could be expected to have been generated from Chichali formation, whereas Samana Suk formation have poor generative potential.

Future recommendations. Chichali and Samana Suk formations can be further investigated by using advanced techniques like Py-GC, GC-MS, microfacies analysis and biomaker study for depositional and enviromental factors.

Acknowledgment

The authors are thankful to the Directorate General Petroleum Concession, Pakistan (DGPC) for the provision of data, OGDCL for providing the samples, and University of Malaya for lab analysis.

Conflict of Interest. The authors declare no conflict of interest.

References

Asim, S., Qureshi, S.N., Asif, S.K., Abbasi, S.A., Solangi, S., Mirza, M.Q. 2014. Structural and stratigraphical correlation of seismic profiles between Drigri Anticline and Bahawalpur high in

central Indus basin of Pakistan. *International Journal of Geosciences*, **5:** 1231-1240.

Fazeelat, T., Jalees, M.I., Bianchi, T.S. 2010. Source rock potential of eocene, paleocene and Jurassic deposits in the subsurface of the Potwar basin, northern Pakistan. *Journal of Petroleum Geology*, **33:** 87-96.

Hasany, S.T., Aftab, M., Siddiqui, R.A. 2012. In: *Proceeding of Refound Exploration Opportunities in Infracambrian and Cambrian Sediments of Punjab Platform, Pakistan*. Annual Technical Conference, Islamabad, Pakistan, **1:** 31-62.

Hunt, J.M. 1995. *Petroleum Geochemistry and Geology*, Freeman, W. H. & Co., 2nd edition, vol. **1,** 743 pp., New York, USA.

Kadri, I.B. 1995. *Petroleum Geology of Pakistan*, pp. 11-203, Pakistan Petroleum Limited Karachi, Pakistan, 275 pp.

Kazmi, A.H., Snee, L.W. 1997. Geology, *Gemology and Genesis*, **1:** 4-11, Emerald of Pakistan, Pakistan.

Kemal, A., Balkwill, H.R., Stoakes, F.A. 1991. Indus basin hydrocarbon plays. In: *International Petroleum Seminar on New Directions and Strategies for Accelerating Petroleum Exploration and Production in Pakistan*, pp. 16-57.

Peters, K.E, Clark, M.E., Das Gupta, U., McCaffrey, M.A., Lee, C.Y. 1995. Recognition of an infracambrian source rock based on biomarkers in the Baghewala-1 oil, India. *American Association of Petroleum Geologists Bulletin*, **79:** 1481-1494.

Peters, K.E., Cassa, M.R. 1994. Applied source rock geochemistry. In: *The Petroleum System-From Source to Trap*, Magoon, L.B., Dow, W.G. (eds.), American Association of Petroleum Geologists Memoir, **60:** 93-120.

Peters, K.E. 1986. Guidelines for evaluating petroleum source rock using programmed pyrolysis. *American Association of Petroleum Geologists Bulletin*, **70:** 318-329.

Raza, H.A., Ahmad, W., Ali, S.M., Mujtaba, M., Alam, S., Shafeeq, M., Riaz, N. 2008. Hydrocarbon prospects of Punjab platform Pakistan, with special reference to Bikaner-Nagaur Basin of India. *Pakistan Journal of Hydrocarbon Research*, **18:** 1-33.

Raza, H.A., Ahmed, R., Alam, S., Ali, S.M. 1989. Petroleum zones of Pakistan. *Pakistan Journal of Hydrocarbon Research*, **1:** 1-20.

Shah, S.B.A., Abdullah, W.H., Shuib, M.K.B. 2019. Petrophysical properties evaluation of Balkassar oil field, Potwar Plateau, Pakistan, implication for reservoir characterisation. Himalayan Geology, **40:** 50-57.

Shah, S.B.A., Ahmed, A. 2018. Hydrocarbon source rock potential of Paleocene and Jurassic deposits in the Panjpir oil field subsurface, Punjab platform, Pakistan. *Arabian Journal of Geosciences*, **11:** 607.

Shah, S.B.A., Abdullah, W.H. 2017. Structural interpretation and hydrocarbon potential of Balkassar oil field, eastern Potwar, Pakistan, using seismic 2D data and petro physical analysis. *Journal of the Geological Society of India*, **90:** 323-328.

Shah, S.B.A., Abdullah, W.H. 2016. Petrophysical properties and hydrocarbon potentiality of Balkassar well 7 in Balkassar oil field, Potwar Plateau, Pakistan. *Bulletin of the Geological Society of Malaysia*, **62:** 73-77.

Shah, S.I. 2009. *Stratigraphy of Pakistan*, pp. 3-150, Government of Pakistan Ministry of Petroleum & Natural Resources Geological Survey of Pakistan.

Tissot, B.P., Welte, D.H. 1984. *Petroleum Formation and Occurrenc*, 2nd eds, vol. **699,** pp. 25-140, Springer Berlin.

Wandrey, C.J., Law, B.E., Shah, H.A. 2004. Patala-Nammal composite total petroleum system, Kohat-Potwar geologic province, Pakistan. *US Geological Survey*, **1:** 1-18.

Pak. j. sci. ind. res. Ser. A: phys. sci. 2021 **64A**(1) 65-75

Design Optimization and Analysis of Rotor Blade for Horizontal-Axis Wind Turbine Using Q-Blade Software

Muhammad Mujahid, Abdur Rafai, Muhammad Imran*, Mustansar Hayat Saggu and Noor Rahman
Department of Mechanical Engineering, FET, IIU, Islamabad, Pakistan

(received August 19, 2019; revised February 7, 2020; accepted February 11, 2020)

Abstract. Wind energy plays a tremendous role in energy power sector in terms of wind turbine. Engineers and scientists are trying to improve the wind turbine design in order to get the maximum power efficiency from the wind, which is one of the most cheap and common renewable resource in nature. The objective of this study was to design a horizontal wind turbine rotor blade for a site of known wind data in order to extract the maximum power efficiency from the wind by using blade element theory analysis and Q-Blade simulation. Eight different aerofoils of different thicknesses from two NACA family 55xx and 00xx were considered for this study. The four different rotor blades were designed having length of 25 meter. Each blade consists of the combination of these NACA aerofoils which are oriented at different angles of attack and to simulate it at different Reynolds numbers. Comparative study was done to find the optimum blade design by considering the power output at two different rotational speeds and observe the effects of changing chord length and twist angle of final selected blade on these power output.

Keywords: wind energy, Q-Blade simulation, BEM theory, HAWT rotor blade, reynolds number

Introduction

The extraction of power energy from wind is becoming more popular (Kaveh and Sabeti, 2019) day by day because of two main reasons (Chaudhary and Prakash, 2019; Kaveh and Sabeti, 2019; Raut *et al*., 2017). The first reason is environmental friendly and the second one is its availability for free almost throughout the year (Hassanli *et al*., 2018; Saeed, 2018). This is the main reason that this area becomes more interest for the researcher, scientist and engineers to maximize the power efficiency from the wind resources by altering the size and shape of the wind turbine most commonly the rotor blade (Drumheller *et al*., 2015). Design and analysis for any application is critical to the service life and economics of the structures (Imran *et al*., 2019a, b and c; 2018).

Turbine is basically divide into two most common types, horizontal axis wind turbine (HAWT) and vertical axis wind turbine (VAWT) (Das and Talapatra, 2016). These are distinguished by the rotor design and rotating axis, each with its own favourable features (Hau, 2006). However, VAWT designs are not capable of producing a power in megawatt scale and need more development, so that it can be considered to compete with HAWT, while the popularity of HAWT can be attributed to increased rotor control through pitch and yaw control (Schubel and Crossley, 2012).

If we consider the power output of wind turbine, it can be divided into different categories as small (power output less than 100kW) and medium (power output between 100kW-1MW) (Tong, 2010). Small and medium wind turbines are essentially used for small home or villages to generate electricity (Lanzafame and Messina, 2010).

Since optimal rotor blade and high power efficiency is required for maximum power extraction from wind energy but the maximum energy that can be extracted from wind is 59%, which is explained by Bitz law (Broberg *et al*., 2018) and it is widely accepted (Gorban *et al*., 2001). Since in real practice the rotor design experiences some of minor losses like tip losses, wake effects and drive train efficiency losses; so, the maximum theoretical power efficiency has not yet been to achieved (Yurdusev *et al*., 2006).

HAWT are very sensitive to changes in blade profile and design (Tang *et al*., 2019). The most common parameters that influence the HAWT performance are, aerofoils selection, Reynolds number, tip speed ratio, chord length and twist angle (Ceyhan, 2012).

Successful blade design must satisfy a wide range of objectives too, some of which can be in conflict. These

*Author for correspondence;
E-mail: Muhammad.imran@iiu.edu.pk

objectives are to (1) Maximize annual energy production, (2) Restrict the maximum power output in the turbine, (3) Endure fatigue loads, (4) Limit tip deflections to avoid blade and tower collisions, (5) Prevent resonances, (6) Minimize weight and cost. The design process can be divided into two stages that the aerodynamic design, in which objectives (1) and (2) are satisfied, and the structural design. The aero dynamic design addresses the selection of the optimum geometry of the blade and the external surface, also referred to as the blade geometry. The blade geometry is defined by the aerofoil family and the chord, twist and thickness distribution. The structural design consists of blade material selection and determination of a structural cross section or spar within the external envelope that meets objectives (4) to (6) (Bossanyi *et al*., 2012).

For easiness during the production, several simplifications should be maintained along the process such as reducing the angle of twist, linearization of the chord width and reducing the number of different aerofoil profiles.

The aim of this study is to determine the aero dynamic performance of eight different aerofoils *viz*. 0020, 0018, 0015, 0012, 5520, 5518, 5515, and 5512 at different Reynolds number for rotor with 3 blades and 25 m radius using Q-Blade software and to find the optimum blade design for a specific wind corridor.

Material and Methods

Simulation and modeling. The main focus of this research is the rotor blade design because the horizontal wind turbines are highly sensitive to changes in blade profile and design, allowing great improvements when it comes to efficiency. The all simulation is carried in by Q-Blade software version 0.96. The software Q-Blade is to developed as an open source framework for the simulation and design of wind turbines.

In this study eight different NACA aerofoils from 4-digit family (i.e. 0020, 0018, 0015, 0012, 5520, 5518, 5515 and 5512) were selected. The NACA 4-digit aerofoil family has some advantages over the rest of the aerofoil family. The 4-digit has acceptable stall characteristics, a small centre of pressure movement across large speed range and they are less sensitive to roughness. Besides this, the type of aerofoils has a slightly low maximum lift coefficient, a high drag coefficient and a high pitching moment. Nonetheless, they have been used in several applications in general aviation, horizontal tails and HAWT with excellent performance. These aerofoils were simulated at different Reynolds number which was calculated according to minimum and maximum wind speed at given site by means of following expression:

$$Re = Vc/\nu \quad \text{..... (1)}$$

where:

ν = velocity of wind; c = chord width and ν = kinametic viscocity of air. Four different Reynolds number were determined, two for each according to minimum wind speed *i.e*. 5 m/sec and maximum wind speed *i.e*. 14 m/sec from a wind data of Jamshoro, with respect to maximum and minimum chord length, and then choose average value of Reynolds number from these four wind speed data that is 400000 and 1200000. However, the operating wind turbine blade elements experience different Reynolds numbers due to variable wind speed, chord width and different blade span locations. After Reynolds number calculation, the coefficient of lift and drag with respect to angle of attack *i.e*. -5 to 25 were calculated by simulating all these NACA aerofoils at each Reynolds number by using Q-Blade software. After aerofoils simulation, beam element theory (BEM) formulation was implemented to find the optimal blade rotor design. The length of rotor blade of 25 meter was considered in this study. The parameters such as chord length and twist angle for optimum blade design were derived from the following formulas (Wang *et al*., 2012).

$$C_{l,n} = (C_{i,\theta} - 0.3) + 0.3\,\frac{(n-1)}{N} \quad n = 1,2, \ldots N + 1 \quad \text{.... (2)}$$

$$\theta_{l,n} = (\theta_{i,\theta} - 6) + 12\,\frac{(n-1)}{N} \quad n = 1,2, \ldots N + 1 \quad \text{..... (3)}$$

where:

n = indicates the nth case; C_{in} and θ_{in} are the chord and twist angle at the ith blade element of the nth case respectively.

And by using other equation (Hau, 2006)

$$C_{opt} = \frac{2\pi r}{n}\,\frac{8}{9C_L}\,\frac{U_{wd}}{\lambda V_r} \quad \text{where } V_r = \sqrt{V_w^2 + U^2} \quad \text{.... (4)}$$

where:

r = radius (m); n = Blade numbers; C_L = coefficient of lift; λ = local tip speed ratio; V_r = Local resultant air velocity; U= wind speed; U_{wd} = design wind speed; C_{opt}

= Optimum chord length.

And the twist angle from equation (Manwell *et al*., 2010).

$$\Phi_i = \left(\frac{2}{3}\right) \tan^{-1} \frac{1}{\lambda_{r,i}} \quad \text{..... (5)}$$

$$\theta_{p,i} = \Phi_i - \alpha \quad \text{..... (6)}$$

where:

i = ith blade element; $\lambda_{T,i}$ = local tip speed ratio; Φ_i = relative angle of wind at i_{th} blade element, and $\theta_{p,i}$ = twist angle of i_{th} blade element.

After calculation of these parameters, data was implemented into Q-Blade software to design rotor blade for further simulation. The NACA aerofoils that are selected were used in combination by 4 different ways at different sections in the designed rotor blade so, that we have 4 different blades (*i.e*. 55xx multi blade, 00xx multi blade, 00xx55xx multi blade and 55xx00xx multi blade) of same length, same twist angle and same chord length but different aerofoils as shown in Fig. 1-3. Because the use of the same single aerofoil for the entire blade length would result in an inefficient design (Maalawi and Badr, 2003). By finding the coefficient of power (Cp) verses tip speed ratio (TSR) and Power (Hassanli *et al*., 2018) verses wind speed at two Reynolds number *i.e*. 400,000 and 1,200,000 at two different rotational speeds, the optimum rotor blade on base of maximum power output was selected.

After selection of optimum blade, the chord length and twist angle were changed to find the effects of both these parameters on power output of rotor. The losses factors such as tip losses, root losses and Reynolds drag corrections also considered throughout the simulations.

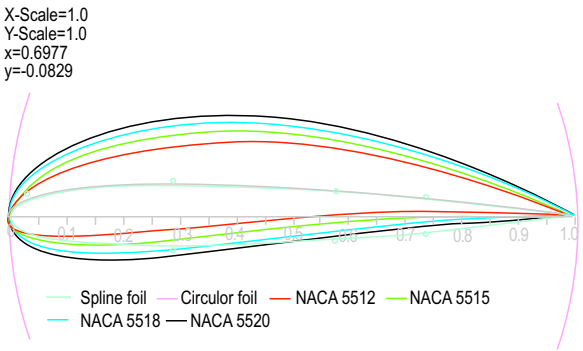

Fig. 1. NACA family 55xx aerofoils profile.

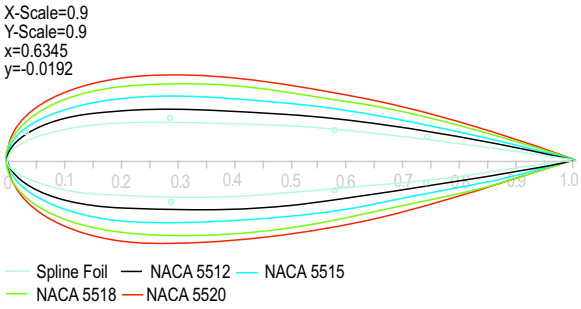

Fig. 2. NACA family 00xx aerofoils profile.

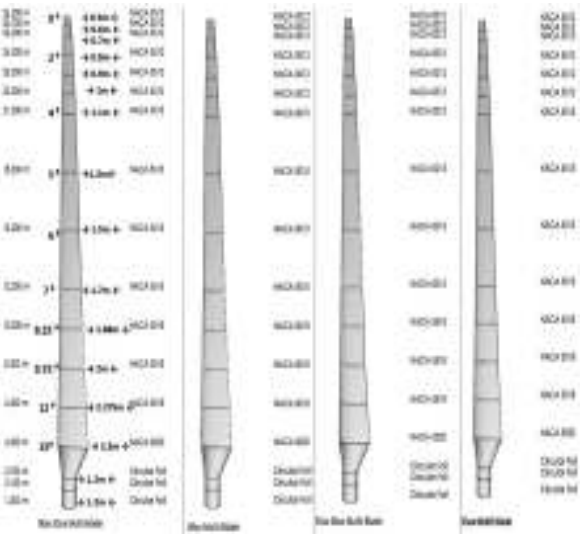

Fig. 3. Four different Rotor blade profiles design from Q-blade.

In the end, the optimal blade design selected on base of maximum power output efficiency, and it was evaluated for the distributions of aerodynamic loads at each blade section at wind speed of 15 m/s because the maximum speed at selected site is 14m/s. The aero dynamic loads were calculated by blade element momentum theory formulation as given below:

$$dFx = Cx.dq \quad \text{..... (7)}$$

$$dFy = Cy.dq \quad \text{..... (8)}$$

where:

$$Cx = C_L \sin\Phi - C_d \cos\Phi \quad \text{..... (9)}$$

$$Cy = C_L \cos\Phi + C_d \sin\Phi \quad \text{..... (10)}$$

$$\tan\Phi = \frac{(1-a)V_o}{(1-a'')\Omega_r} \quad \text{..... (11)}$$

$$dq = 1/2\rho w^2 cdr \quad \text{..... (12)}$$

The differential thrust and torque can be find by:

$$dT = BCydq \quad \text{..... (13)}$$

$$dQ = BCxdqr \quad \text{..... (14)}$$

where:

c = chord length; Ω = rotational speed of rotor.

The range of winds used for the analysis was between the maximum (*i.e*. 14 m/s) and minimum (*i.e*. 5 m/s) wind speed at the height of 50 m, encountered in Jamshoro during the wind site evaluation conducted by Pakistan Meteorological Department as shown in Fig. 4.

Beam element theory is implemented for the design of optimal rotor blade as shown in Fig. 3. Eight different aerofoils from two NACA 4-digits family were selected according to thickness and Reynolds number performance by using wind speed data at online airfoil tools. com and simulate all these eight aerofoils at Q-blade software were simulated.

Results and Discussion

The analysis of the designed rotor blade by using Q-blade software. First, the different NACA aerofoils and their aerodynamics parameter such as coefficient of lift and drag vs angle of attack will be discussed, than rotor blades performance such as coefficient of power *vs* TSR, and power output with respect to wind speed and in the last the thrust force and moment force at each section of optimal rotor blade.

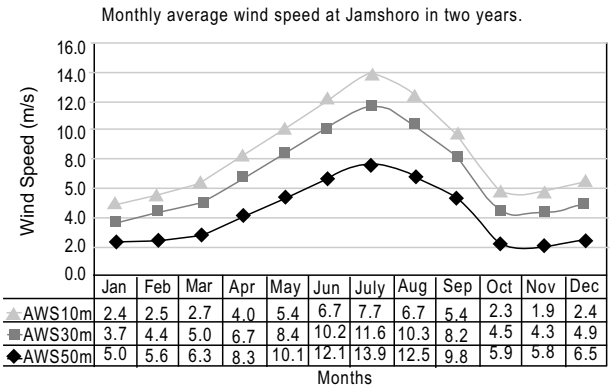

	Jan	Feb	Mar	Apr	May	Jun	July	Aug	Sep	Oct	Nov	Dec
AWS10m	2.4	2.5	2.7	4.0	5.4	6.7	7.7	6.7	5.4	2.3	1.9	2.4
AWS30m	3.7	4.4	5.0	6.7	8.4	10.2	11.6	10.3	8.2	4.5	4.3	4.9
AWS50m	5.0	5.6	6.3	8.3	10.1	12.1	13.9	12.5	9.8	5.9	5.8	6.5

Source:Pakistan meteorological department

Fig. 4. Wind speed data of Jamshoro by Pakistan meteorological department.

Aerodynamics of aerofoils. The analysis is done by Q-Blade by using eight different aerofoils from 2 NACA 4-digit families that is 0020,0018,0015,0012, and 5520,5518,5515,5512. The last two digits of each aerofoil represent the max thickness as shown in Fig. 2-3. The results from Q-Blade software simulation for each aerofoils at different Reynolds numbers (*i.e*. 400000, 800000 and 1200000) in between CL/Cd vs angle of attack are presented in Fig. 5.

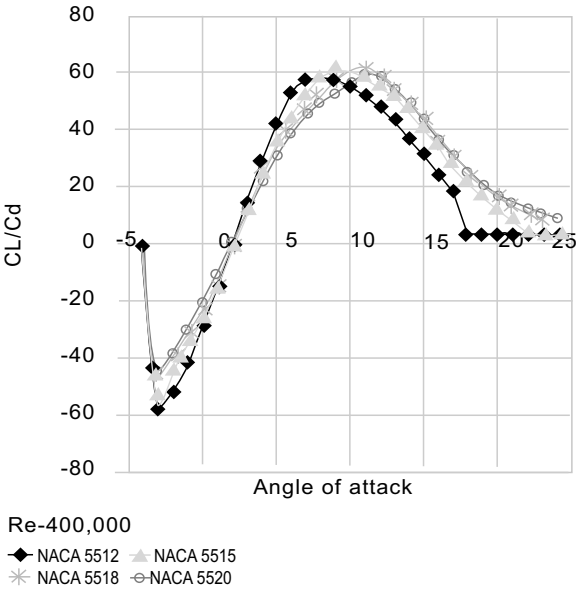

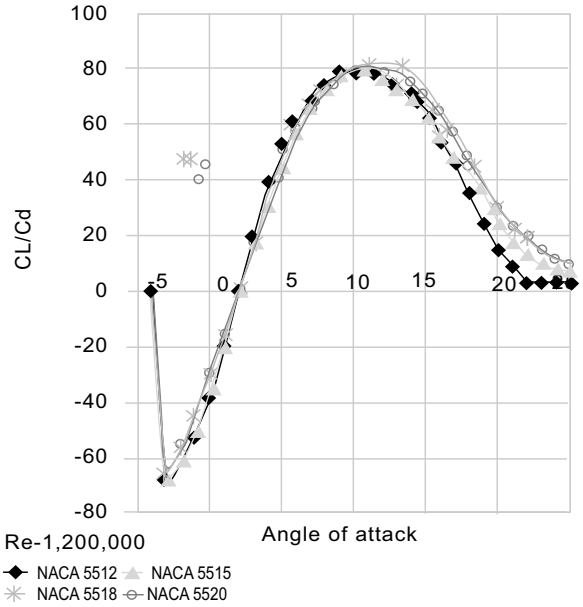

Fig. 5. Graphs between Cl/Cd vs angle of attack of NACA aerofoils 00xx family at different Reynolds number from Q-blade simulation.

In this section the selected two NACA families are considered for comparison. The comparison is done at different angles of attack from -5 to 25 degree for maximum Cl/Cd ratio. It can be seen from Fig. 5-6, that the coefficient of lift-to-drag ratio for NACA family 00xx is almost same at all thicknesses. The maximum Cl/Cd value is achieved at an angle of approximately 8-12 degrees, while it's maximum value is different at different Reynolds number. At Re-400000 the maximum coefficient of lift-to-drag ratio is almost 60 and at Re-1200000 it is increased and the maximum value reaches to 80.

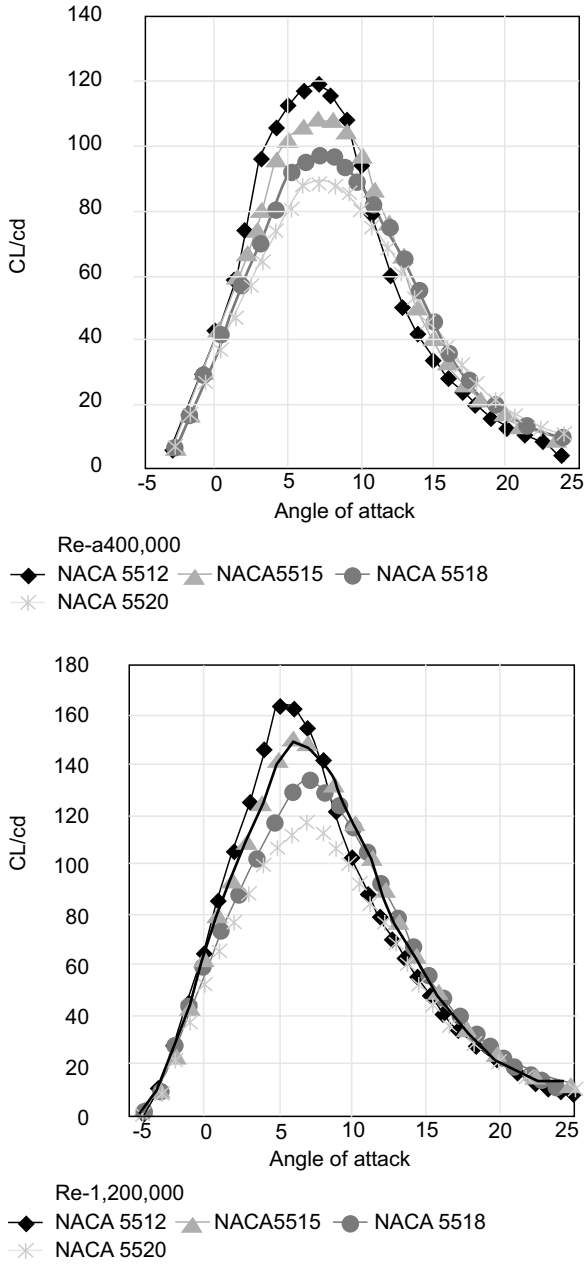

Fig. 6. Graphs between CL/CD vs angle of attack of NACA aerofoils 55xx family at different Reynolds number from Q-blade simulation.

On the other hand, the coefficient of lift-to-drag ratio for NACA family 55xx is gradually increased as the thickness of the aerofoils decreases. For this NACA family the maximum Cl/Cd is approximately achieved at an angle of 5-7 degree. The maximum Cl/Cd is observed by NACA 5512 at both different Reynolds number that is 120 for Re-400000 and almost 165 at Re-1200000. It is also clearly seen that the NACA foils family 00xx have negative coefficient of lift-to-drag ratio below 3 degree of angle of attack as shown in Fig. 5. The difference between Cl/Cd of these two NACA families is due to the shape of foils as shown in Fig. 2-3.

By observing these results, the max coefficient of lift-to-drag ratio occurred at different angles of attack of each aerofoil. Thus the aerofoils can be choosen for different applications that are depending upon the aerodynamic parameters requirement. While for particular applications not only Cl/Cd ratio is considered but other parameters such as maximum camber and maximum thickness are also considered.

The reason of low coefficient of lift-to-drag ratio at low Reynolds number is that, NACA profiles are usually developed for high Reynolds number and thus suffer from significant laminar separation bubbles when it operate at low Reynolds number. Due to this laminar separation the coefficient of lift decreases, while coefficient of drag increases gradually (Alom and Saha, 2019).

Power efficiency. ***Coefficient of power versus tip speed ratio*****.** After the complete simulation and evaluation of all aerofoils by means of coefficient to lift, coefficient of drag and angle of attack, these aerofoils were further used in the design blade at different sections by considering root, span, tip and twist angle is four different ways and its performance evaluated with respect to power coefficient, Tip speed ratio and power output. Mean value of wind speed was calculated as 9 m/s from a selected site. Fig. 7 show the graphs between coefficient of power vs tip speed ratio at two different Reynolds number and was obtained from Q-Blade.

It is seen from graphs that for all different rotor blades, the coefficient of power value initially increases, reaches

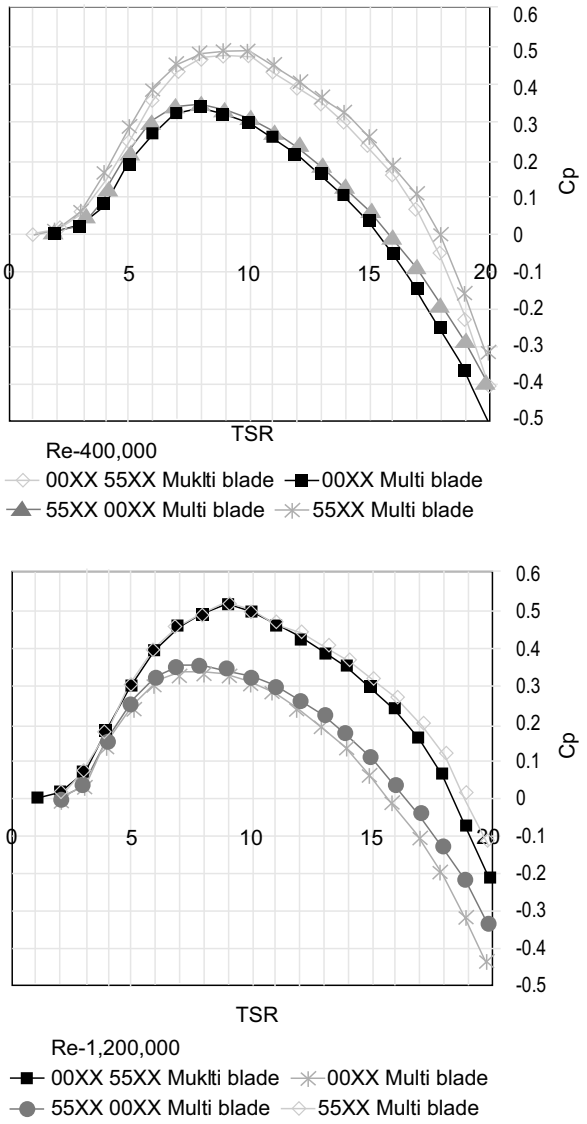

Fig. 7. Graph between coefficient of power and tip speed ratio at two different Reynolds number from Q-blade simulation.

to maximum and then decrease gradually with increase in tip speed ratio.

Also it was observed that maximum Cp value occurs at different values of TSR for different blades *i.e*. at Re-400000, for Blade 00xx and 55xx00xx, Cp maximum (*i.e*. 0.35) is obtained at TSR=8, whereas for blades 55xx and 00xx55xx, C_{pmax} obtained at TSR=10, that is approximately 0.48. Similarly at Re-1200000, the C_{pmax} for blades 00xx and 55xx00xx is almost same as that is at Re-40, but the TSR decrease to 7. The same situation also observed for blades 55xx and 00xx55xx which gives maximum power coefficient (*i.e*. approx. 0.5 to 0.52) now at TSR=9.

It is clear in graphs that simulation and the Reynolds number increases and shows the maximum power coefficient was obtained at more low tip speed ratio. Tip speed ratio is basically the ratio between the wind speed and the rate of rotor rotation. Generally a high TSR is a desirable feature for horizontal wind turbine, since it results in a high shaft rotation and a result at high power extraction but on the other side, if blade rotor turns too fast, the rotating blades act like a solid wall for incoming wind flow, resulting in reduced power extraction. The rotating of rotor too slowly is also not desirable because most of the wind will pass without interaction with rotor blades and hence little power extracted (Song *et al*., 2018).

Power output verses wind speed. The main objective of this research was to select an optimal design for the specific wind corridor. So, in this section we will briefly describes the power output of all four designed blades with respect to wind speed and find the best one which gives the maximum power output at desirable wind speed for the given site. For this purpose the four different blade designs were simulated at Q-blade at two different rotational speeds of rotor blades (*i.e*. rpm 20 and 25) and two different Reynolds number that was calculated early according to minimum and maximum wind speeds. The power output of our concern was 5 m/s to 14 m/s that is a minimum and maximum wind speed of selected area but simulation was taken from 0-30 m/s.

It is seen from Fig. 8-9 and Table 1-2, the cut in speed for each blade is 5 m/s, but whenever the speed of wind increases, the difference in power output is observed for each blade profiles with respect to Reynolds number and rotational speed of rotor blade. If we compare the power verses wind speed with respect to Reynolds number, it is clearly observed that at low Reynolds number (*i.e*. R=40E4), the power output at each wind speed is lower than that of observed for high Reynolds number (*i.e*. Re-120E4). Also it was observed that the blade profiles 55xx and 00xx55xx give maximum power output at each wind speed and each Reynolds number, while the other two blades 00xx and 55xx00xx give minimum power output.

However, the rotational speed is also greatly influenced on the power efficiency of these rotors blades as shown in Fig. 7-8 and Table 1-2. It is clearly observed that at

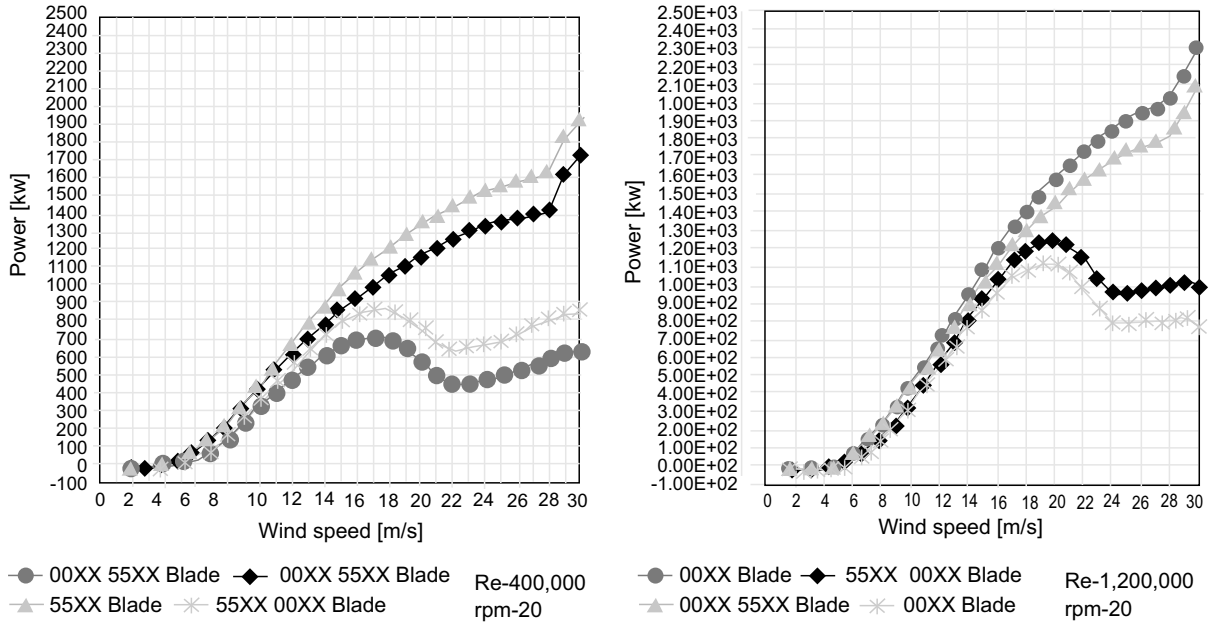

Fig. 8. Graph between power vs wind speed at 20 rpm from Q-blade.

rotational speed of 20 rpm, the power output is small as compared to high rotation speed. At high rotational speed i.e. 25 rpm the power output is gradually increased for all different blades profiles. The other important factor observed is that, at low rotational speed the cut-in speed of HAWT blades were starting at 4 m/s of wind speed, while for rotational speed of 25 rpm, its cut=in speed started at 5 m/s.

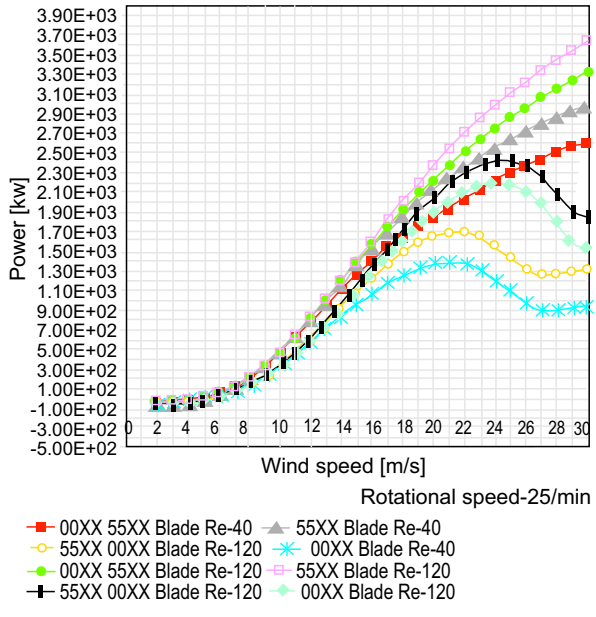

Fig. 9. Graph between power vs wind speed at Reynolds number 40E4 and 120E4 and rotational speed 25/min.

Apart from the main objective to find the optimum blade design, another important factor is also observed that, for large rotor blade, the aerofoils selection at each section throughout the blade length largely affect the power output efficiency. A close look to the graphs and table values show that, the blade profile 00xx consist of only 00xx aerofoils family throughout the length as shown in Fig. 3. The power output of this blade was low as compared to NACA 55XX family blade, but when we combine the NACA 55xx aerofoils from mid span up to tip of blade (*i.e.* 00xx 55xx blade) the power output gradually increased and reached somewhat near to 55xx blade profile which has high power efficiency. Similarly when the 00xx NACA aerofoils is combined with 55xx family from mid spin up to tip, the power output efficiency observed was much low as compared to 55xx blade profiles.

So, from this observation, we can conclude that aerofoils that have max camber line and tailing edges can give a maximum power output, if we use it in blade profiles from mid span to tip while the aerofoils at root have not much effect on power output efficiency.

Effect of chord length and twist angle on power output. The rotor blade considered for this study is 55xx blade, which has high power efficiency from other three blade

designs. The actual chord length of selected blades rotor was 2.5 m. So, we changed the chord length throughout the blade length, while the twist angle was kept the same as the previous deigned 55xx blade. The new max chord lengths was consider 3 meter and 2 meter at the same position as that of previous blade and then it was changed throughout blade length according to formulas that have already been described in section 2 as shown in Fig. 10.

Figure 10 shows that the selected chord length has not much effect on power output efficiency with respect to wind speed. The output power is approximately same for all four blade designs up to wind speed of 14 m/s, while at high wind speed, the maximum chord blade lengths have a significant increase in power output efficiency as compared to other two.

Figure 11 is plotted between power output and wind speed at different twist angle. The optimal blade design

Table 1. Power vs wind speed at Reynold number = 400,000

Wind	Power (Hassanli, *et al*.)							
speed	00xx 55xx Multi blade		00xx Multi blade		55xx 00xx Multi blade		55XX Multi blade	
m/s	rpm-20	rpm-25	rpm=20	rpm-25	rpm-20	rpm-25	rpm-20	rpm-25
1	-25.3948	-49.7708	-21.4752	-42.664	-21.5026	-42.8791	-25.3614	-49.8780
2	-24.7222	-48.0237	-24.0279	-40.3077	-20.5764	-39.0077	-21.8895	-46.7087
3	-9.56349	-40.1650	-14.4824	-41.0640	-11.3115	-34.3708	-7.21338	-34.8772
4	21.1599	-6.44814	4.30017	-22.7345	7.27984	-16.7596	23.2237	-2.00342
5	65.1603	41.3278	35.9195	8.39878	39.4725	14.2184	67.5841	45.3588
6	133.764	106.973	83.2012	55.5994	88.0399	62.2151	137.673	111.437
7	215.848	200.123	148.356	121.708	154.121	130.307	220.979	206.512
8	315.243	322.608	230.606	209.015	238.854	218.779	323.039	330.635
9	418.211	458.211	314.784	319.700	335.384	331.548	438.364	468.918
10	525.254	615.710	400.570	450.402	435.267	466.512	559.654	630.935
11	627.850	786.099	481.705	592.149	533.566	616.277	679.606	809.547
12	704.582	950.169	541.959	723.354	629.040	772.369	791.312	998.076
13	778.800	1114.23	602.996	853.698	717.942	928.419	892.186	1188.55
14	859.804	1246.72	663.155	953.642	790.820	1080.10	985.789	1372.88
15	924.129	1376.14	692.805	1058.51	840.586	1228.59	1069.67	1545.53

Table 2. For power vs wind speed at Reynold number = 1,200,000

Wind	Power (Hassanli, *et al*.)							
speed	00xx 55xx Multi blade		00xx Multi blade		55xx 00xx Multi blade		55XX Multi blade	
m/s	rpm-20	rpm-25	rpm=20	rpm-25	rpm-20	rpm-25	rpm-20	rpm-25
1	-25.3948	-49.7708	-21.4752	-42.664	-21.5026	-42.8791	-25.3614	-49.8780
2	-24.7222	-48.0237	-24.0279	-40.3077	-20.5764	-39.0077	-21.8895	-46.7087
3	-9.56349	-40.1650	-14.4824	-41.0640	-11.3115	-34.3708	-7.21338	-34.8772
4	21.1599	-6.44814	4.30017	-22.7345	7.27984	-16.7596	23.2237	-2.00342
5	65.1603	41.3278	35.9195	8.39878	39.4725	14.2184	67.5841	45.3588
6	133.764	106.973	83.2012	55.5994	88.0399	62.2151	137.673	111.437
7	215.848	200.123	148.356	121.708	154.121	130.307	220.979	206.512
8	315.243	322.608	230.606	209.015	238.854	218.779	323.039	330.635
~~9~~	~~418.211~~	~~458.211~~	~~314.784~~	~~319.700~~	~~335.384~~	~~331.548~~	~~438.364~~	~~468.918~~
10	525.254	615.710	400.570	450.402	435.267	466.512	559.654	630.935
11	627.850	786.099	481.705	592.149	533.566	616.277	679.606	809.547
12	704.582	950.169	541.959	723.354	629.040	772.369	791.312	998.076
13	778.800	1114.23	602.996	853.698	717.942	928.419	892.186	1188.55
14	859.804	1246.72	663.155	953.642	790.820	1080.10	985.789	1372.88
15	924.129	1376.14	692.805	1058.51	840.586	1228.59	1069.67	1545.53

that is 55xx blade having max twist angle 15 degree at root was considered and its twist angle was changed by 24 degree and 10 degree. The other parameters such as length and chord width were kept constant and then its effect on power output efficiency was evaluated.

It was observed that no major difference occurred on power output efficiency due to change in twist angle up to wind speed of almost 18 m/s for this rotor blade. At wind speed greater than 20 m/sec, an increase in power efficiency was observed.

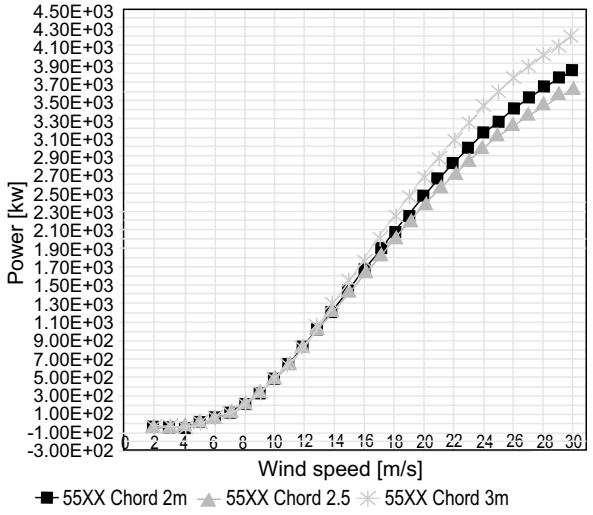

Fig. 10. Graph power verses wind speed at different chord length.

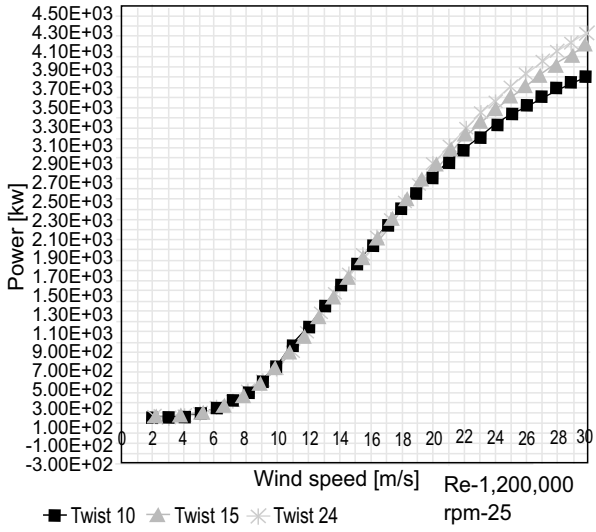

Fig. 11. Power output vs wind speed at different twist angle.

So, the blade design 55xx is more favourable and no need of change of twist angle required. The large twist angle blade (*i.e*. 24 degree) has slightly more power output efficiency than the optimum blade design (*i.e*. 15 degree) but, due to large twist, the main drawback is of manufacturing difficulty and cost (Rahimi, 2018). On the other hand decreasing the twist angle can cause increase in thrust force. So, the 55xx rotor blade should be considered as an optimal blade design.

***Aerodynamic loads*.** Aerodynamics loads are usually generated by lift and drag forces of the blades aerofoil section which is greatly dependent on wind velocity, surface finish, angle of attack, aerofoils profile and blade velocity. These aerodynamic lift and drag forces are resolved in useful thrust (T) and torque.

After comparison between four different rotor blade designs, the optimal rotor blade design is selected on the basis of maximum power efficiency that is 55XX blade design. The normal forces, tangential forces (*i.e*. thrust) and torque was calculated by using blade element theory (BEM) formulation as described in Table 3.

Table 3. Aerodynamics forces for 55xx blade

Position (r/R)	Normal force (N)	Tangential force (N)	Torque (Nm)
0.06	715	3433	1072.5
0.12	1498	7152	4500
0.2	2217	12854	11085
0.28	2190	15556	15330
0.36	2342	19591	21078
0.44	2370	23280	26070
0.56	3423	39640	47922
0.68	3172	45077	53924
0.8	2670	37741	53400
0.92	682	118921	15699
1	-1488	417046	-37200
Total	19791	739071	212880

Conclusion

This project spanned the entire process involved with designing and analysing an optimal 25 meter horizontal wind turbine rotor blade for a specific wind corridor. The rotor blade design process starts with the basic collection of aerofoils performance for the wind conditions at the turbine site to determine what can be done to increase the amount of wind energy captured

by turbine. For this purpose, a 25 meter rotor blade is considered for this study.

After finding the results of different simulations done by Q-Blade software, it is concluded that an optimal design of rotor blade for this site is 55xx blade. This design blade captures the power from wind at 4 m/sec while, the minimum power range for this site is 5 m/sec. This blade design gives approximately 500kw at mean wind speed of 9 m/s that is a more desirable characteristics. Furthermore, the effect of change in chord length and twist angle on power output efficiency is also analysed in this study. These results show that there is very little effect of these changing on the power output in the wind speed range up to 18 m/sec.

Acknowledgment

Authors acknowledge the Department of Mechanical Engineering, International Islamic University, Islamabad, H-10 Campus.

Conflict of Interest. The authors declare no conflict of interest.

References

Alom, N., Saha, U.K. 2019. Evolution and progress in the development of savonius wind turbine rotor blade profiles and shapes. *Journal of Solar Energy Engineering*, **141:** 150-165.

Bossanyi, E., Savini, B., Iribas, M., Hau, M., Fischer, B., Schlipf, D., Carcangiu, C. 2012. Advanced controller research for multi-MW wind turbines in the UPWIND project. *Wind Energy*, **15:** 119-145.

Broberg, D., Shah, D., Drapcho, S., Brockway, A. 2018. Getting more out of the wind, extending Betz's law to multiple turbines. *arXiv preprint arXiv*, 1805-1820.

Ceyhan, O. 2012. Towards 20MW wind turbine, In: *Proceedings of High Reynolds Number Effects on Rotor Design. Paper presented at the 50th AIAA ASM Conference*, Nashville, Tennessee, USA.

Chaudhary, M.K., Prakash, S. 2019. Investigation of blade geometry and airfoil for small wind turbine blade. *Advanced Science, Engineering and Medicine*, **11:** 448-452.

Das, A., Talapatra, P.K. 2016. Modelling and analysis of a mini vertical axis wind turbine. *International Journal of Emerging Technology and Advanced Engineering*, **6:** 184-188.

Drumheller, D.P., D'Antonio, G.C., Chapman, B.A., Allison, C.P., Pierrakos, O. 2015. Design of a micro-wind turbine for implementation in low wind speed environments, paper presented at the 2015 *Systems and Information Engineering Design Symposium*.

Gorban, A.N., Gorlov, A.M., Silantyev, V.M. 2001. Limits of the turbine efficiency for free fluid flow. *Journal of Energy Resources Technology*, **123:** 311-317.

Hassanli, S., Kwok, K.C., Zhao, M. 2018. Performance assessment of a special double skin façade system for wind energy harvesting and a case study. *Journal of Wind Engineering and Industrial Aerodynamics*, **175:** 292-304.

Hau, E. 2006. *Wind Turbines: Fundamentals, Technologies, Application, Economics*, pp. 408-411, Springer.

Imran, M., Badshah, S., Khan, R. 2019a. Vibration analysis of cracked composite laminated plate: a review. *Mehran University Research Journal of Engineering and Technology*, **38:** 705-716.

Imran, M., Khan, R., Badshah, S. 2019b. Finite element analysis to investigate the influence of delamination size, stacking sequence and boundary conditions on the vibration behaviour of composite plate. *Iranian Journal of Materials Science and Engineering*, **16:** 11-21.

Imran, M., Khan, R., Badshah, S. 2019c. Investigating the effect of delamination size, stacking sequences and boundary conditions on the vibration properties of carbon fiber reinforced polymer composite. *Materials Research*, 22: http://orcid.org/0002-2704-6813.

Imran, M., Khan, R., Badshah, S. 2018. Vibrtaion analysis of cracked composite laminated plate. *Pakistan Journal of Scientific and Industrial Research Series A: Physical Sciences*, **61:** 84-90.

Kaveh, A., Sabeti, S. 2019. Optimal design of monopile offshore wind turbine structures using CBO, ECBO, and VPS algorithms. *Scientia Iranica*, **26:** 1232-1248.

Lanzafame, R., Messina, M. 2010. Power curve control in micro wind turbine design. *Energy*, **35:** 556-561.

Maalawi, K., Badr, M. 2003. A practical approach for selecting optimum wind rotors. *Renewable Energy*, **28:** 803-822.

Manwell, J.F., McGowan, J.G., Rogers, A.L. 2010. *Wind Energy Explained, Theory, Design and Application*, 2nd edition, J. F. Manwell, J. G. McGowan, A. L. Rogers (eds.), John Wiley & Sons, Ltd.

Rahimi, M. 2018. Control and performance assessment of variable rotor resistance based wind turbines regarding the aerodynamic power fluctuations. *Scientia Iranica*, **25:** 1593-1607.

Raut, M.S., Shrivas, M.S., Sanas, M.R., Sinnarkar, M.N., Chaudhary, M. 2017. Simulation of micro wind turbine blade in Q-Blade. *International Journal for Research in Applied Science and Engineering Technology*, **5:** 256-262.

Saeed, A. 2018. Potential of wind power in Pakistan. *Journal of Information Communication Technologies and Robotic Applications*, 28-35.

Schubel, P.J., Crossley, R.J. 2012. Wind turbine blade design. *Energies*, **5:** 3425-3449.

Song, D., Yang, J., Fan, X., Liu, Y., Liu, A., Chen, G., Joo, Y.H. 2018. Maximum power extraction for wind turbines through a novel yaw control solution using predicted wind directions. *Energy Conversion and Management*, **157:** 587-599.

Tang, H., Lam, K.M., Shum, K.M., Li, Y. 2019. Wake effect of a horizontal axis wind turbine on the performance of a downstream turbine. *Energies*, **12:** 2395-2405.

Tong, W. 2010. *Wind Power Generation and Wind Turbine Design*, Wit Press, Kollmorgan Corporation, USA. (www.WitPress.com).

Wang, L., Tang, X., Liu, X. 2012. Optimized chord and twist angle distributions of wind turbine blade considering Reynolds number effects. *Wind Energy*, Materials, Engineering and Policies (WEMEP). http://www.citeseerx.ist.P.S.O.edu.

Yurdusev, M., Ata, R., Cetin, N. 2006. Assessment of optimum tip speed ratio in wind turbines using artificial neural networks. *Energy*, **31:** 2153-2161.

Pak. j. sci. ind. res. Ser. A: phys. sci. 2021 **64A**(1) 76-83

Experimental Investigation of the Influence of Stacking Sequence and Delamination Size on the Natural Frequencies of Delaminated Composite Plate

Muhammad Imran*, Rafiullah Khan and Saeed Badshah
Department of Mechanical Engineering, International Islamic University, Islamabad, Pakistan

(received January 16, 2019; revised July 8, 2019; accepted July 17, 2019)

Abstract. The vibration properties of the composite structures is critical to the reliability and durability of the structures. Vibration becomes worst in case the delamination is present within laminates. In this research work, experimental, finite element and analytical techniques have been applied in order to analyze the influence of stacking sequence and delamination sizes on the natural frequencies of carbon fiber reinforced polymer composite (CFRP) plate with and without delamination. The boundary conditions in this research work was (SSSS) (all sides simply supported. Experiments were performed to study the vibration characteristics of (CFRP) delaminated composite plate. Software package ABQUS was used to model and analyze the vibration response of carbon fiber reinforced polymer composite plate for (SSSS) boundary condition and the effect of stacking sequence and delamination size was calculated. Rayleigh-Ritz Method was used to find the natural frequencies for different delamination sizes and stacking sequences. The results was concluded that natural frequencies were significantly affected by the delamination sizes and stacking sequences. Stacking sequence of (0/90/45/90) showed higher values of natural frequencies in lower mode subjected to all-sides simply supported boundary conditions. It was interesting to see that there were small differences in values of natural frequencies among the stacking sequences for lower modes but the difference gradually increased in case of higher modes.

Keywords: experimental vibrations, delamination, composite plate, finite element analysis, simulations

Introduction

Composite materials have many advantages when compared to conventional materials (Karsh *et al*., 2018; Imran *et al*., 2018 and b). They are lightweight, cheaper, stiffer, stronger and eco-resistant (Kumar *et al*., 2017; Bakis *et al*., 2002). A good example of a composite material is carbon fibre reinforced polymers. To form a carbon fibre reinforced polymer, two components are required. They include reinforcement and a matrix. The reinforcement needed is achieved through the carbon fibre. It is the reinforcement of the carbon fibre that gives the required strength to the composite material being formed. The matrix on the other hand provides bonding between the reinforced materials. and an example of a matrix is epoxy (made from polymer resin) (Imran and Badshah, 2012; Bakis *et al*., 2002). Usually, the characteristics of the carbon fibre reinforced polymers formed depend on the reinforcement and the particular matrix used. For example, reinforcement components like elasticity and stress determines the rigidity and strength of the carbon fibre reinforced polymers. This is why the property strength of carbon fibre reinforced polymers is usually described as directional and distinct from isotropic structures like aluminum. It must not be forgotten that the carbon fibre layout also has the ability to influence the carbon fibre reinforced polymers properties (Corum *et al*., 2000). Composite laminates are preferred due to their many advantages such as their high-strength, bending stiffness and resistant to expansion (Agarwal *et al*., 2017; Imran, 2015). Usually, composite laminates are formed from a hybrid of fibre matrix layers. The fibre usually consists of such materials as boron or glass, while the matrix consist of such materials as aluminum or epoxy. Undoubtedly, Fibre reinforced composites have gained wide use in many aspects of engineering applications. They have been applied in ship building, mechanical, aerospace, etc. They are preferred because of the advantages they have such as superior mechanical characteristics, high-strength, their stiffness ratio to weight is excellent (Friedrich and Almajid, 2013). One of the crucial parameter in composite laminates is delamination that

*Author for correspondence;
E-mail: muhammad.imran@iiu.edu.pk

are generated accidentally either during service period or during manufacturing of the composites (Saghafi *et al*., 2017; Yelve *et al*., 2017; Kharghani and Guedes, 2016).

Structures prior to be applied in service should be investigated (Imran *et al*., 2019 a,b& c; Shao *et al*., 2017). Delamination is the sensitive defect that affect the vibration characteristics of carbon fibre reinforced polymer composites (Imran *et al*., 2018 a&b; Venkate *et al*., 2017) so, it is quiet important to study the influence of stacking sequences and delamination sizes (Imran *et al*., 2019 a,b&c).

A lot of studies have been done to investigate the vibration properties of composite structures like composite beam, composite shells, glass fiber reinforced polymer composite structures, however studies to find the effect of different parameters like stacking sequences and delamination sizes are scarce (Imran *et al*., 2019 a,b&c). In following paragraphs, we will do literature studies to find the effect of the above parameters on the vibration characteristics of different composite structures.

Shu and Della (2004) studied the free vibration impact of composite beams subjected to multiple delaminations. Classical Euler-Bernoulli was used as governing equation. It was concluded that primary and secondary frequencies decreases as the length of the delamination increased, however reduction of primary frequency is not significant. In this study the size effect of delamination was also analyzed. No effect on frequency for short delamination was observed contrary to large delamination that reduced the natural frequency significantly. It was also observed that natural frequency and mode shapes are largely dependent of the assumed constraints. Jadhav and Bhoomkar (2016) carried out experimental and finite element analysis of cracked composite laminated beam.

Lee *et al*. (2002) conducted the vibration analysis and analyzed the effect of multi-delamination on the vibration properties of multi-delaminated composite beam columns. Loading was axial compressive. It was shown that effect of multi delaminations are more significant than those for single delamination. Kim and Hwang (2002) investigated the influence of delamination. They found that the natural frequencies and vibration mode shapes in honeycomb sandwich beams. Delamination was embedded between the face layers of carbon/epoxy laminates and nomex-aramid honeycomb cores. Equation of motion of the split sandwich beam was used for debonded honeycomb sandwich beam. An increase in value of debonding or delamination. They observed that value of natural frequency reduced. At delamination length of 50 mm, a critical debonding point was observed at beyond which response of natural frequencies was unpredictable or disproportional. Also mode shapes become smaller for the increase in debonding size. The theoretical results obtained in this analysis were close to the experimental measurements.

Brandinelli and Massabò (2003) conducted analysis to find the free vibration characteristics of beam-type composite structures subjected to delamination with proposed analytical solution using the mid-plane delamination and constrained model assumptions. They neglected the shear deformations and considered it as homogeneous material. It has been observed that opening mode continues to disappear as the transversal longitudinal spring stiffness tends to increase from zero to higher values. Luo *et al*. (2004) did an investigation to find the non-linear vibration properties of the composite beam subjected to variation in sizes and positions of the delamination. Since the amplitude is small, larger value of frequency would be observed with greater length of delamination. Frequency increases relatively slow with an increase in length of the delamination. As the value of amplitude is increased, the influence of the positions or locations of delamination gets clearer. The influence by transverse shear deformation has significant importance and cannot be considered as no impact for non-linear vibration characteristics of composite beam.

Nanda and Sahu (2012) find the vibration response of delaminated composite shell using first order shear deformation theory subjected to cylindrical, spherical and hyperboloid shells. The value of linear frequency showed increasing trend with reduction of number of layers. This frequency difference continues to increase after the six number of layers. Moreover, higher modes were more influenced by the delamination. Yam *et al*. (2004) analyzed the dynamic behaviour of composite plate with multi-layered structure subjected internal delamination. Eight-node rectangular thin element was used for finite element formulation. It was concluded that local internal delamination had slight or negligible influence on the natural frequencies of laminated

composite plate with multi-layers. Moreover it was also found that natural frequency decreases if the area of delamination is increased. Kim *et al*. (2003) found the effect of delamination and without delamination on cross-ply laminates with various delamination at multiple places. They used layer-wise composite laminate theory. It was observed that natural frequencies decreased with delamination and there is significant difference between delaminated and without delaminated structure.

The vibration characteristics of delaminated composite laminates using finite elements and used third order shear deformation theory which studied by (Thornburgh and Chattopadhyay, 2003; Thornburgh and Chattopadhyay, 2001). Ply thickness was reduced, while incorporating matrix cracking.

Mohammed (2017) carried out vibration analysis of cantilever composite beam produced by hand-lay-up method. They used Matlab, Solidworks and did experiments to find the effect of fibre angles on the mode shapes and natural frequencies. Juhász *et al*. (2017) developed a model using finite element analysis predicting the modal analysis in through-width delaminated composite plate and the results were validated experimentally. Zhang *et al*. (2018) conducted finite element and experimental analysis to find the vibration properties of carbon fibre and glass fibre reinforced polymer composite plates. They analyzed the influence of delamination size and delamination location on the natural frequencies. (Tsongas *et al*., 2017: Vo *et al*., 2017) carried out free vibration analysis using ANSYS and ABAQUS and compared the results with numerical ones obtained from shear and normal deformation theory on the axial loaded composite beam.

From the above literature, it is observed that the vibration analysis subjected to (SSSS) boundary conditions with different delamination sizes for these three stacking sequences (0/45), (0/90) and (0/90/45/90) is very poor. Therefore, it is utmost important to investigate the vibration characteristics of carbon fiber reinforced polymer composite plate.

Finite element approach using ABAQUS. It shows delaminated region modeled in ABAQUS software package version 16. In order to find the dynamic characteristics of delaminated carbon fibre reinforced composite plate, SOLID (Eight-node brick element) was used as element type and average number of elements per model were 180000. The orientation of the layers were modeled using coordinate system. All delamination surfaces are located in the middle-plane of the composite laminated plate as shown in Fig. 1.

A total of 48 models each consisting in at least 12 natural frequencies and their corresponding modal shapes were computed.

Materials and Method

The composite plate samples were prepared using handy layup method (Imran *et al*., 2019) and cured at room temperature. Teflon tape having sizes of 6.25%, 255 and 56.25% was used as delamination in the center of the composite plate and layers were stacked as per their configuration like (0/90/45/90), (0/90) and (0/45). In this case, eight layers of laminates were joined together using 50:50 fibre to matrix weight with mid plane delamination. Free vibration analysis was conducted by using Model Hammer Model 2302 and FFT analyzer Model 3560 (Karim11 *et al*., 2017; Tsongas *et al*., 2017; Mishra & Sahu, 2012) as shown in Fig. 2. Simple layout

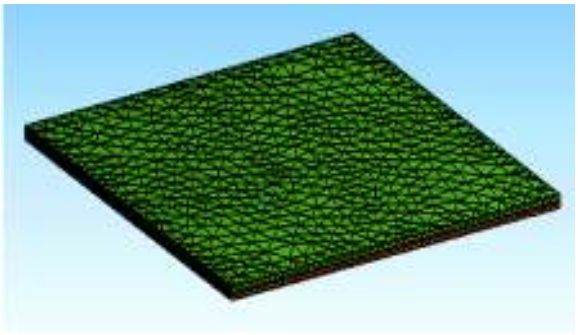

Fig. 1. View of mesh created for composite plate.

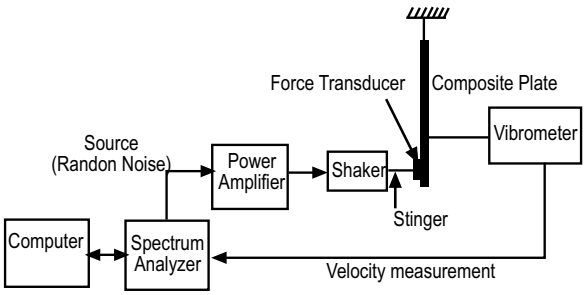

Fig. 2. Simple layout of Experimental Setup.

of experimental setup The natural frequencies of all plates subjected to all sides simply supported were determined with and without delaminated plate.

Analytical analysis. Rayleigh Ritz Method (Oliveri and Milazzo, 2018; Vescovini *et al*., 2018; Ardestani *et al*., 2017; Sayyad and Ghugal, 2017) is used to find the natural frequencies as in equation (1)

$$\omega^2 = \frac{1}{\rho}\left(\frac{A^4 D_x}{a^4} + \frac{B^4 D_y}{b^4} + \frac{2CD_{xy}}{a^4 b^4}\right) \cdots\cdots\cdots\cdots (1)$$

where:

A, B, C and D are frequency coefficients dependent on the boundary conditions of the structure. After putting the values of all sides simply supported boundary conditions in the equation (2), we will solve this in Matlab tool to analyze the natural frequencies.

$$\omega_{m,n} = \frac{\pi^2}{a^2\sqrt{\rho}}\sqrt{D_x\, m^4 + 2D_{x,y}\, m^2 n^2 \left(\frac{a}{b}\right)^4} \cdots\cdots\cdots\cdots (2)$$

where:

a = width of plate; b = height of the plate; ρ = density of the plate.

Results and Discussion

Natural frequencies values obtained from three techniques, i.e ABAQUS, analytical and experimental methods have been presented in Table 1. Results showed that all the three techniques are in good agreement for results and the error percentage is less than 2% in all cases which validate the methods adapted for all sides simply supported delaminated carbon fibre reinforced polymer composite plate subjected to stacking sequences of (0/90/45/90), (0/45) and (0/90).

Table 1. Comparison of results from experimental, analytical and finite element methods subjected to all sides simply supported boundary conditions and without delamination

Boundary condition	Layers sequence	Method	Mode1, Hz	Mode 2, Hz	Mode 3, Hz	Mode 4, Hz
All sides simply supported	0/90/45/90	ABAQUS	444.7	1175.8	1175.8	1769.6
		Analytical	447.6	1182.3	1182.3	1790.6
		Experimental	425	1168	1179	1777
	0/45	ABAQUS	475.9	1191.9	1191.9	1892.9
		Analytical	482.4	1206	1206	1929.6
		Experimental	468	1189	1185	1895
	0/90	ABAQUS	421.6	1163.1	1163	1678.2
		Analytical	422.2	1165.8	1165.8	1688.8
		Experimental	409	1151	1160	1674

Table 2. Effect of delamination sizes on the natural frequencies of delaminated composite plate subjected to SSSS boundary condition.

Delamination area	Stacking sequence	Mode 1		Mode 2		Mode 3		Mode 4	
		Experimental	ABAQUS	Experimental	ABAQUS	Experimental	ABAQUS	Experimental	ABAQUS
6.25%	0/90/45/90	390	444.78	990	1175.7	1185	1175.7	1800	1769.6
25%		387	441	985	1174.9	1169	1174.9	1755	1769.6
56.25%		385	439.18	983	1172.4	1155	1172.4	1740	1769.4
6.25%	0/45	385	421.66	1100	1163	1170	1163	1701	1678.2
25%		384	411.66	1090	1162.1	1154	1162.1	1689	1678.2
56.25%		384	407.65	1080	1159.3	1146	1159.3	1669	1678
6.25%	0/90	379	475.96	1150	1191.7	1179	1191.7	1851	1892.9
25%		373	473.96	1140	1191	1167	1191	1837	1892.8
56.25%		371	470.95	1120	1188.7	1155	1188.7	1829	1892.7

Effect of delamination size. In the following paragraphs, we will study the effect of delamination size of 0%, 6.25%, 25% and 56.25% subjected to (SSSS) boundary condition. The Table 2 reveals that the on increase in delamination reduces the natural frequencies of carbon fibre reinforced composite plate for (0/90/45/90) for (SSSS) boundary conditions. Experimental and finite element results showed a declining trend with increase in delamination sizes. Maximum value of natural frequency is observed in case of (0/90/45/90) stacking sequence subjected to 6.25% delamination size. This value continue to decrease on an increase of delamination size. One can also see that the higher modes have larger difference than lower modes.

It has been observed that all sides simply supported boundary conditions subjected to all delaminated sizes, with stacking sequence of (0/90/45/90) has the highest values of natural frequencies. It may be interesting to see that natural frequencies are less affected in lower modes for all delaminated sizes.

Effect of stacking sequence. From Table 3, it is clear that Mode 1 is less affected in all sizes of delamination subjected to all stacking sequences. Mode 2 and Mode 3 have much lower difference in the values of natural frequencies in case of all sides simply supported boundary conditions. Maximum influence on the natural frequencies is observed. It is also observed that there is significant decrease in natural frequency with and without delamination.

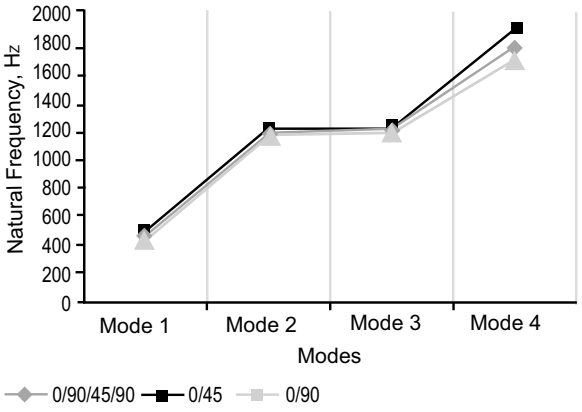

Fig. 3. Natural frequency of non-delaminated composite plate subjected to (SSSS) boundary condition.

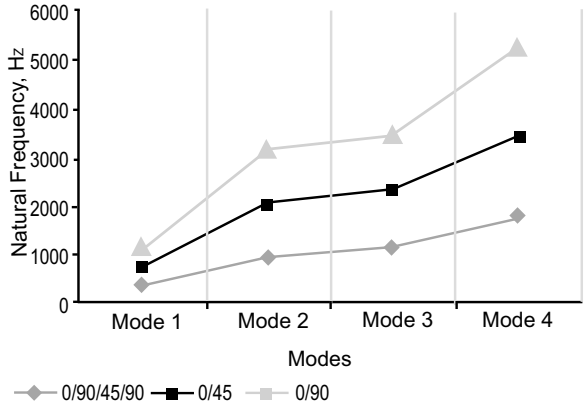

Fig. 4. Natural frequencies for first four Modes subjected to 6.25% delamination.

Table 3. Effect of stacking sequence for delaminated and non-delaminated composite plate.

Delamination area	Stacking sequence	Mode 1 experimental	Mode 2 experimental	Mode 3 experimental	Mode 4 experimental
0%		444.78	1175.8	1175.8	1769.6
6.25%	0/90/45/90	390	990	1185	1800
25%		385	985	1169	1755
56.25%		387	983	1155	1740
0.00%		475.96	1191.9	1191.9	1892.9
6.25%	0/45	385	1100	1170	1701
25%		383	1090	1154	1689
56.25%		384	1080	1146	1669
0.00%		421.66	1163.1	1163.1	1678.2
6.25%	0/90	379	1150	1179	1851
25%		381	1140	1167	1837
56.25%		380	1120	1155	1829

Highest values of natural frequencies are observed in the stacking sequence of 0/45 without delamination subjected to all four Modes as shown in Fig. 3 and it may be noted that stacking sequence of (0/90/45/90) has highest values in Mode 1 and stacking sequence of (0/90) has the highest values of natural frequencies as shown in Fig. 4.

Conclusion

It has been concluded that SSSS boundary constraint showed highest values of natural frequencies subjected to 0/90/45/90 stacking sequence for the delamination sizes of 0%, 6.25%, 25% and 56.25%. However lower values of natural frequencies were observed in lower modes. The combined analytical, experimental and finite element analyses of the nonlinear properties are believed to enhance the understanding of the vibration behaviour of the carbon fibre reinforced polymer composites. The results of this analysis can be considered as a base point for the safe, reliable design of composite structures with and without delamination. Based on the experimental, analytical and finite element methods, it has been observed that natural frequencies in case of all sides simply supported boundary conditions get inflected not only by the stacking sequences but also by the variation in delamination sizes.

Acknowledgment

Authors acknowledge the support from Department of Mechanical Engineering, Faculty of Engineering and Technology, International Islamic University, Islamabad.

Conflict of Interest. The authors declare no conflict of interest

References

Agarwal, B.D., Broutman, L.J., Chandrashekhara, K. 2017. *Analysis and Performance of Fibre Composites*. John Wiley & Sons.

Ardestani, M.M., Zhang, L., Liew, K. 2017. Isogeometric analysis of the effect of CNT orientation on the static and vibration behaviours of CNT-reinforced skew composite plates. *Computer Methods in Applied Mechanics and Engineering*, **317:** 341-379.

Bakis, C., Bank, L.C., Brown, V., Cosenza, E., Davalos, J., Lesko, J., Machida, A., Rizkalla, S., Triantafillou, T. 2002. Fiber-reinforced polymer composites for construction-state-of-the-art review. *Journal of Composites for Construction*, **6:** 73-87.

Brandinelli, L., Massabò, R. 2003. Free vibrations of delaminated beam-type structures with crack bridging. *Composite Structures*, **61:** 129-142.

Corum, J., Battiste, R., Liu, K., Ruggles, M. 2000. *Basic Properties of Reference Cross Ply Carbon-Fibre Composite*, Oak Ridge National Laboratory. ORNL/TM-2000.

Friedrich, K., Almajid, A.A. 2013. Manufacturing aspects of advanced polymer composites for automotive applications. *Applied Composite Materials*, **20:** 107-128.

Imran, M., Khana, R., Badshaha, S. 2019a. Investigating the effect of delamination size, stacking sequences and boundary conditions on the vibration properties of carbon fibre reinforced polymer composite. *Materials Research*, **22:** e20190478.

Imran, M., Khan, R., Badshah, S. 2019b. Finite element analysis to investigate the influence of delamination size, stacking sequence and boundary conditions on the vibration behavior of composite plate. *Iranian Journal of Materials Science & Engineering*, **16:** 11-21.

Imran, M., Badshah, S., Khan, R. 2019c. Vibration analysis of cracked composite laminated plate: a review. *Mehran University Research Journal of Engineering and Technology*, **38:** 705-716.

Imran, M., Khan, R., Badshah, S. 2018a. Vibration analysis of cracked composite laminated plate. *Pakistan Journal of Scientific & Industrial Research Series A: Physical Sciences*, **61:** 84-90.

Imran, M., Khan, R., Badshah, S. 2018b. A review on the effect of delamination on the performance of composite plate. *Pakistan Journal of Scientific & Industrial Research Series A: Physical Sciences*, **61:** 173-182.

Imran, M., Rafiullah, K., Badshah, S. 2018. Vibration analysis of cracked composite laminated plate and beam structures. *Romanian Journal of Acoustics and Vibration*, **15:** 3-13.

Imran, M. 2015. Pre-stress and free vibration optimization of composite ocean current turbine blade. *International Journal of Science, Engineering and Innovative Research*, **3:** 1-5.

Imran, M., Badshah, S. 2012. Vibration analysis of an ocean current turbine blade. *International Journal of Scientific and Engineering Research (USER)*,

3: 2229-5518.

Jadhav, V., Bhoomkar, D.M. 2016. Experimental and numerical FEM analysis of cracked composite cantilever beam by vibration techniques. *International Journal of Engineering Science*, 3347.

Juhász, Z., Turcsán, T., Tóth, T.B., Szekrényes, A. 2017. Sensitivity analysis for frequency based prediction of crack size in composite plates with through the width delamination. *International Journal of Damage Mechanics*: 1056789517709893.

Karim11, Z., Said, A., Nuawi, M., Ghani, J., Bahari, A. 2017. Value prediction of materials mechanical properties using I-kaz analysis method during impact test: experimental study. *International Journal of Applied Engineering Research*, **12:** 14608-14619.

Karsh, P.K., Mukhopadhyay, T., Dey, S. 2018. Spatial vulnerability analysis for the first ply failure strength of composite laminates including effect of delamination. *Composite Structures*, **184:** 554-567.

Kharghani, N., Guedes, S.C. 2016. Behaviour of composite laminates with embedded delaminations. *Composite Structures*, **150:** 226-239.

Kim, H.S., Chattopadhyay, A., Ghoshal, A. 2003. Dynamic analysis of composite laminates with multiple delamination using improved layerwise theory. *AIAA Journal*, **41:** 1771-1779.

Kim, H.-Y., Hwang, W. 2002. Effect of debonding on natural frequencies and frequency response functions of honeycomb sandwich beams. *Composite Structures*, **55:** 51-62.

Kumar, N., Mireja, S., Khandelwal, V., Arun, B., Manik, G. 2017. Light-weight high-strength hollow glass microspheres and bamboo fiber based hybrid polypropylene composite: a strength analysis and morphological study. *Composites Part B: Engineering*, **109:** 277-285.

Lee, S., Park, T., Voyiadjis, G.Z. 2002. Free vibration analysis of axially compressed laminated composite beam-columns with multiple delaminations. Composites Part B: Engineering, **33:** 605-617.

Luo, S.-N., Yi-Ming, F., Zhi-Yuan, C. 2004. Non-linear vibration of composite beams with an arbitrary delamination. *Journal of Sound and Vibration*, **271:** 535-545.

Mishra, I., Sahu, S.K. 2012. An experimental approach to free vibration response of woven fibre composite plates under free-free boundary condition. *International Journal of Advanced Technology in Civil Engineering*, **1:** 67-72.

Mohammed, D. 2017. Effect of fibre angles on dynamic response of cantilever composite beams. *ZANCO Journal of Pure and Applied Sciences*, **29:** 157-163.

Nanda, N., Sahu, S.K. 2012. Free vibration analysis of delaminated composite shells using different shell theories. *International Journal of Pressure Vessels and Piping*, **98:** 111-118.

Oliveri, V., Milazzo, A. 2018. A Rayleigh-Ritz approach for postbuckling analysis of variable angle tow composite stiffened panels. *Computers & Structures*, **196:** 263-276.

Saghafi, H., Ghaffarian, S., Salimi-Majd, D., Saghafi, H. 2017. Investigation of interleaf sequence effects on impact delamination of nano-modified woven composite laminates using cohesive zone model. *Composite Structures*, **166:** 49-56.

Sayyad, A.S., Ghugal, Y.M. 2017. Bending, buckling and free vibration of laminated composite and sandwich beams: a critical review of literature. *Composite Structures*, **171:** 486-504.

Shao, D., Hu, S., Wang, Q., Pang, F. 2017. Free vibration of refined higher-order shear deformation composite laminated beams with general boundary conditions. *Composites Part B: Engineering*, **108:** 75-90.

Shu, D., Della, C.N. 2004. Vibrations of multiple delaminated beams. *Composite Structures*, **64:** 467-477.

Thornburgh, R., Chattopadhyay, A. 2003. 44th AIAA/ ASME/ASCE/AHS/ASC Structures, *Structural Dynamics, and Materials Conference*, 1773 pp.

Thornburgh, R., Chattopadhyay, A. 2001. Unified approach to modeling matrix cracking and delamination in laminated composite structures. *AIAA Journal*, **39:** 153-160.

Tsongas, K., Tzetzis, D., Mansour, G. 2017. Mechanical and vibration isolation behaviour of acrylonitrile-butadiene rubber/multi-walled carbon nanotube composite machine mounts. Plastics, *Rubber and Composites*, **46:** 458-468.

Venkate G.C., Rajanna, N., Udupa, N.G.S. 2017. Investigating the effects of delamination location and size on the vibration behaviour of laminated composite beams. *Materials Today: Proceedings*, **4:** 10944-10951.

Vescovini, R., Dozio, L., D'Ottavio, M., Polit, O. 2018.

On the application of the Ritz Method to free vibration and buckling analysis of highly anisotropic plates. *Composite Structures*, **192:** 460-474.

Vo, T.P., Thai, H.-T., Aydogdu, M. 2017. Free vibration of axially loaded composite beams using a four-unknown shear and normal deformation theory. *Composite Structures*, **178:** 406-414.

Yam, L.H., Wei, Z., Cheng, L., Wong, W.O. 2004. Numerical analysis of multi-layer composite plates with internal delamination. *Computers & Structures*, **82:** 627-637.

Yelve, N.P., Mitra, M., Mujumdar, P. 2017. Detection of delamination in composite laminates using Lamb wave based nonlinear method. *Composite Structures*, **159:** 257-266.

Zhang, Z., He, M., Liu, A., Singh, H.K., Ramakrishnan, K.R., Hui, D., Shankar, K., Morozov, E.V. 2018. Vibration-based assessment of delaminations in FRP composite plates. *Composites Part B: Engineering*, **144:** 254-266.

Pak. j. sci. ind. res. Ser. A: phys. sci. 2021 **64A**(1) 84-96

Review

Nanocarriers for the Oral Delivery of Drugs With Special Focus on Porous Silicon: A Review

Asad Muhammad Azama[a]* and Tahir Iqbal Awan[b]
[a]Department of Physics, University of Gujrat, Pakistan
[b]Department of Physics, Umeå University, SE-901 87 Umeå, Sweden

(received August 7, 2018; revised June 31, 2019; accepted June 3, 2019)

Abstract. The focus concerning controlled drug release requires the growth of appropriate drug carriers that could move adequate amount of the drug to injured area with controlled and sustained manner. A variety of nanoparticles including magnetic nanoparticles, the staes, liposomes, polymers dendrimers, solid lipid nanoparticles (SLN) and porous silicon have been investigated as drug carriers in drug delivery cases. Nanocarriers have achieved significant importance in the stabilization of proteins and peptides, anti-cancer drug camptothecin (CPT) and bone tissue engineering offering improved buccal access and protection according to the desired function. Moreover, tailored formulation along with functionalization and bio-compatibility has importance in fabrication of nanoparticles for proteins or peptides *via* oral delivery systems, which has advantage over parenteric delivery systems because of their comfort running and observance to treatment. The review summarizes interesting approaches on existing publications for drugs such as proteins or peptides carrier nanoparticles with special focus on porous silicon for delivery systems. Fabricatioan of nanoparticles e.g. porous silicon nanocarriers for oral delivery, advantages and disadvantages, prospective use of porous silicon in drug delivery systems will be addressed.

Keywords: drug carriers, functionalization, porous silicon, electrochemical etch method, applications of porous silicon

Introduction

An extensive class of drugs such as proteins or peptides is considered as curative drugs for the healing and administration of numerous diseases. The history of biological drugs is early known when Food and Drug Administration (FDA) of USA had accepted first re-combinant human insulin in 1982 (Schiffter *et al*., 2011).

Currently, several bioactive drugs are under clinical examination and more or less than 35 have been licensed for commercialization by FDA. Parenteral administration route is still significantly in use due to size obstacle, stability and low bioavailability issues in gastrointestinal region in spite of having several functional protein or peptide bio-technological drugs. Parenteral route is hurting, having possibility of contamination for the patients plus requires presence of medical personnel for its delivery (Prantera *et al*., 1997). Moreover, parenteral route is costly and requires method of preparation under hygienic condition, while oral route is preferable due to friendly falling in line to treatment (Harloff-Helleberg *et al*., 2017). The achievements of nano technological materials opened several ways of drug conjugation with different nanoparticles. Due to easy size modification and surface enhancement properties of nanomaterials, they are considered as smart drug nanocarriers. The objective of smart drug nanocarriers is that drug pursuing target tissues or organs release with slow rate or proper rate of action and will not move freely during blood circulation. Premeditated drug nanocarriers or stimuli-responsive drugs mechanism towards exogenous or endogenous stimulus is illustrated in Fig. 1. Endogenous parameters (disease pathological) such as small biomolecules, redox gradient, pH- value, glucose, hormone level, enzyme concentration and exogenous parameters like magnetic field, temperature, electric or high energy pulse, light and ultrasound can be in use for controlled release of drugs over the target (Kelley *et al*., 2013; Mura *et al*., 2013). Oral route types comprise sublingual, gastrointestinal, gingival and buccal routes. Drug release methods can be modified to definite function and unclear target for absorption according to the prescriptions of pharmaco-kinetics of specific drug. Buccal delivery is suitable when unstable

*Author for correspondence; E-mail: asadpu2003@gmail.com

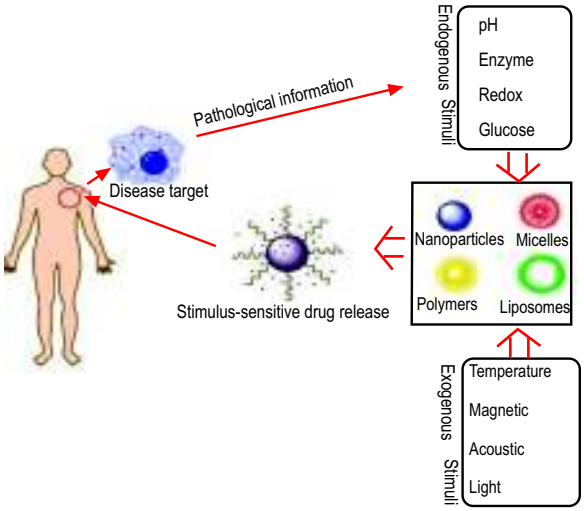

Fig. 1. Schematic illustration for stimulus drug delivery mechanism (Nagal *et al*., 2013).

carried drugs at severe pH-value subject to undergo enzymatic absorption or metabolization of inactive products.

Gastrointestinal route is used when drug nanocarriers are stable with higher bio-availability. Numerous methods have been used to shield therapeutic drugs with nanocarriers in order to increase immovability and diffusion across absorption in gastrointestinal route. Encapsulation of therapeutic drugs within nanocarriers has revealed improved bio-compatibility. Size of the nanoparticles is identified to be 10 to 100 nm and can be ordered as alone or incorporated with a variety of nanomaterials such as synthetic polymers, metals, lipids, proteins and polysaccharides (Maruthi *et al*., 2011). The designing of nanoparticles for drug delivery systems requires controlled size, toxicity and surface properties against release of active drugs at therapeutically optimal rate. Nanostructures reveal excellent biological and physico-chemical properties with an improved ability to cross tissue barrier and reliable with cell environment (Nagal *et al*., 2013). Mesoporous silica nanocarriers have been rigorously recommended for stable drug delivery systems, biomarking, gene transport, biosignal probing and several other biomedical applications due to its excellent properties such as bio-compatibility, bio-degradability, high surface area, increased pore volume, tunable pore structure and physico-chemical stability (Patel *et al*., 2014). However, 10 to 100 nm size of nanoparticles is not acknowledged by the Royal Society and Royal Academy of Engineering (RSRE) 2004. According to RSRE, the biological properties do not depend on size variation (Jong *et al*., 2008). Modern delivery systems (frequently used proteins or peptides *via* oral route) for therapeutic purposes have shown a greater impact economically and are allocated a budget of US$ 479,752 million for year 2024 (Global Biologics Market *et al*., 2017). Function of nanoparticles in drug delivery tasks have major advantages like mucoadhesion, increased permeability round epithelia absorption, increased surface area, good functionalization, accuracy over target delivery, affinity to intestinal cells will be further discussion topics in this article. Several upto date examples of drug nanocarrier's e.g. porous silicon nano or meso particles for protein or peptide drugs and main results that were obtained will be addressed in this review article critically.

Characterization methods and characteristics for encapsulation of nanocarriers and drug interaction. Polymer nanoparticles have a collection of properties with controlled and tuned circumstances which are assigned to respond drug targeting. Nanoparticles as drug carriers must be in possession of good physical characteristics such as drug loading efficiency, polydispersity indicator and size, surface carrier behaviour with controlled and favourable conditions (Global Biologics Market *et al*., 2017).

Scanning electron microscopy (SEM), atomic force microscopy (AFM), transmission electron microscopy (TEM), dynamic light scattering (DLS), Fourier-transform infrared (FTIR), Raman spectroscopy, X-ray photoelectron spectroscopy (XPS) and energy dispersive spectroscopy (EDS) are commonly used techniques for the measurement of nanoparticles size, presence of agglomerates, rate of action and surface morphology. Zeta-potential, a central task for the idea of *in vivo* performance of nanocarriers when set on with cellular arrangement is measured by electrophoretic light scattering (ELS). Synthesis of nanoparticles is an essential requirement for specific tasks and remains a problem for researchers worldwide (Lin *et al*., 2014). Specific physico-chemical properties such as morphology, aggregation, mean size, polydispersity index (size distribution), surface properties, drug content, conformational effects, concentration and drug discharge, are commonly examined during characterization (Crucho *et al*., 2017).

Formulation of a certain nanoparticle have strong dependence on the targeting application, therefore quite

difficult to recognize nanoparticle as a standard tool but it must be proven to predict *in vivo* conditions, toxicity and guarantee effectiveness. Researchers have proven that shape and size of nanoparticles have a strong role in loading and interaction with biological interfaces (Banerjee *et al*., 2016). Usually, it is the supposition that nanoparticles with spherical shape are taken as the most appropriate drug carriers is not a true fact in all situations. In order to modify size, shape and surface properties of nanoparticles for oral drug carrier, researchers manufactured polystyrene nanoparticles of various shapes like rod- shaped, sphere, flakes and disc-shaped of sizes 500, 200, and 50 nm respectively. Researchers tested the rate of action, cellular transport or immovability and uptake capacities across certain drugs such as Caco-2 Caco-2/HT29 and Caco-2/HT29/Raji-B triple culture. Confocal microscopy confirmed that drugs Caco-2 and Caco-2/HT-29 cells have increased capacity to load when particle size was small (Lynch *et al*., 2008). Knowledge about drug and nanocarries interaction e.g. formulation and association of the drug meso/nano carriers and drug release time of the nanoparticle has much importance during drug delivery administration. Drugs like proteins with increased association rate constants and increased concentration are initially exist at the nanocarrier surface, but after a short time nanocarrier structure may act as proteins of higher affinity, slower exchange rate and lower concentration (Lynch *et al*., 2008). Interactions such as hydrophobic, chemical and electrostatic (regarding protein adsorption) play important roles. According to various studies, some proteins show strong adsorption and release rate to the nanocarriers while others have weak residence times and weak affinities (Lynch *et al*., 2008). Polymers due to their outstanding biocompatibility and biodegradability, such as polylactic acid (PLA), amphiphilic copolymer polyethylene glycol (PEG), chitosan, polylactide co-glycolide (PLGA), gelatin, starch polycaprolactone (PCL) and alginate are generally used for manufacturing nanoparticles (Patel *et al*., 2014; Giovino *et al*., 2012; Lynch *et al*., 2008; Mundargi *et al*., 2008; Rawat *et al*., 2006). Solvents such as acetone, dichloromethane, ethyl acetate, acidic solutions, diffusing agents like cyclo-dextrins and phospho- lipids along with surfactants such as polyvinyle alcohol and polyssorbate are commonly preferred for the synthesis of nanocarriers (Lai *et al*., 2014). The preparation of nanoparticles must be done according to the fulfillment of certain properties such as drug loading and drug release time, association efficiency, zeta potential, size of nanoparticles, surface properties i.e. charge and shape, the degree of bio-compatibility, bio-degradability, toxicity, and the antigenicity of the host (Maruthi *et al*., 2011; Mohanraj *et al*., 2006).

Functionalization of nanoparticles as drug carriers. For drugs such as protein or peptide delivery, solid lipid nanoparticles (SLN), porous silicon and polymeric nanocarriers have been most frequently explored (Patel *et al*., 2014). Solid lipid nanoparticles (SLN) have achieved commercial as well as scientific interest as therapeutic drug delivery carriers recently. SLN have shown proved advantages over controlled drug release and functionalization to target (diseased organs or tissues) accurately. Functionalization of the surface chemistry helps the nanopartile to achieve the specific targeted organ. For instance, with the help of chitosan as a coating agent e.g. non-covalent approach, Solid lipid nanoparticles (SLN), porous silicon nanoparticles and polylactide-coglycolide (PLGA) can be modified and functionalized to have intestinal cells as target (Araujo *et al*., 2014; Mura *et al*., 2013). Solid lipid nanoparticles (SLN) were functionalized by coating chitosan on the surface of solid lipid nanoparticles for oral delivery of insulin (Mura *et al*., 2014). Under comparison with uncoated solid lipid nanoparticles (SLN), chitosan coated- SLN have successfully showed improved insulin across drugs such as Caco-2 and Caco-2/HT29. Under vitro assay, relative pharmacological conditions such as relative pharmacological bio-availabilities were of 8% for insulin carried by uncoated-SLN and 17% for insulin carried by chitosan coated SLN when hypoglycemic effect in diabetic mice was tested. It was found that high effectiveness of insulin loaded with chitosan- coated solid lipid nanoparticles was linked due to positively increased zeta potential and rigid junction i.e.(disorderly reaction of chitosan) (Kelley *et al*., 2013; Cano-Cebrian *et al*., 2005). Fluorescent marker was used to label insulin in order to verify increased adsorption by intestinal cells inside the intestinal wall. It is important to note that increased positive zeta potential increases both mucoadhesion and contact with the help of non-covalent functionalization of nanocarriers with chitosan, while covalent functionalization is stable and extra valuable with distinct biological properties as compared to non-covalent functionalization (Araújo *et al*., 2017; Hermanson *et al*., 2009). Functionalization of nanocarriers is an important tool to achieve targeting

delivery and increased permeability. Without functionalization of nanocarriers, it is difficult to investigate functionalization rate of individual carrier which is covalently bonded. Moreover, it is noted that non-covalent functionalization as well as the gastrointestinal tract may perhaps lose appearance as it is usually weaker than covalent functionalization (Araújo *et al*., 2009). Functionalization of nanocarriers take part in increasing residence time of loaded drug and drug released amount from nanocarriers according to redox reaction or specified pH-value (Huo *et al*., 2014; Colombo *et al*., 2009). Therefore, functionalization methods as well as functionalizing agents are important factors for the functionalization of nanocarriers. Solid lipid nanoparticles (SLN) can be synthesized with the help of biocompatible lipids that have physiological body melting temperature round about 37 °C. Cetyl palmitate, beeswax and carnauba wax lipids utilized for the synthesis of solid lipid nanoparticles are digested by intestinal juices and have higher melting temperature as compared to physiological body temperature (Madureira *et al*., 2016; Mundargi *et al*., 2011). Studies have shown that solid lipid nanoparticles are proved more protective and sensitive due to chemical, thermal and oxidative degradation behavior (Righeschi *et al*., 2016). Moreover, solid lipid nanoparticles are low cost with excellent properties such as conjugation of hydrophilic and lipophilic compounds, avoidance of using organic solvents, better functionalization for targeted delivery than biodegradable polymers and phosphor lipids. Hence, solid lipid nanoparticles have been suggested as an excellent drug carrier designed for several drug delivery systems (Aditya *et al*., 2015). While polymeric nanocarriers with the help of different production methods can be designed as nanocapsules or nanospheres according to uniform distribution of bioactive drugs within a matrix or membrane (Khalid *et al*., 2017).

Synthesis of nanoparticles. Chemical and physico-chemical methods are major categories of nanocarriers fabrication intending the encapsulation and release of bioactive drugs such as protein or peptides (Iqbal *et al*., 2015) Polymerization techniques like emulsion polymerization, interfacial polymerization and mixed-emulsion polymerization fall in chemical methods category, while numerous emulsion techniques such as spray drying, solvent diffusion emulsion and bilayer emulsion fall in physico-chemical methods (Kumari *et al*., 2010; Soppimath *et al*., 2001).

Emulsion polymerization technique is further subdivided into single and double emulsion techniques which are trouble-free and reliable techniques for the synthesis of nanoparticles (Danhier *et al*., 2012). Ionic solvent diffusion and spontaneous emulsification processes contains miscible solvent and an immiscible water organic solvent in the form of grease phase and create an interfacial instability in phases due to which production of small particles takes place. Size of particles is dependent on the concentration of water solvent. Hydrophobic and hydrophilic drugs can be treated by both solvent evaporation and diffusion processes (Mohanraj *et al*., 2006). Simple emulsion processes (water/oil) are valuable carrier routes for the trap of lipophilic molecules. It was noted that polymer concentration, type, stabilizer concentration and homogenizer speed affect particle size. Nanoparticles produced by this technique are not considered suitable for majority of drugs as carriers due to their low association or binding efficiency with hydrophilic molecules (Chung *et al*., 2011; Mohanraj *et al*., 2006; Kwon *et al*., 2001). Interfacial emulsion techniques are more multifarious as compared to uncomplicated emulsions because of existence of nanocacrriers having extra carriers within the medium. Interfacial emulsions (Water/oil/water) are valuable for the amalgamation of lipophilic as well as hydrophilic molecules collectively and are selected for the trap of bioactive drugs such as proteins or peptides (Iqbal *et al*., 2015). Interfacial emulsion technique has certain drawbacks such as high polydispersity index, leakage of bioactive molecules and is a two step production technique. Particle reproduction in non-wetting profile has also been utilized for production of nanoparticles (Mohanraj *et al*., 2006).

In the absence of organic solvents, Interfacial emulsion (solid/ oil/ water) is a reasonable approach (Bilati *et al*., 2005). Nano-precipitation is an ideal method to produce small sized nanoparticles for drugs to suffer hydrolytic degradation due to avoidance of water. Also, nano-precipitation method has drawbacks like high shear stress and poor encapsulation (Bilati *et al*., 2005). Protein ion coupling is an appropriate stable technique used for nano entrapping drugs at pH values lying below isoelectric position. Ion coupling involves the existence of a surfactant and excites an increased hydrophobicity which causes excellent encapsulation efficiency (Meyer *et al*., 1998; Quintanar-Guerrero *et al*., 1997). Finally, buccal delivery of drugs offer stability as well as protection against enzymatic degradation and have

general utility and encapsulation strength into mucoadhesive films, strips, hydrogels, scaffolds. Mucoadhesive films are usually prepared by solvent casting method (Castro *et al*., 2015).

Electrochemical etching method. Formation of porous silicon by electrochemical etching method is illustrated in Fig. 2.

Porous Si is an artifact of an electrochemical anodization of Si wafers in single crystalline form in a hydrofluoric acid electrolyte solution. The factors such as current density, the electrolyte concentration, the type and concentration of dopant and the crystalline orientation of the wafer help in variation of size (macro, meso and micropores) and pore morphology. Pore sizes from 1 nm to a few microns range can be prepared (Canham *et al*., 1994). The mechanism of pore formation is generally a combination of electronic and chemical factors (Zhang *et al*., 2004). The type of dopant establishes the availability of valence band holes in the original silicon wafer which are the key oxidizing agents in the reaction shown in Fig. 2. Configuration of dopants to morphology of host on the basis of type and concentration can be classified into four groups namely p-type, n-type, highly doped p- type and highly doped n-type. "Highly doped," corresponds to dopant levels, where conductivity performance of the material is more metallic as compared to semiconducting. "Moderate doping" corresponds to n-type silicon wafers where barring of valence band holes from the space charge region determines the pore diameter. Quantum well effects are considered to handle pore size moderately in p-doped materials. Reaction for both dopant types is crystal face selective which allows pores to propagate primarily in the <100> direction of the single crystal. An electrolyte containing hydrofluoric acid is the base

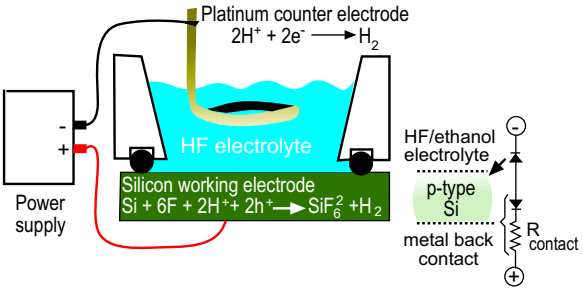

Fig. 2. Schematic illustration of the etch cell for the synthesis of porous silicon (Canham *et al*., 1994).

of electrochemical reaction. Anode current oxidizes a surface silicon atom which is further reacted by fluoride. The whole process involves four electrons of oxidation from which two are supplied from current source and other two electrons come from reduction reaction of proton in SiF_2 species. Pores are formed when Si atoms are removed in the form of Sif_4 in reaction with two corresponding F-atoms in solution to from SiF_6^{-2}. The process of growing porous Si layer i.e. porosity is found to be proportional to applied current density and has range between 40 to 80%. During etching process, morphology of pores remains constant and form only at the Si and porous Si interface. However, the applied current density can change the porosity of a growing layer e.g. In photonic crystals having a stack of layers with discontinuous refractive index can be fabricated by periodically adjusting the current density during an etch (Berger *et al*., 1997; Vincent *et al*., 1994). Porous Si has unique property to tune pore sizes and volumes during electrochemical etching process which is a positive impact of porous Si in drug delivery applications. Porous materials other than Si require complicated design to maintain pore size and volume and still have drawback of spanning pore sizes. Larger pores can be formed with larger current density and larger pores are required to form when sizable molecules or drugs are encapsulated within pores. Porosity and pore size are important factors for determining degradation rates of porous Si host matrix and are basis for loading drugs (Anderson *et al*., 2003). Smaller pores with large surface area have more capacity for attack of aqueous media and yield greater dissolution rates with controlled degradation rates of host matrix. Porous Si *in vivo* applications is desired to prepare in the form of particles where porous layer can be removed from Si substrate with the help of a procedure called electropolishing or lift-off. The etching electrolyte is substituted with lower concentration of hydrofluoric acid and a current pulse is applied for short time. Other conventional methods such as lithography and micro droplet patterning can be formulated if particles require more uniform shapes (Meade *et al*., 2007).

Chemistry of porous silicon. Silicon is considered as connective and bone tissue trace element and health of tissue strongly depends on silicon. Chemical species like silane (SiH_4) and oxides of silicon represent toxicity of porous silicon. Si-H, SiH_2 and SiH_3 are surface species of porous silicon that like to convert into silane (Meade *et al*., 2004; Jay *et al*., 2000). Silane is toxic

and chemically reactive when inhaled, while other species such as silicon hydrides of porous silicon have oxidizing ability in aqueous solution. Thermodynamically, silicon itself has unstable oxidation behaviour and water provides sufficient oxidizing potential to precede a spontaneous reaction. The following three equations represent oxidized chemical species of porous silicon.

$$SiH_4 + 2H_2O \rightarrow SiO_2 + 4H_2 \quad \text{.....1}$$

$$Si + O_2 + \rightarrow SiO_2 \quad \text{.....2}$$

$$SiO_2 + 2H_2O \rightarrow Si(OH)_4 \quad \text{.....3}$$

The act of SiO_2 as well as Si-H when absorbed in hydrofluoric acid solutions causes suspension of silicon momentarily slow due to its extremely porous structure. Reasonably large quantity of silicon having species from oxidized porous silicon can be obtained from spontaneous aqueous solution shortly. Soluble silicon dioxide contains different silicic acidic SiO_4^{-4} ions as the fundamental constituent and these oxides are found to be toxic in doses (Lai *et al.,* 2005; Kawanabe *et al.,* 1992). The problem with silica based drug carriers is the increased rate of degradation and desorption. The contribution of Bayliss, Canham and other researchers determined relatively low toxic behavior of porous silicon in various cellular and live animal cases (Chin *et al*., 2001; Bayliss *et al*., 1997). The by products of porous silicon showing easy degradation and low toxicity have opened new doors in controlled drug delivery systems for researchers.

Porous silicon with controlled release of drugs. Controlled as well as confined release of peptides or proteins is thought to be key functions for the elimination of potential side effects and tends to increase the efficacy (Wise *et al*., 2000). Due to certain excellent properties such as increased porosity, low toxicity and favourable surface chemistry of porous silicon and porous SiO_2 have grown them as potential candidate or fundamental craft for diagnostics, therapeutics and several other types of drugs as carriers. Numerous methodologies of loading proteins or peptides into porous silicon host have been experimented and can be characterized into covalent binding, adsorption and physical traping. Covalent binding method is useful to link bimolecular capture directly into inner pore walls of porous silicon for biosensing applications as well as for drug carrier encapsulation (Schwartz *et al*., 2005). It was found that bimolecular attachment *via* silicon-carbon bonds is more stable than silicon-oxygen bonds because of susceptibility of silicon- oxygen species against nucleophilic beat. The flexibility of the hydrosilylation response was early famous in the history of surface chemistry of silicon to prepare functional porous silicon (Buriak *et al*., 2002). The most common step was graphitization of an organic molecule like carboxylic species on terminal alkene (Dorvee *et al*., 2008; Boukherroub *et al*., 2002). If the physical trapping of drugs is relatively robust then locking or encapsulation can be occurred due to oxidation of porous silicon host matrix. Trapping or locking is an excellent property of porous silicon when porous silicon is oxidized to SiO_2 due to which volume expansion contain additional oxygen atoms and shrink the pores and locked or trapped the drugs in pores. Similarly, iron oxide (Fe_3O_4) nanocarriers have been overloaded and accumulated with the porous silicon nanostructure using aqueous ammonia to stimulate oxidation (Dorvee *et al*., 2004).

Composites of porous silicon. Composites have gained strong attention of researchers for drug delivery devices due to advantageous physical and chemical characteristics as individual constituents are deficient of these properties. Composite design preference of nanostructure composites have greatly expanded in the last few years (Gurny *et al*., 2006). The nanostructure template has proven as a versatile method to create periodic nanostructures during synthesis of materials. Templates such as zeolites, crystalline colloidal arrays and micro or mesoporous membranes have been used and numerous mechanical, electronic and optical structures have been created or formed. Porous silicon is a potential candidate for applying as a medium due to good tuneability of the porosity and regular pore size. Moreover, one, two and three dimensional photonic crystals are being manufactured from porous silicon. Porous silicon composites are proving better with improved mechanical stability and excellent control rate over drug release mechanism for an oral delivery case. Polymers such as polystyrene, polycaprolactone, poly (N-isotropyl acrylamide), polydimethyl siloxane, zein (a kind of biopolymer obtained from maize) and polylactide have been encapsulated or incorporated into porous silicon matrix. Oxidation of porous silicon from a polymer or biopolymer can be completed *via* chemical dissolution method with the help of aqueous potassium hydroxide [KOH] and hydrofluoric acid solutions respectively from which an isolated porous composite

structure with excellent optical properties can be obtained. The concept of porous silicon and polymer composite was primarily known in 1990 (Koshida *et al*., 1993). Two techniques have been demonstrated, first the polymer is fabricated inside the porous silicon matrix and secondly melts or solution casting processes are used to inculcate polymer into the porous silicon matrix (Li *et al*., 2006). Porous silicon formed an excellent matrix of nanocrystalline domains but one drawback is its mechanical stability in applications where porous silicon is subjected to mechanical stress or thermally in use. Chemical encapsulation of porous silicon need correct choice of polymerization conditions.

Importance of optical properties of porous silicon *in vivo* monitoring. Some drug carriers provide information regarding drug loading and its release time on self based report and for others, it is important to investigate a new time for next dose. The engineered optical characteristics of porous silicon have ability to detect such investigations *in vivo* conditions. The production of porous silicon with modified refractive index has measured drug loading capacity from reflection spectrum of the nanostructure. From optical spectrum of molecular functionalized encapsulation with porous silicon, drug content as well as drug degradation can be measured (Chan *et al*., 2000; Lin *et al*., 1997). Characterization and quantification of drug loading or release time can be assessed under *ex vivo* case accordingly. Description and interpretation of optical interference spectra can be studied elsewhere, a brief overview will be presented here. It is evident from studies that refractive index can be linked to the mass as well as composition of a nanostructure (thin film or sensor). The reflectivity spectra of a thin film (air-porous silicon or porous silicon-crystalline) shown in Fig. 3 displays Fabry-Perot interference fringes.

The refractive index and thickness of the film can be find out using Fast Fourier Transform (FFT) from constructive and destructive interference of reflected light at the borders of interface. Shifts and refractive index in the reflectivity spectra present relationship with composition and mass loading of film according to Bruggeman effective medium model (Janshoff *et al*., 1998; Bohren *et al*., 1983). A shift in the reflectivity spectra also provides information about oxidation mechanism of porous silicon. Porous silicon and oxidized porous silicon have refractive index approximately 2.1 and 1.6 (Ouyang *et al*., 2005). Optical structures such as Bragg stack, micro activity, rugate and Fabry-Perot

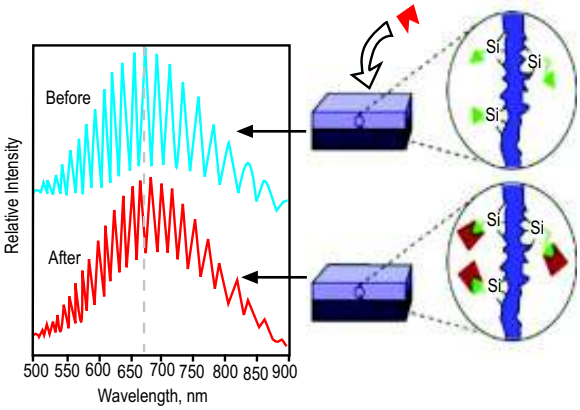

Fig. 3. Schematic illustration of reflectivity spectrum of single layered porous silicon upon encapsulation of bioactive molecular species into the host porous silicon matrix (Li *et al*., 2003).

have shown similar trends of sensitivity when analyzed in provisions of substrate concentration verses spectral shift at the pores of optical structure (Ouyang *et al*., 2005).

Monitoring a porous silicon fixture *in vivo*. Optical interference spectrum obtained from a diode laser interferometer or a CCD (charge coupled device) spectrometer can be used to measure drug loading capacity of porous silicon nanoparticles (Gao *et al*., 2002; Gao *et al*., 2000), e.g., monitoring of porous silicon carriers for ocular drug delivery in the vitreous of rabbit eyes shown in Fig. 4 (Li *et al*., 2003).

Drug release or dissolution of the particles causes deviation into the refractive index of the porous silicon film that is analyzed as a wavelength shift in the reflectivity spectra. Clinically, this colour shift change can be analyzed by spectroscopy or fundus camera in the living eye. Deoxi carboxylic nucleic acid (DNA), dexamethasone (Anglin *et al*., 2004), caffeine, bovine serum albumin (Collins *et al*., 2002) and several other molecules has been found using this technique. Detection of optical interferometric test and high surface area results high sensitivities as compared to surface plasmon resonance method for several systems. The optical spectrum of porous silicon for human tissue having thickness up to 1 mm can be easily detected and have shown the feasibility as *in vivo* self reporting medium (Li *et al*., 2003). The optical technique is significantly important for controlling intraocular drug release activity

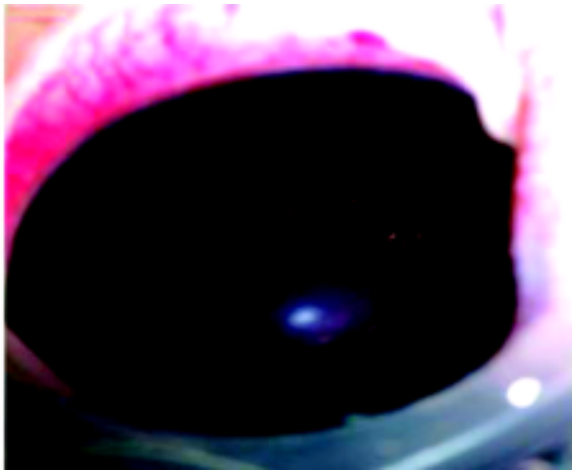

Fig. 4. Photograph showing presence of porous silicon micro carriers in the eye of a rabbit (Li *et al*., 2013).

in composite films or by using porous silicon carriers as illustrated in Fig. 5.

The microparticles of porous silicon shown in Figure 5 have been reported as self-reporting drug carriers for certain diseases like age related macular collapse where long durability is the initial requirement in intraocular drug delivery case (Park *et al*., 2006).

Applications of porous silicon in medical science. The efficacy and bio-compatibility of different types of porous silicon have been investigated for medical purposes and clinical trials are ongoing. The encapsulation of anti-cancer therapeutics (Vaccari *et al*., 2006; Coffer *et al*., 2003) anti-inflamatory agents (Salonen *et al*., 2005; Li *et al*., 2003) analgesics and corresponding medicinally drugs has been demonstrated. Porous silicon as an oral drug carrier has been investigated for a dietary supplement of silicon (Canham *et al*., 2007). Porous silicon drug carriers have opted different forms in order to take drug according to specific function such as particles, films, microneedls and flakes in the form of composite materials (Segal *et al*., 2007; Canham *et al*., 1994). Due to its easy encapsulation and bio-compatibility microns as well as nanoparticles of porous silicon have been utilized in biomedical applications. Oxides of porous silicon as well as porous silicon as a brachytherapy device have been used by porous Si media,Inc for diagnosing cancer. They have taken porous silicon particles of approximated size 20ìm as implants containing radioactive 32p to diagnose tumor. Elemental transmutation method was used to load radioactive isotope in the porous silicon and induced *via* high energy neutrons exposure from a nuclear reactor. Silicon implants hydrolysis to silicic acid and absorbs in body after the radiation dose delivery. Physiological conditions were maintained according to level of toxicity of silicic acid (Lai *et al*., 2005; Kawanabe *et al*., 1992). Anticancer drugs have been successfully encapsulated into porous silicon, for example, calcium phosphate and porous silicon have been taken as carriers for eis-platin in simulated body fluid (Li *et al*., 1998). Porous silicon films loaded with doxorubicin have shown toxic behavior towards adenocarcinoma cell lines of human colon. Singlet oxygen can be formed when photoexcitation of quantum confined silicon nanostructures encapsulated with aqueous aerated medium has been categorized. The harmless toxicity of silicic acid has achieved priority over molecular (porphrin-based) sensitizers for photodynamic therapy (Fujii *et al*., 2006; Fujii *et al*., 2004). Particles as drug carriers have dependence on their size, for example, quantity of drug encapsulated with porous silicon microparticle is increased because of its high pore volume. Singlet porous silicon cubic carrier with approximated size 10 ìm and porosity of 80 % stored a maximum 0.8 pL (picoliter) of free volume (Thomas *et al*., 2006). The incorporation of porous silicon with super paramagnetic iron oxide structures has been reported for magnetic resonance imaging (MRI) and remote radio frequency (RF) heating (Park *et al*., 2006). Salonen along with his coworkers have explored drug

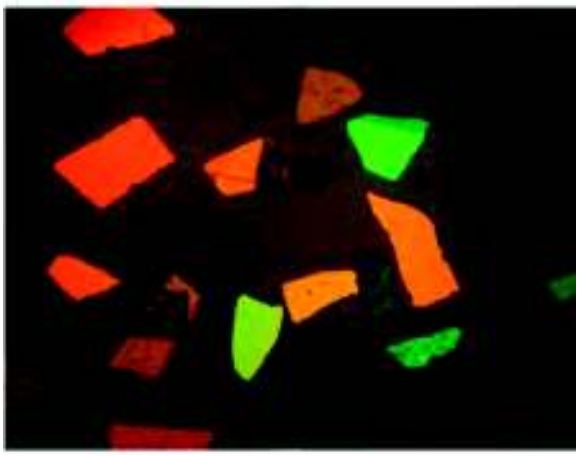

Fig. 5. Porous silicon microcarriers image taken with the help of light microscope (Li *et al*., 2003).

release mechanism of porous silicon microparticles for oral delivery application.

Future prospects and conclusion.

Natural molecules such as proteins have potential applications in biomedicine and may considered as inherent protein biorecognition, target agent and utilized in therapies (Pelegri- O'Day *et al*., 2014). Proteins have been used for the fabrication of nanocarriers due to their ease of surface adaptation, biodegradability and metabolization. Excellent challenges need to be modified in order to prepare protein or peptide therapeutic solutions, an effective delivery carrier and suitable techniques to overcome the formulation. Unconventional delivery systems and formulation techniques will be implemented in oral drug delivery systems in future as predicted by researchers. For example, three dimensional printing and layering precision (nanometer) of oral delivery of drugs as a dozage agent to picoliter (Goyanes *et al*., 2015). Three dimensional printings have not only provided more convenient predictable delivery schemes but also in research of approximately 100% efficient homogeneous nanocarriers.

Therapeutic categorization may realize as a short term reality due to fast and easy 3D printing production methods. Most favorable usage of 3D printing production does not involve use of organic solvents in fabrication of drugs with nanocarriers which will be more convenient and cost effective. The trend of creation of bilayer delivery systems opened many doors for multiphasic delivery (Goyanes *et al*., 2015). Buccal and mucoadhesive delivery routes with encapsulated nanocarriers could be recognized as superior delivery systems for therapies entailing drug absorption while others used to decrease allergies, pain relief, relaxing, sleep, nervous system defects and antihypertensive reactions. Surface modifications and drug carrier encapsulation may improve stability, toxicity to tissue cells, their kinetic release, *in vivo* sensing and circulation rate. Conjugation of drug carriers may improve durability of drug release and provide protection against enzymatic degradation. Oral delivery systems focusing buccal delivery show promising business trend in biomedical and pharmaceutical industries.

Porous silicon micro as well as nano particles have interesting properties for controlled drug delivery. Because of low toxicity of silicon nanoparticles, they have promising pharmaceutical applications. However, their biostability presents little challenges for chronic use due to metabolization after encapsulation. Secondly, pore size, surface area and free volume matter during fabrication. Generation of pores from nanometer to a number of hundreds in diameter is also possible. Surface chemistry of silicon can be modified according to engineering of drug release profile. Amazing optical features of porous silicon have been provided dimensions for *in vivo* sensing or therapeutics. Fluorescence can be obtained from porous silicon having application in silica quantum dots. Porous silicon can be produced with desired optical reflection spectrum. These promising features of porous silicon have opened new doors for the growth of advanced purposeful structures that are in use with sensors, chips for control as well as for diagnostic and therapeutic functions (Prasad *et al*., 2016) Porous silicon can be integrated into well circuited silicon microelectronic fabrication processes which could be converted into active devices for storage as well as for medical applications (Mayne *et al*., 2000; Stewart *et al*., 1998; Nassiopoulos *et al*., 1995). In the last decade, drug nanocarriers have achieved greater importance for therapeutic applications. This review highlighted major advancements in drug carrier systems and biological improvements in drug carrier administration. The growth of oral formulations for drugs encapsulation with biodegradable and biocompatible porous silicon, its composites with polymers like nanostructures have been proven best for oral drug delivery systems.

Acknowledgement

The author paticularly Asad Muhammad Azam would like to thank Dr Tahir Iqbal Awan, University of Gujrat, Pakistan for his valueable suggestions during writing of this article.

Conflict of Interest. The authors declare no conflict of interest.

References

Aditya, N.P., Ko, S. 2015. Solid lipid nanoparticles (SLNs): delivery vehicles for food bioactives. *Advances-Royal Society of Chemistry*, **5:** 30902-30911.

Anderson, S.H.C., Elliott, H., Wallis, D.J., Canham, L.T., Powell, J.J. 2003. Dissolution of different forms of partially porous silicon wafers under simulated physiological conditions. *Physica Status Solidi A-Applications and Materials Science*, **197:** 331-335.

Anglin, E.J., Schwartz, M.P., Ng, V.P., Perelman, L.A., Sailor, M.J. 2004. Engineering the chemistry and nanostructure of porous silicon Fabry–Pérot films for loading and release of a steroid. *Langmuir*, **20:** 11264-11269.

Araújo, F., das Neves, J., Martins, J.P., Granja, P.L., Santos, H.A., Sarmento, B. 2017. Functionalized materials for multistage platforms in the oral delivery of biopharmaceuticals. *Progress in Materials Science*, **89:** 306-344.

Araújo, F., Shrestha, N., Shahbazi, M.A., Fonte, P., Makila, E.M., Salonen, J., Hirvonen, J.T., Granja, P.L., Santos, H.A., Sarmento, B. 2014. The impact of nanoparticles on the mucosal translocation and transport of GLP-1 across the intestinal epithelium. *Biomaterials*, **35:** 9199-9207.

Banerjee, A., Qi, J., Gogoi, R., Wong, J., Mitragotri, S. 2016. Role of nanoparticle size, shape and surface chemistry in oral drug delivery. *Journal of Control Release*, **238:** 176-185.

Bayliss, S.C., Harris, P.J., Buckberry, L., Rousseau, C. 1997. Phosphate and cell growth on nanostructured semiconductors. *Journal of Materials Science Letters*, **16:** 737-740.

Berger, M.G., Arens-Fisher, R., Thönissen, M., Krüger, M., Billat, S., Lüth, H., Hilbrich, S., Theiss, W., Grosse, P. 1997. Dielectric filters made of porous silicon: advanced performance by oxidation and new layer structures. *Thin Solid Films-Journal*, **297:** 237-240.

Bilati, U., Allemann, E., Doelker, E. 2005. Nano-precipitation versus emulsion-based techniques for the encapsulation of proteins into biodegradable nanoparticles and process-related stability issues. *Aaps Pharmscitech,* **6:** E594-E604.

Bilati, U., Allemann, E., Doelker, E. 2005. Development of a nano-precipitation method intended for the entrapment of hydrophilic drugs into nanoparticles. *European Journal of Pharmaceutical Sciences*, **24:** 67-75.

Bohren, C.F., Huffman, D.R. 1983. *Adsorption and Scattering of Light by Small Particles*, pp. 217, Wiley, New York, USA.

Boukherroub, R., Wojtyk, J.T.C., Wayner, D.D.M., Lockwood, D.J. 2002. Thermal hydrosilylation of undecylenic acid with porous silicon. *Journal of Electrochemical Society*, **149:** 59-63.

Buriak, J.M. 2002. Organometallic chemistry on silicon and germanium surfaces. *Chemical Review*, **102:** 1272-1308.

Canham, L.T. 2007. Nanoscale semiconducting silicon as a nutritional food additive. *Nanotechnology*, **18**.

Canham, L. 1997. Properties of Porous Silicon, In: *EMIS Datareviews*, B.L. Weiss (ed.), vol. **18**, pp. 1-405, Institution of Engineering and Technology, London, UK.

Canham, L.T., Saunders, S.J., Heeley, P.B., Keir, A.M., Cox, T.I. 1994. Rapid chemography of porous silicon undergoing hydrolysis. *Advance Material*, **6:** 865-868.

Cano-Cebrian, M.J., Zornoza, T., Granero, L., Polache, A. 2005. Intestinal absorption enhancement via the paracellular route by fatty acids, chitosans and others: a target for drug delivery. *Current Drug Delivery*, **2:** 9-22.

Castro, P.M., Fonte, P., Sousa, F., Madureira, A.R., Sarmento, B., Pintado, M.E. 2015. Oral films as breakthrough tools for oral delivery of proteins/peptides. *Journal of Control Release*, **211:** 63-73.

Chan, S., Fauchet, P.M., Li, Y., Rothberg, L.J., Miller, B.L. 2000. Porous silicon microcavities for biosensing applications. *Physica Status Solidi A-Applied Research*, **182:** 541-546.

Chin, V., Collins, B.E., Sailor, M.J., Bhatia, S.N. 2000. Compatibility of primary hepatocytes with oxidized nanoporous silicon. *Advance Material*, **13:** 1877-1880.

Chung, T.W., Huang, Y.Y., Liu, Y.Z. 2001. Effects of the rate of solvent evaporation on the characteristics of drug loaded PLLA and PDLLA microspheres. *International Journal of Pharmacy*, **212:** 161-169.

Coffer, J.L., Montchamp, J.L., Aimone, J.B., Weis, R.P. 2003. Routes to calcifled porous silicon: implications for drug delivery and biosensing. *Physica Status Solidi A-Applied Research*, **197:** 336-339.

Collins, B.E., Dancil, K.P., Abbi, G., Sailor, M.J. 2002. Determining protein size using an electrochemically machined pore gradient in silicon. *Advance Functional Materials*, **12:** 187-191.

Collins, R.T., Fauchet, P.M., Tischler, M.A. 1997. Porous silicon: from luminescence to LEDs. *Physics Today*, **50:** 24-31.

Colombo, P., Sonvico, F., Colombo, G., Bettini, R. 2009. Novel platforms for oral drug delivery. *Pharmaceutical Research*, **26:** 601-611.

Crucho, C.I.C., Baros, M.T. 2017. Polymeric nanoparticles: a study on the preparation variables and characterization methods. *Materials Science & Engineering C-Materials for Biological*

Applications, **80:** 771-784.

Danhier, F., Ansorena, E., Silva, J.M., Coco, R., Le Breton, A., Preat, V. 2012. PLGA-based nanoparticles: an overview of biomedical applications. *Journal of Control Release*, **161:** 505-522.

Dorvee, J.R., Sailor, M.J., Miskelly, G.M. 2008. Digital microfluidics and delivery of molecular payloads with magnetic porous silicon chaperones. *Dalton Translation*, doi: 10.1039/b714594b.

Dorvee, J.R., Derfus, A.M., Bhatia, S.N., Sailor, M.J. 2004. Manipulation of liquid droplets using amphiphilic, magnetic 1-D photonic crystal chaperones. *Natural Matters*, **3:** 896-899.

Fujii, M., Nishimura, N., Fumon, H. 2006. Dynamics of photosensitized formation of singlet oxygen by porous silicon in aqueous solution. *Journal of Applied Physics*, **100.**

Fujii, M., Minobe, S., Usui, M. 2004. Generation of singlet oxygen at room temperature mediated by energy transfer from photoexcited porous Si. *Physical Review B-American Physical Society*, **70:** 172101.

Gao, J., Gao, T., Li, Y.Y., Sailor, M.J. 2002. Vapour sensors based on optical interferometry from oxidized microporous silicon films. *Langmuir*, **18:** 2229-2233.

Gao, J., Gao, T., Sailor, M.J.A. 2000. Porous silicon vapor sensor based on laser interferometry. *Applied Physics Letter*, **77:** 901-903.

Giovino, C., Ayensu, I., Tetteh, J., Boateng, J.S. 2012. Development and characterisation of chitosan films impregnated with insulin loaded PEG-b-PLA nanoparticles (NPs): a potential approach for buccal delivery of macromolecules. *International Journal of Pharmaceutical*, **428:** 143-151.

Global Biologics Market, 2016. Global Industry Analysis, will be worth US$479, 752 Million by 2024; Size, Share, Growth, Trends, and Forecast - 2024: TMR, 2017.

Goyanes, A., Wang, J., Buanz, A., Martinez-Pacheco, R., Telford, R., Gaisford, S., Basit, A.W. 2015. 3D printing of medicines: engineering novel oral devices with unique design and drug release characteristics. *Molecular Pharmaceutical*, **12:** 4077-4084.

Gurny, R. 2006. Theme issue: nano- and microscaled drug carriers. *European Journal of Pharmaceutics and Biopharmaceutics*, **63:** III–III.

Harloff-Helleberg, S., Nielsen, L.H., Nielsen, H.M. 2017. Animal models for evaluation of oral delivery of biopharmaceuticals. *Journal of Control Release*, **268:** (Suppl. C) 57-71.

Hermanson, G.T. 2013. *Bioconjugate Techniques*, Greg T. Hermanson, 3rd edition, Academic Press.

Huo, M., Yuan, J., Tao, L., Wei, Y. 2014. Redox-responsive polymers for drug delivery from molecular design to applications. *Polymer Chemistry*, **5:** 1519-1528.

Iqbal, M., Zafar, N., Fessi, H., Elaissari, A. 2015. Double emulsion solvent evaporation techniques used for drug encapsulation. *International Journal of Pharmacy*, **496:** 173-190.

Janshoff, A., Dancil, K.P.S., Steinem, C. 1998. Macroporous p-type silicon Fabry– Perot layers. Fabrication, characterization, and applications in biosensing. *Journal for American Chemical Society*, **120:** 12108–12116.

Jay, T., Canham, L.T., Heald, K., Reeves, C.L., Downing, R. 2000. Autoclaving of porous silicon within a hospital environment: potential benefits and problems. *Physical Status Solidi A-Applied Research*, **182:** 555-560.

Jong, W.H.D., Borm, P.J.A. 2008. Drug delivery and nanoparticles: applications and hazards. *International Journal of Nano Medicine*, **3:** 133-149.

Kawanabe, K., Yamamuro, T., Kotani, S., Nakamura, T. 1992. Acute nephrotoxicity as an adverse effect after intraperitoneal injection of massive amounts of bioactive ceramic powders in mice and rats. *Journal of Biomedical Material Research*, **26:** 209-219.

Kelley, E.G., Albert, J.N., Sullivan, M.O. 2013. Epps III TH. Stimuli- responsive copolymer solution and surface assemblies for biomedical applications. *Chemical Society Reviews*, **42:** 7057-71.

Khalid, M., El-Sawy, H.S. 2017. Polymeric nanoparticles: promising platform for drug delivery. *International Journal of Pharmacy*, **528:** 675-691.

Khalil, N.M., do Nascimento, T.C., Casa, D.M., Dalmolin, L.F., de Mattos, A.C., Hoss, I., Romano, M.A., Mainardes, R.M. 2013. Pharma-cokinetics of curcumin-loaded PLGA and PLGA-PEG blend nanoparticles after oral administration in rats. *Colloids and Surfaces B: Biointerfaces*, **101:** 353-360.

Koshida, N., Koyama, H., Yamamoto, Y., Collins, G.J. 1993. Visible electro-luminescence from porous silicon diodes with an electro-polymerized contact.

Applied Physics Letters, **63:** 2655-2657.

Kumari, A., Yadav, S.K., Yadav, S.C. 2010. Biodegradable polymeric nanoparticles based drug delivery systems. *Colloids and Surfaces B: Biointerfaces*, **75:** 1-18.

Kwon, H.Y., Lee, J.Y., Choi, S.W., Jang, Y.S., Kim, J.H. 2001. Preparation of PLGA nanoparticles containing estrogen by emulsification- diffusion method. *Colloids and Surfaces A Physico-chemical and Engineering Aspects*, **182:** 123-130.

Lai, P., Daear, W., Lobenberg, R., Prenner, E.J. 2014. Overview of the preparation of organic polymeric nanoparticles for drug delivery based on gelatine, chitosan, poly (d,l-lactide-co-glycolic acid) and polyalkyl cyanoacrylate, *Colloids and Surfaces B: Biointerfaces*, **118:** (Suppl. C) 154-163.

Lai, W., Garino, J., Flaitz, C., Ducheyne, P. 2005. Excretion of resorption products from bioactive glass implanted in rabbit muscle. *Journal of Biomedical Material Research Part A*, **75:** 398-407.

Li, X., Chen, Y., Wang, M., Ma, Y., Xia, W., Gu, H.A. 2013. A mesoporous silica nanoparticle-PEI-fusogenic peptide system for siRNA delivery in cancer therapy. *Biomaterials*, **34:** 1391-401.

Li, X., Coffer, J.L., Chen, Y., Pinizzotto, R.F., Newey, J., Canham, L.T. 1998. Transition metal complex-doped hydroxyapatite layers on porous silicon. *Journal of American Chemical Society*, **120:** 11706-11709.

Li, Y.Y., Cunin, F., Sailor, M.J., Link, J.R., Gao, T. 2006. *Nanostructured Casting of Organic and Biopolymers in Porous Silicon Templates*, Patent no. ISS2006/0236436A1, oct; 19,2006. University of California, San Diego, USA.

Li, Y.Y., Cunin, F., Link, J.R. 2003. Polymer replicas of photonic porous silicon for sensing and drug delivery applications. *Science*, **299:** 2045-2047.

Lin, P.C., Lin, S., Wang, P.C., Sridhar, R. 2014. Techniques for physico-chemical characterization of nanomaterials. *Biotechnology Advances*, **32:** 711-726.

Lin, V.S.Y., Motesharei, K., Dancil, K.S., Sailor, M.J., Ghadiri, M.R. 1997. A porous silicon based optical interferometric biosensor. *Science*, **278:** 840-843.

Lohcharoenkal, W., Wang, L.Y., Chen, Y.C., Rojanasakul, Y. 2014. Protein nanoparticles as drug delivery carriers for cancer therapy. *Biomedicine Research International*.

Lynch, I., Dawson, K.A. 2008. Protein-nanoparticle interactions. *Nano Today*, **3:** 40-47.

Madureira, A.R., Campos, D.A., Oliveira, A., Sarmento, B., Pintado, M.M., Gomes, A.M. 2016. Insights into the protective role of solid lipid nanoparticles on rosmarinic acid bioactivity during exposure to simulated gastrointestinal conditions. *Colloids and Surface B Biointerfaces*, **139:** 277-284.

Maruthi, G., Smith, A.A., Manavalan, R. 2011. Nanoparticles–a review, *Journal of Advance Scientific Research*, **2:** 12-19.

Mayne, A.H., Bayliss, S.C., Barr, P., Tobin, M., Buckberry, L.D. 2000. Biologically interfaced porous silicon devices, *Physical Status Solidi A-Applied Research*, **182:** 505-513.

Meade, S.O., Sailor, M.J. 2007. Microfabrication of free standing porous silicon particles containing spectral barcodes. *Physica Status Solidi-Rapid Research Letters*, **1:** R71–R73.

Meade, S.O., Yoon, M.S., Ahn, K.H., Sailor, M.J. 2004. Porous silicon photonic crystals as encoded micro carriers. *Advance Materials*, **16:** 1811-1814.

Meyer, J.D., Manning, M.C. 1998. Hydrophobic ion pairing: altering the solubility properties of biomolecules. *Pharmaceutical Research*, **15:** 188-193.

Mohanraj, V., Chen, Y. 2006. Nanoparticles–a review, *Tropical Journal Pharmaceutical Research*, **5:** 561-573.

Mundargi, R.C., Rangaswamy, V., Aminabhavi, T.M. 2011. Poly (N- vinylcaprolactam-comethacrylic acid) hydrogel microparticles for oral insulin delivery. *Journal of Microencapsulation*, **28:** 384-394.

Mundargi, R.C., Babu, V.R., Rangaswamy, V., Patel, P., Aminabhavi, T.M. 2008. Nano/micro technologies for delivering macromolecular therapeutics using poly (D,L-lactide-co-glycolide) and its derivatives. *Journal of Controlled Release*, **125:** 193-209.

Mura, S., Nicolas, J. 2013. Couvreur P. Stimuliresponsive nanocarriers for drug delivery. *Nature Materials*, **12:** 991-1003.

Nagal, A., Singla, R.K. 2013. Nanoparticles in different delivery systems: a brief review. *Indo Global Journal of Pharmaceutical Sciences*, **3:** 96-106.

Nassiopoulos, A.G., Grigoropoulos, S., Canham, L. 1995. Sub-micrometre luminescent porous silicon structures using lithographically patterned substrates. *Thin Solution Films*, **255:** 329-333.

Ouyang, H., Christophersen, M., Viard, R., Miller, B.L. Fauchet, P.M. 2005. Macroporous silicon

microcavities for macromolecule detection. *Advance Function Material*, **15:** 1851-1859.

Park, J.H., Derfus, A.M., Segal, E., Vecchio, K.S., Bhatia, S.N., Sailor, M.J. 2006. Local heating of discrete droplets using magnetic porous silicon-based photonic crystals. *Journal of American Chemical Society*, **128:** 7938-7946.

Patel, A., Cholkar, K., Mitra, A.K. 2014. Recent developments in protein and peptide parenteral delivery approaches. *Therapeutic Delivery*, **5:** 337-365.

Pelegri-O'Day, E.M., Lin, E.W., Maynard, H.D. 2014. Therapeutic protein-polymer conjugates: advancing beyond PEGylation. *Journal of American Chemistry Society*, **136:** 14323-14332.

Prantera, C., Korelitz, B.I. 1997. *Development of Biopharmaceutical Parenteral Dosage Forms*, pp 264, edition, Boca Raton, CRC Press;

Prasad, L.K., Smyth, H. 2016. 3D Printing technologies for drug delivery: a review. *Drug Development and Industrial Pharmacy*, **42:** 1019-1031.

Quintanar-Guerrero, D., Allemann, E., Fessi, H., Doelker, E. Applications of the ionpair concept to hydrophilic substances with special emphasis on peptides. *Pharmaceutical Research*, **14:** 119-127.

Rawat, M., Singh, D., Saraf, S., Saraf, S. 2006. Nanocarriers: promising vehicle for bioactive drugs. *Biological Pharmaceutical Bulletin*, **29:** 1790-1798.

Righeschi, C., Bergonzi, M.C., Isacchi, B., Bazzicalupi, C., Gratteri, P., Bilia, A.R. 2016. Enhanced curcumin permeability by SLN formulation: the PAMPA approach. *LWT-Food Science and Technology*, **66:** 475-483.

Salonen, J., Laitinen, L., Kaukonen, A.M. 2005. Mesoporous silicon microparticles for oral drug delivery: loading and release of five model drugs. *Journal of Controlled Release*, **108:** 362-374.

Schiffter, H. 2011. *Pharmaceutical Proteins—Structure, Stability, and Formulation, Comprehensive Biotechnology*, pp. 521–541. Academic Press Burlington, Vermont.

Schwartz, M.P., Cunin, F., Cheung, R.W., Sailor, M.J. 2005. Chemical modification of silicon surfaces for biological applications. *Physica Status Solidi A-Applications and Materials Science*, **202:** 1380-1384.

Segal, E., Perelman, L.A., Cunin, F. 2007. Confinement of thermo responsive hydrogels in nanostructured porous silicon dioxide templates. *Advance Function Materials*, **17:** 1153-1162.

Soppimath, K.S., Aminabhavi, T.M., Kulkarni, A.R., Rudzinski, W.E. 2011. Biodegradable polymeric nanoparticles as drug delivery devices. *Journal of Controlled Release*, **70:** 1-20.

Sousa, F., Castro, P., Fonte, P., Sarmento, B. 2015. How to overcome the limitations of current insulin administration with new non-invasive delivery systems. *Therapeutic Delivery*, **6:** 83-94.

Stewart, M.P., Buriak, J.M. 1998. Photopatterned hydrosilylation on porous silicon. *Angewandte Chemie International Edition in English*, **37:** 3257-3260.

Thomas, J.C., Pacholski, C., Sailor, M.J. 2006. Delivery of nanogram payloads using magnetic porous silicon microcarriers. *Lab on a Chip*, **6:** 782-787.

Vaccari, L., Canton, D., Zaffaroni, N., Villa, R., Tormen, M., di Fabrizio, E. 2006. Porous silicon as drug carrier for controlled delivery of doxorubicin anticancer agent. *Microelectronic Engineering*, **83:** 1598-1601.

Vincent, G. 1994. Optical properties of porous silicon superlattices. *Applied Physical Letter*, **64:** 2367-2369.

Wise, D.L. 2000. *Handbook of Pharmaceutical Controlled Release Technology*, 1st ed. Marcel Dekker Inc., New York USA.

Zhang, X.G. 2004. Morphology and formation mechanisms of porous silicon. *Journal of Electrochemical Society*, **151:** C69-C80.